

Universiteit
Leiden
The Netherlands

MAS NMR study of the photoreceptor phytochrome

Rohmer, T.

Citation
Rohmer, T. (2009, October 13). *MAS NMR study of the photoreceptor phytochrome*. Retrieved from https://hdl.handle.net/1887/14203

Version:	Corrected Publisher's Version
License:	Licence agreement concerning inclusion of doctoral thesis in the Institutional Repository of the University of Leiden
Downloaded from:	https://hdl.handle.net/1887/14203

Note: To cite this publication please use the final published version (if applicable).

MAS NMR study of the photoreceptor phytochrome

Thierry Rohmer

MAS NMR study of the photoreceptor phytochrome

PROEFSCHRIFT

Ter verkrijging van de graad van Doctor
aan de Universiteit Leiden,
op gezag van de Rector Magnificus Prof. mr. P. F. van der Heijden,
volgens besluit van het College voor Promoties
te verdedigen op 13 october 2009
klokke 16.15 uur

door

Thierry Rohmer

geboren te Schiltigheim, Frankrijk in 1978

Promotiecommissie

Promotor:	Prof. dr. H. J. M. de Groot
Copromotor:	Dr. J. Matysik
Overige Leden:	Prof. dr. W. Gärtner, Max-Planck Institut Mülheim an der Ruhr
	Prof. dr. J. Brouwer
	Prof. dr. J. Lugtenburg
	Prof. dr. J. P. Abrahams
	Prof. dr. G. van der Marel
	Dr. J. Neugebauer

A mes parents

A la Mercè

The work described in this thesis was carried out at the Leiden Institute of Chemistry under the supervision of Dr. Jörg Matysik. The research was supported by Volkswagen-Stiftung Grant I/79979 and the printing of the thesis was financially supported by the J. E. Jurriaanse Stichting, Rotterdam.

ISBN 978-90-9024576-8

List of abbreviations

Arg	Arginine
Asp	Aspartic acid
BphP	Bacteriophytochrome
BV	Biliverdin
$CDCl_3$	d-Chloroform
CD_2Cl_2	d_2-Dichloromethane
CD_3OD	d_4-Methanol
CP	Cross-Polarization
Cph1Δ2	N-terminal part of Cph1
Cph	Cyanobacterial phytochrome
Cph1	Cyanobacterial phytochrome 1
Cys	Cysteine
DARR	Dipolar-Assisted Rotary Resonance
Eq.	Equation
Fig.	Figure
Fph	Fungal phytochrome
FSLG	Frequency-Switched Lee-Goldburg
GAF	cGMP phosphodiesterase/Adenyl cyclase/FhlA
Gln	Glutamine
His	Histidine
HKD	Histidine Kinase Domain
HKRD	Histidine Kinase Related Domain
HMBC	Heteronuclear Multiple Bond Correlation
HSQC	Heteronuclear Single Quantum Coherence
Leu	Leucine

LG	Lee-Goldburg
Lys	Lysine
MAS	Magic Angle Spinning
MeLoDI	Medium and Long Distance
n.d.	not determined
NMR	Nuclear Magnetic Resonance
PAS	Per-ARNT-Sim
PCB	Phycocyanobilin
PCBE	Phycocyanobilin dimethyl Ester
PDSD	Proton Driven Spin Diffusion
PΦB	Phytochromobilin
Pfr	far-red absorbing state of phytochrome
Phy	Phytochrome
phyA	phytochrome A
*phyA*65	65-kDa fragment of phytochrome A
Pr	red absorbing state of phytochrome
RF	Radio-Frequency
RFDR	Radio-Frequency-driven Dipolar Recoupling
RR	Response Regulator
Ser	Serine
Thr	Threonine
TPPM	Two-Pulse Phase-Modulation
Tyr	Tyrosine
u-[^{13}C,^{15}N]-PCB	uniformly ^{13}C- and ^{15}N-labeled phycocyanobilin

List of symbols

$\mathbf{B}_{\text{eff}}$	effective field
$\mathbf{B}_0$	external magnetic field
H_{CS}	chemical shift Hamiltonian
H_{D}^{II}	homonuclear dipolar Hamiltonian
H_{D}^{IS}	heteronuclear dipolar Hamiltonian
H_0	Zeeman Hamiltonian
$\mathbf{I}$, $\mathbf{S}$	nuclear spin angular momentum operator
I_z, S_z	z-component of $\mathbf{I}$ and $\mathbf{S}$
r_{ij}	internuclear distance between spin i and j
δ	anisotropy parameter
η	asymmetry parameter
γ^i	gyromagnetic ratios of the spin i
λ_{max}	wavelength of maximum optical absorption
μ_0	vacuum permeability
ν	frequency
$\omega_{0\text{i}}$	resonance frequency of spin i
$\boldsymbol{\sigma}$	chemical shielding tensor
σ_{iso}	isotropic value
σ_{xx}	xx eigenvalue of $\boldsymbol{\sigma}$ in the principal axis system
σ_{yy}	yy eigenvalue of $\boldsymbol{\sigma}$ in the principal axis system
σ_{zz}	zz eigenvalue of $\boldsymbol{\sigma}$ in the principal axis system

Contents

List of abbreviations **i**

List of symbols **iii**

1 Introduction **1**

1.1 Phytochrome 1

1.1.1 The phytochrome superfamily 1

1.1.2 The modular domain architecture of phytochromes . . . 3

1.1.3 The phytochrome chromophore 4

1.1.4 The phytochrome photocycle 5

1.1.5 X-ray structures of phytochromes 7

1.2 Theoretical background of solid-state CP/MAS NMR 9

1.2.1 Interactions in solid-state NMR 9

1.2.2 Chemical shielding Hamiltonian 9

1.2.3 Dipolar coupling Hamiltonian 10

1.3 Solid-state NMR techniques 11

1.3.1 Magic angle spinning 12

1.3.2 Cross-polarization 12

1.3.3 Heteronuclear dipolar decoupling 13

1.3.4 Homonuclear correlation spectroscopy 13

1.3.5 Heteronuclear correlation spectroscopy 15

1.4 Aim and scope of this thesis 15

2 MAS NMR on phycocyanobilin **17**

2.1 Introduction 17

2.2 Results 19

2.2.1 ^{13}C chemical shift assignment 19

2.2.2 ^{15}N chemical shift assignment . . . 23
2.3 Discussion . . . 25
2.3.1 PCB tautomers . . . 25
2.3.2 Differences between forms A and B . . . 26
2.3.3 PCB Dimers . . . 27
2.3.4 Geometry optimization and dimer characterization . . . 28
2.4 Materials and methods . . . 29
2.4.1 Sample preparation . . . 29
2.4.2 Mass spectrometry . . . 30
2.4.3 NMR experiments . . . 30

3 MAS NMR on the Pr and Pfr states 33
3.1 Introduction . . . 33
3.2 Results . . . 34
3.2.1 Assignments of ^{13}C CP/MAS NMR spectra of Pr and Pfr states in Cph1Δ2 . . . 34
3.2.2 ^{15}N CP/MAS NMR of u-[^{13}C,^{15}N]-PCB-Cph1Δ2 . . . 39
3.2.3 Pr → Pfr conversion in Cph1Δ2 . . . 41
3.2.4 Pr → Pfr conversion in the plant phytochrome *phyA* . . . 41
3.3 Discussion . . . 44
3.3.1 Chromophore photoconversion . . . 44
3.3.2 Charge localization in phytochrome . . . 46
3.3.3 Signal transduction pathway . . . 48
3.4 Materials and Methods . . . 49
3.4.1 Sample preparation for MAS NMR spectroscopy . . . 49
3.4.2 MAS NMR spectroscopy . . . 49

4 The Pfr → Pr photoconversion 51
4.1 Introduction . . . 51
4.2 Results . . . 52
4.2.1 Conformational changes of the cofactor carbon atoms . . . 52
4.2.2 Assignment of the nitrogen atoms . . . 56
4.2.3 Changes of the nitrogen atoms . . . 58
4.3 Discussion . . . 59
4.3.1 The Pfr → Lumi-F transition . . . 59
4.3.2 The Lumi-F → Meta-F transition . . . 61
4.3.3 The Meta-F → Pr transition . . . 61

4.3.4 Model for the back-reaction 61
4.3.5 Model for signal transduction 63
4.4 Materials and Methods 64
4.4.1 Sample preparation for MAS NMR spectroscopy 64
4.4.2 MAS NMR spectroscopy 65

5 Discussion and outlook **67**
5.1 Comparison with model compounds 68
5.1.1 Effect of protein environment on PCB in phytochrome . 68
5.1.2 Pr → Pfr conversion 71
5.1.3 Photoisomerization in phytochrome 72
5.2 Results and prospects 73

Appendices **77**

A **79**

B **83**

C **89**

Summary **93**

Samenvatting **97**

Publications **101**

Curriculum vitae **103**

Chapter 1

Introduction

1.1 Phytochrome

1.1.1 The phytochrome superfamily

The dominant factor regulating development and behavior of photosynthetic organisms is light, which provides both the energy necessary for growth and metabolism as well as the sensory information needed for adaptation to the environment. In order to sense light, plants use photoreceptors that perceive different areas of the electromagnetic spectrum [1–3]. Photoreceptors are proteins that bind a chromophore which undergoes a photochemical reaction upon absorption of light at a specific wavelength.

The phytochromes form a family of photoreceptors that is collectively defined by the use of a bilin chromophore (see section 1.1.3). Phytochrome pigments were first characterized in higher plants in the 1950's [4]. Vierstra and Quail [5] isolated the full-length phytochrome protein from *Avena sativa* in 1982 and the complete amino acid sequence of this phytochrome was obtained in 1985 [6]. More recently, polygenetic and biochemical studies have dramatically expanded the phytochrome superfamily to other domains of life. Phytochromes were discovered in proteobacteria, cyanobacteria, fungi and possibly slime moulds. Karniol *et al.* [7] organized the members of the phytochromes superfamily into distinct subfamilies that include plant phytochromes, bacteriophytochromes, cyanobacterial phytochromes, fungal phytochromes and a collection of phytochrome-like sequences (Fig. 1.1).

The phytochrome properties are triggered by the intrinsic photochemical

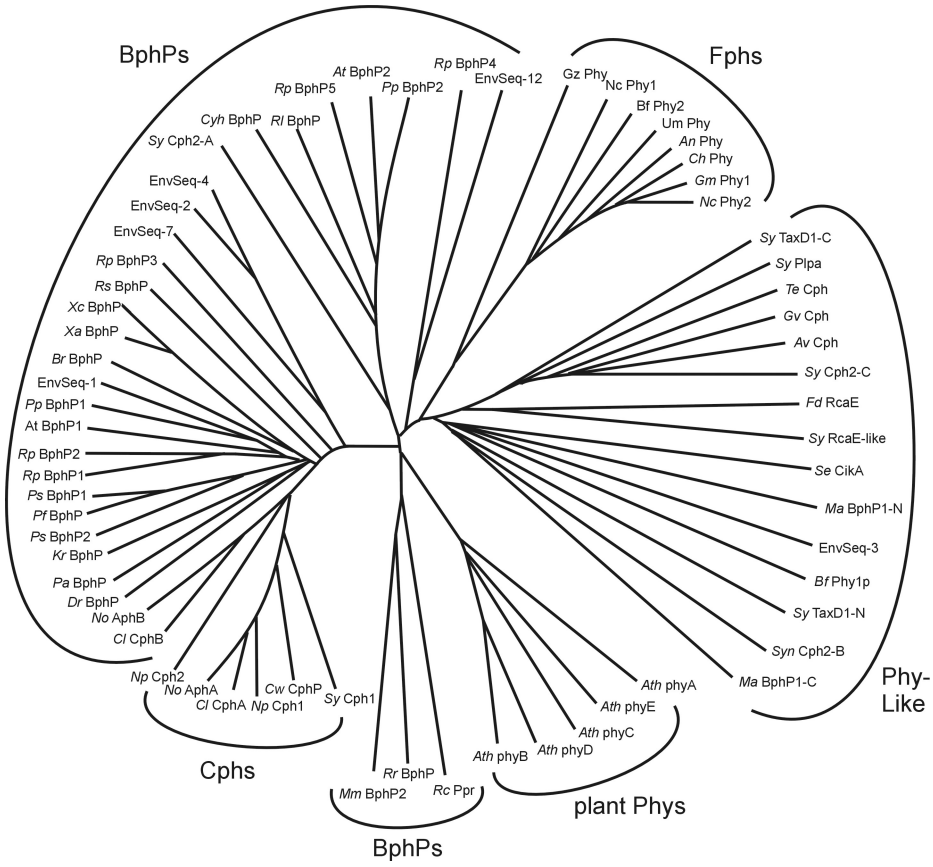


Figure 1.1: Phylogenetic tree of the phytochrome superfamily based on alignment of the GAF domain (adapted from [7]).

activity of their bilin (or linear open-chain tetrapyrrole) prosthetic group within the protein matrix (Fig. 1.2A). It allows phytochromes to occur in two photointerconvertible states, the red-light Pr ($\lambda_{\max} \sim 660$ nm) and far-red-light Pfr ($\lambda_{\max} \sim 710$ nm) absorbing states (Fig. 1.2B). The biological activity of phytochromes is related to the Pr/Pfr ratio, which is determined by the light environment. The plant Phys, in combination with other photoreceptors, regulate photomorphogenetic processes such as seed germination, etiolation, growth inhibition, leaf development, phototropism, shade avoidance, induction of flowering and regulation of the circadian clock [3]. On the other hand, the biological function of the other phytochromes remains mostly unknown. It has been postulated that BphPs act as bilin sensors that can function as

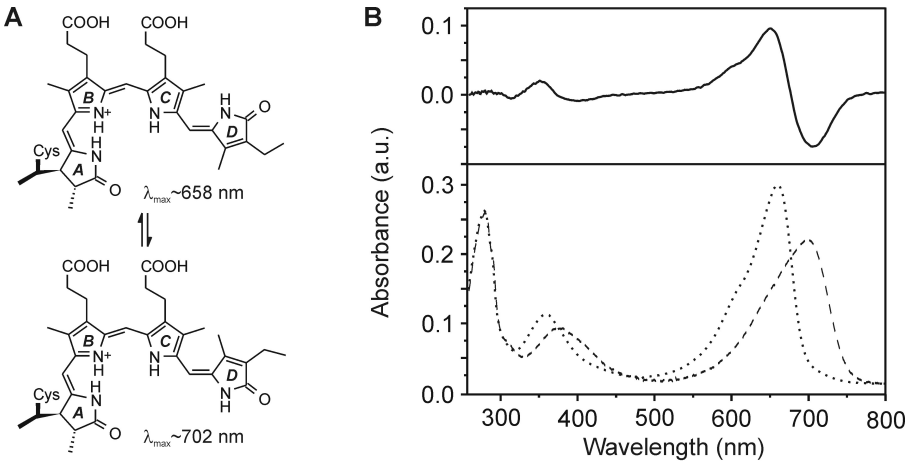


Figure 1.2: Photoconversion of cyanobacterial phytochrome 1 (Cph1). (**A**) Structure of the phycocyanobilin chromophore with *ZZZssa* and *ZZEssa* geometries as assumed in the Pr and Pfr states, respectively. (**B**) Absorption spectrum of Cph1 in the Pr (dotted line), Pfr (dashed line) and Pr-Pfr difference spectrum (full line).

photoreceptors. In particular, it has been proposed that BphPs regulate the biosynthesis of the photosynthetic apparatus in the photosynthetic bacterium *Rhodopseudomonas palustris* [8] and trigger pigment biosynthesis in *Deinococcus radiodurans* and *Rhodospirillum centenum* [9, 10].

1.1.2 The modular domain architecture of phytochromes

All phytochrome families share a common dimeric Y-shaped architecture (Fig. 1.3A) [11–13]. The quaternary structure of each monomer consists of two domains (for review, see [7, 14]). The N-terminal photosensory region binds the bilin cofactor and is composed of three conserved domains, termed P2 or PerARNT-Sim domain, P3 or cGMP phosphodiesterase/adenyl cyclase/FhlA domain, and P4 or PHY domain (uppercase letters are used to denote the Phy domain specifically), while the C-terminal regulatory module contains a histidine kinase or histidine kinase related domain (Fig. 1.3B). Plant Phys have an additional N-terminal extension termed P1 and two additional regulatory PAS domains. Fphs have distinct N-terminal extensions and additional C-terminal response regulator domains. Canonical phytochromes thus consist of a PAS-GAF-PHY N-terminal photosensory module typically combined with

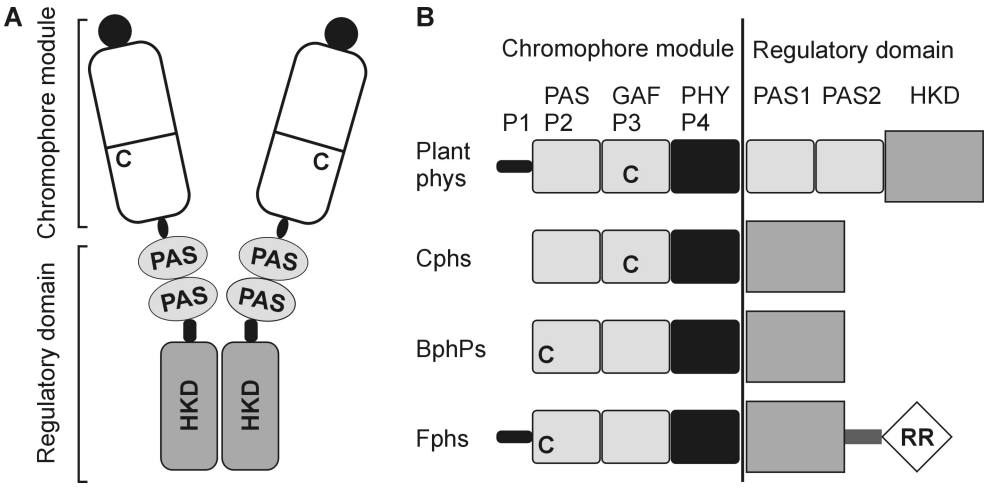


Figure 1.3: Quaternary structure of plant phytochrome in the Pr state adapted from [16] (**A**). Schematic representation of the domain structure of plant Phys, Cphs, BphPs and Fphs phytochromes (**B**). The chromophore location is indicated by **C**.

a C-terminal HKRD module. The concatenation of PAS, GAF, and PHY domains attached to HKRD modules typify all classes of phytochromes and phytochrome-related proteins. For a detailed description of the phytochrome domains, see [15].

1.1.3 The phytochrome chromophore

The bilin or open-chain tetrapyrrole chromophores incorporated in all phytochromes are synthesized from hemes in two steps. First, a heme oxygenase converts the heme into biliverdin (Fig. 1.4), which is directly attached as chromophore of the BphPs and Fphs *via* a thioether linkage at $C3^2$ to a conserved cysteine upstream of the P2/PAS domain [17, 18]. In plants and cyanobacteria, however, BV is further reduced to yield phytochromobilin in higher plants and phycocyanobilin in cyanobacteria and green algae (Fig. 1.4). Both PΦB and PCB bilins are covalently attached at $C3^1$ to a conserved cysteine in the P3/GAF domain of the photosensory core [19–21].

Borucki *et al.* have investigated the autocatalytic assembly of the Cph1 apoprotein with its native PCB chromophore [22]. The first step of the PCB assembly is associated with a major red shift and transfer of oscillator strength from the Soret region to the 680 nm region. This absorption change is due

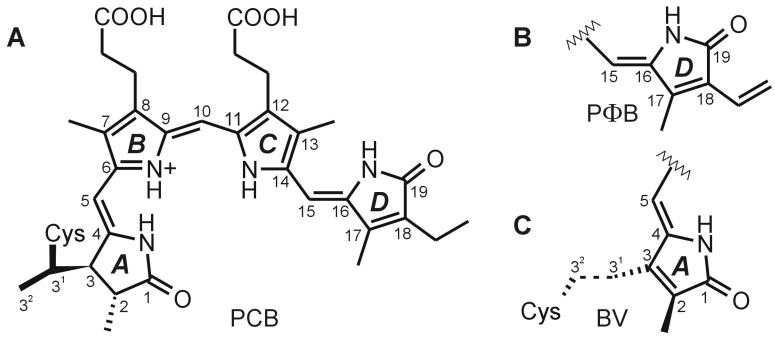


Figure 1.4: Structure of the phycocyanobilin (PCB) in the *ZZZssa* geometry (**A**). Ring ***D*** of phytochromobilin (PΦB, **B**) and ring ***A*** of biliverdin (BV, **C**) are represented. The remainder of these molecules is identic to PCB.

to the formation of the extended conformation of the linear tetrapyrrole, presumably from a *ZZZsss* (5-*Z*, 10-*Z*, 15-*Z*, 5-*syn*, 10-*syn*, 15-*syn*) geometry of the three methine bridges, as present in solution [23, 24], to a *ZZZssa* geometry [25]. Then the protonation of the ring ***B*** nitrogen occurs in the binding pocket. The third step is associated with a blue shift of about 25 nm, which has been attributed to the formation of the covalent bond with a cysteine residue.

The intrinsic photochemical activity of the open-chain tetrapyrrole cofactor inside the chromophore binding domain allows the photoconversion between the Pr ($\lambda_{max} \sim 660$ nm) and Pfr ($\lambda_{max} \sim 710$ nm) states. Using 60 kDa chromopeptides, ^{1}H liquid-state NMR studies revealed that the absorption of red light triggers the *Z*-to-*E* photoisomerization of the C15=C16 double bond [20, 26].

1.1.4 The phytochrome photocycle

The photochemical conversion processes of phytochrome have been intensively investigated. Time-resolved absorption, low temperature and vibrational spectroscopic methods allowed for the identification of three intermediates appearing during the Pr → Pfr pathway (Lumi-R, Meta-R$_a$, and Meta-R$_c$), and at least two intermediates (Lumi-F and Meta-F) during the reverse Pfr → Pr reaction (Fig. 1.5). The first step of the Pr → Pfr conversion is the *Z*-to-*E* photoisomerization of the C15=C16 double bond [20, 26–29]. Ultrafast

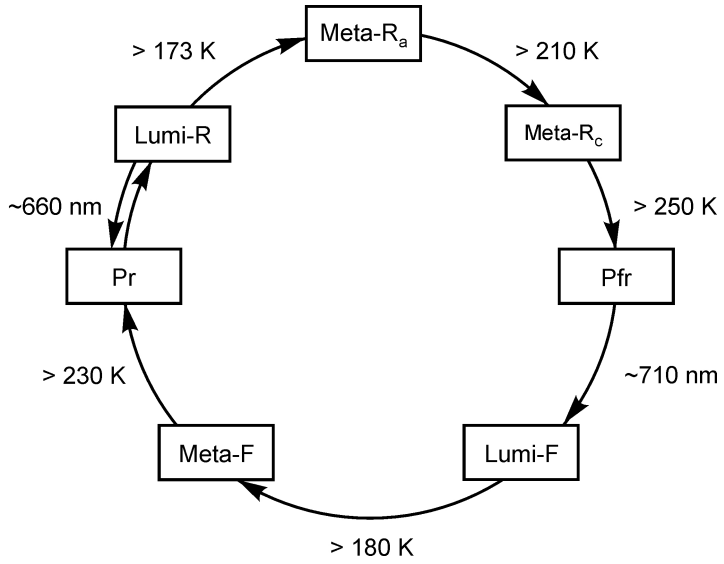


Figure 1.5: Photocycle of the Cph1 phytochrome

Vis/Vis pump-probe spectroscopy and picosecond time-resolved fluorescence spectroscopy at room temperature have determined the time scale of the formation of Lumi-R to be in the picosecond range [30–36]. The extent of the photoreversible Pr → Pfr phototransformation upon red light illumination was determined to be about 0.75 for Cphs [37] and about 0.87 for plant Phys [38]. In both cases, the quantum yield Φ of 0.15 is relatively low. The subsequent reaction steps occur on the microsecond to millisecond time scale. Intermediate states of the photocycle of different Phys have been addressed by Fourier transform infrared and resonance Raman spectroscopy using low-temperature trapping techniques [27, 39–43]. At room temperature, the Meta-R_a state is formed within hundreds of microseconds and decays within milliseconds to the last intermediate before Pfr, called Meta-R_c [27, 39, 42]. The Meta-R_c formation is characterized by a significant red shift of the first absorption maximum and is the key step of the Pfr formation, which occurs within hundreds of milliseconds.

The Pfr → Pr conversion has been investigated less intensively. Until now, two intermediates have been identified, Lumi-F and Meta-F. While the Pr photoreaction occurs in 40-200 ps, the Pfr photoreaction is much faster and occurs on the time scale of a few picoseconds [31,33,35]. Despite intensive

and extensive investigations with vibrational and optical spectroscopy [27,39, 40, 43], the molecular and mechanical characteristics of these intermediates remain to be discovered.

1.1.5 X-ray structures of phytochromes

Until 2005, the study of the structural interactions in phytochrome was limited to indirect methods such as amino acid mutation [44–50]. A breakthrough occurred when the crystallographic studies of the CBDs from *Deinococcus radiodurans* DrBphP [18,51] and *Rhodopseudomonas palustris* RpBphP3 [52] revealed the structures of the PAS and GAF domains and their biliverdin-IXα chromophore in the Pr state. However, these phytochromes lack the PHY domain, which has been shown to be required for Pfr stability [19, 44, 45, 47, 48] and do not undergo full photoconversion between the Pr and Pfr states. The X-ray structure of the complete sensory module (PAS-GAF-PHY tridomain) of the N-terminal part of the cyanobacterial phytochrome 1 (residues 1-514) from *Synechocystis* sp. PCC 6803 in the Pr state has been resolved in 2008 [53]. In the tertiary structure of these three proteins, the PAS domain penetrates the GAF domain to form a knot in which the N-terminal extension passes through the large insert in the GAF domain. The unique feature of the Cph1 structure is a long, tongue-like protrusion from the PHY domain that seals the chromophore pocket (Fig. 1.6A).

Although the comparison between the tertiary structures of these three proteins revealed some differences, most of the chromophore-protein interactions present in the CBD are conserved. The domain architecture and CBD in Cph1Δ2 are presented in Figure 1.6B. The PCB cofactor is covalently attached to the GAF domain by a carbon-thioether link between the $C3^1$ carbon and the sulfur of Cys-259 and adopts a *ZZZssa* geometry at the three methine bridges. The chromophore is twisted by angles of 9.8°, 1.4°, and 26.3° between pyrrole rings ***A*-*B***, ***B*-*C***, and ***C*-*D***, respectively. However, slight rotations around single bonds that are hardly reflected by the crystal structures may cause a more distorted chromophore, a scenario that is supported by a recent investigation utilizing vibrational spectroscopy and density functional theory (DFT) calculations [54]. One of the main features of the chromophore/protein interactions is the occurrence of a very well ordered water molecule (W-3) that participates in a hydrogen-bonding network with the nitrogen atoms of the rings ***A***, ***B***, and ***C***, the His-260 Nδ nitrogen and the

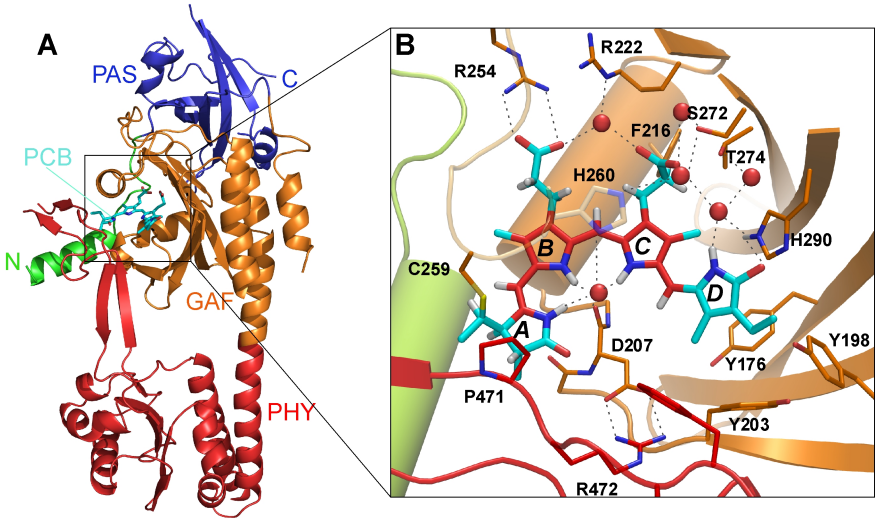


Figure 1.6: Ribbon representation of the sensory module structure of Cph1Δ2 showing the N-terminal α-helix (green) and PAS (blue), GAF (orange) and PHY (red) domains (**A**) and zoom into the chromophore region (**B**).

amide oxygen of Asp-207. The conserved His-290 residue is hydrogen-bonded to the C19 carbonyl of ring ***D*** and is linked to the carboxylic group of the propionic side-chain of ring ***C*** through a water-mediated bridge. In addition, the crystal structure of the CBD shows that the rings ***A***, ***B*** and ***C*** are tightly packed inside the matrix, especially around the C10 atom connecting rings ***B*** and ***C***. In contrast, there is space for ring ***D*** to rotate upon *Z*-to-*E* photoisomerisation of the C15=C16 double bond [53].

The crystal structure of the PaBphP-PCD BphP from *Pseudomonas aeruginosa* with an intact, fully photoactive photosensory core domain in its dark-adapted Pfr state has been determined in 2008 [55]. In this structure, the BV chromophore adopts a *ZZEssa* geometry. Asp-194, Tyr-250, and Ser-459 (equivalent to Asp-207, Tyr-263 and Ser-472 in Cph1Δ2) interact directly with the pyrrole nitrogen of ring ***D***, and Tyr-250, Gln-188, and Ser-459 (Tyr-263, Lys-201 and Ser-472 in Cph1Δ2) are within hydrogen-bonding distance of the C19 carbonyl group of ring ***D***. It is believed that the main features of the PaBphP-PCD BphP structure in its Pfr dark-adapted state are similar to Cphs and plant Phys. However, it has to be kept in mind that the PaBphP-PCD BphP has a low stability in the Pr state and that some residues of the

CBD (Gln-188 or Arg-453) are not conserved along the Phy family.

1.2 Theoretical background of solid-state CP/MAS NMR

1.2.1 Interactions in solid-state NMR

The Zeeman interaction between the nuclear magnetic moment of a spin and the external field **B** is the dominant interaction in NMR. This interaction can be described by the Zeeman Hamiltonian H_z for a magnetic field $\mathbf{B}_0$ along the z-axis

$$H_z = -\gamma^i \hbar I_z B_0, \tag{1.1}$$

where I_z is the z-component of the nuclear spin operator **I**. Although the Zeeman interaction dominates the behavior of the nuclear spin system and determines the quantization z-axis in the theoretical description, it contains little relevant structural information and is removed from the description by a transformation to a frame that is rotating at the NMR frequency along the z-axis [56].

For the spectroscopic applications of NMR, the relevant information originates from the local fields that the nuclear spins "feel". These fields are due to the shielding of the $\mathbf{B}_0$ field by the electron clouds and from the dipolar couplings between spins. For an ensemble of nuclear spins placed in a large magnetic field containing two species, *i.e.*, an abundant I spin system (*e.g.* ^{1}H) with a gyromagnetic ratio γ^I and a resonance frequency ω_{0I} and a dilute S spin system (*e.g.* ^{13}C, ^{15}N) with a gyromagnetic ratio γ^S and a resonance frequency ω_{0S}, the interactions can be described by the chemical shift Hamiltonian H_{CS}, and the homonuclear and heteronuclear dipolar Hamiltonians, H_{D}^{II} and H_{D}^{IS}, respectively. In the rotating frame, this leads to a spin Hamiltonian having the form

$$H = H_{\mathrm{CS}} + H_{\mathrm{D}}^{II} + H_{\mathrm{D}}^{IS}. \tag{1.2}$$

1.2.2 Chemical shielding Hamiltonian

The chemical shielding Hamiltonian expressed as

$$H_{\mathrm{CS}} = -\gamma \mathbf{I} \boldsymbol{\sigma} \mathbf{B_0} \tag{1.3}$$

describes the effect of the electron distribution around the nuclear spin, where $\boldsymbol{\sigma}$ is the chemical shielding tensor.

The electronic distribution around a nucleus in a molecule is rarely spherically symmetric. Since the chemical shielding arises from the electronic surroundings of a nucleus, its value depends on the orientation of the molecule in the magnetic field $\mathbf{B}_0$. This orientation dependence is best described in terms of a chemical shielding tensor, which is a 3×3 matrix that relates the orientation of the magnetic field to the molecular frame in which the induced electronic currents are generated.

The chemical shielding tensor can be placed into its principal axis system, *i.e.*, the reference frame in which it is diagonal and all off-diagonal components are zero, where the principal values of the shielding tensor are σ_{xx}, σ_{yy} and σ_{zz}. In solid-state NMR, the tensor is often represented by

$$\begin{aligned} \sigma_{\text{iso}} &= -\frac{1}{3}(\sigma_{xx} + \sigma_{yy} + \sigma_{zz}), \\ \delta &= \sigma_{zz} - \sigma_{\text{iso}}, \\ \text{and } \eta &= -\frac{\sigma_{xx} - \sigma_{yy}}{\delta}. \end{aligned} \tag{1.4}$$

Here, σ_{iso} is the isotropic value, while δ and η are the anisotropy and asymmetry parameter, respectively [57, 58].

The expression for the anisotropic frequency of a single site in a static sample is given by Equation 1.5 where the orientation dependence of the frequency can be expressed in terms of the polar angles (θ, ϕ) of the $\mathbf{B}_0$ field in the principal axis system [58]:

$$\omega(\theta, \phi) = \delta - \frac{1}{2}(3\cos^2\theta - 1 - \eta - \sin^2\theta\cos 2\phi). \tag{1.5}$$

The chemical shielding Hamiltonian H_{CS} in the principal axis system can be rewritten as

$$H_{\text{CS}} = [\sigma_{\text{iso}}\gamma B_0 + \frac{1}{2}\delta(3\cos^2\theta - 1 - \eta - \sin^2\theta\cos 2\phi)]I_z. \tag{1.6}$$

1.2.3 Dipolar coupling Hamiltonian

The heteronuclear coupling is responsible for much of the broadening observed in the solid-state NMR spectrum. Since each spin represents a nuclear magnetic moment that produces a small magnetic field, every spin "feels" the

magnetic field produced by the nearby spins. The strength of the heteronuclear dipolar coupling is represented by the truncated dipolar Hamiltonian

$$H_{\mathrm{D}}^{IS} = -\frac{\mu_0}{4\pi}\hbar \sum_i \sum_j \frac{\gamma^I \gamma^S}{r_{ij}^3} \frac{1}{2}(3\cos^2\theta_{ij} - 1) 2 I_z^i S_z^j, \tag{1.7}$$

where r_{ij} represents the internuclear distance, μ_0 is the vacuum permeability, γ^I and γ^S are the gyromagnetic ratios of the I and S spins, respectively, and I_z^i and S_z^j are the z-components of the nuclear spin angular momentum operators $\mathbf{I}$ and $\mathbf{S}$, respectively. The angle θ_{ij} describes the orientation of the internuclear vector with respect to the orientation of the external magnetic field. Since the magnitude of the coupling between two nuclear spins has also an r^{-3} distance dependence, the dipolar coupling is a long-range through-space interaction.

Spins also experience a homonuclear dipolar coupling, which results from an interaction between spins of the same species. The homonuclear dipolar Hamiltonian of the I spins is given by

$$H_{\mathrm{D}}^{II} = -\frac{\mu_0}{4\pi}\hbar \sum_i \sum_j \frac{\gamma^I \gamma^S}{r_{ij}^3} \frac{1}{2}(3\cos^2\theta_{ij} - 1)(3 I_z^i S_z^j - \mathbf{I}^i \mathbf{I}^j). \tag{1.8}$$

In this case, r_{ij} represents the internuclear distance and the angle θ_{ij} describes the orientation of the internuclear vector with respect to the orientation of the external magnetic field. Two spins of the same species are able to undergo an energy-conserving "flip-flop" transition in which one spin flips up while the other spin flips down.

1.3 Solid-state NMR techniques

In liquid-state NMR, spectra consist of a series of very sharp signals, which are due to the averaging of the anisotropic NMR interactions by rapid tumbling. By contrast, the full effects of anisotropic or orientation-dependent interactions are observed in solid-state NMR and the resulting signals are generally very broad. In the solid-state, enhancement of peak resolution and signal intensity is obtained under magic angle spinning by the transfer of the ^{1}H magnetization to a dilute spin (^{13}C or ^{15}N) *via* cross-polarization in combination with strong proton decoupling.

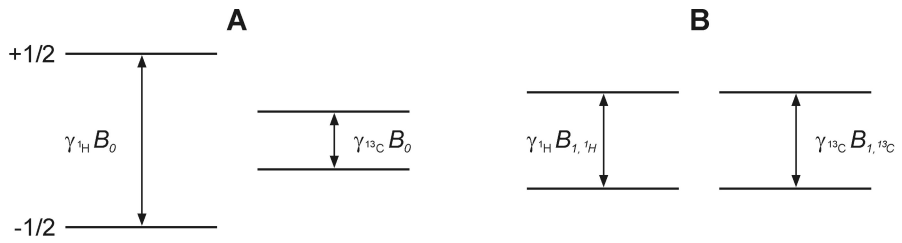


Figure 1.7: Energy levels of the I and S spins. In the laboratory frame, no transfer of magnetization occurs (**A**). In the rotating frame (**B**), the transfer of magnetization is possible due to the application of the RF fields.

1.3.1 Magic angle spinning

As shown in sections 1.2.2 and 1.2.3, the dependence on the molecular interaction is of the form $(3\cos^2\theta - 1)$, where the angle θ describes the orientation of the spin interaction tensors, in particular the chemical shielding and dipolar coupling tensors. In the MAS experiment, the sample is spun rapidly in a cylindrical rotor around a spinning axis oriented at the magic angle ($\theta_{\mathrm{R}} = 54.74°$) with respect to the applied magnetic field $\mathbf{B}_0$ [59–61]. MAS averages the dipolar coupling interactions to zero. In addition, the anisotropic part of the chemical shift disappears under MAS conditions and with fast rotation, the anisotropic line broadening is removed resulting in narrow lines. For a detailed mathematical description of MAS, see [57].

1.3.2 Cross-polarization

Detecting low-γ nuclei such as ^{13}C or ^{15}N is difficult due to their low abundances, low spin polarization and low signal intensity. In addition, dilute spins can exhibit long relaxation times. These drawbacks are overcome by the CP technique, which allows the magnetization to flow from highly polarized nuclei to nuclei with lower polarizations when the two are brought into dipolar contact. In the laboratory frame, the separation between the spin-up and spin-down energy levels do not allow for exchange of magnetization (Fig. 1.7A). Dipolar contact is obtained through the simultaneous application of two external radio-frequency fields satisfying the Hartmann-Hahn condition [62]

$$\alpha_{\mathrm{a}}\gamma^{\mathrm{a}}B_{1\mathrm{a}} = \alpha_{\mathrm{b}}\gamma^{\mathrm{b}}B_{1\mathrm{b}}, \tag{1.9}$$

where γ^{i} and B_{1i} are the gyromagnetic ratio and RF field strength for nucleus i, and $\alpha = [I\ (I + 1)\ -\ m(m\ -\ l)]^{1/2}$ for a transition between the levels m and (m - 1). When both nuclei have $I = 1/2$, this equation reduces to the familiar expression

$$\gamma^{a}B_{1a} = \gamma^{b}B_{1b}. \tag{1.10}$$

One of the RF fields is tuned to the resonance frequency of the I spins and the other to the S spins. As a result, both the magnetization of the I and S spins are rotated around the axis of the applied RF fields. When the nutation frequencies of the I and S spins are equal, an energy-conserving dipolar contact between the two spins is created and the polarization is transferred. The contact is best described in the axes of frames, rotating at both the I and S spin nutation frequencies, in which the spacing between the spin-up and spin-down energy levels is equal for the I and S spins (Fig. 1.7B).

1.3.3 Heteronuclear dipolar decoupling

In solid-state NMR, heteronuclear coupling is responsible for much of the signal broadening. Due to the $(3\cos^2\theta - 1)$ dependence of the heteronuclear interaction, experiments with MAS eliminate the broadening due to the heteronuclear interactions. Another way to obtain signal enhancement is to manipulate the I spins, *e.g.* ^{1}H, in such a way that their interaction with the dilute S spins, *e.g.* ^{13}C or ^{15}N, is averaged to zero. For example, this can be obtained by constantly applying RF power known as continuous wave irradiation, which rotates the I nuclear spins between their spin-up and spin-down states and averages the heteronuclear interactions to zero.

1.3.4 Homonuclear correlation spectroscopy

It has been shown in section 1.3.1 that MAS averages the dipolar coupling and results in signal enhancement. However, MAS also erases the structural information content of these interactions. The ^{13}C-^{1}H dipolar-assisted rotary resonance pulse sequence has been designed by Takegoshi *et al.* [63,64] to reintroduce the ^{13}C-^{1}H dipolar interactions. In this thesis, the DARR sequence has been used to record ^{13}C-^{13}C homonuclear dipolar coupling correlation experiment in the solid state. The DARR sequence (Fig. 1.8A) begins with CP of the ^{1}H magnetization to the nearby ^{13}C nuclei. The ^{13}C-^{1}H dipolar interaction is recovered during t_1 by a continuous wave RF irradiation on ^{1}H

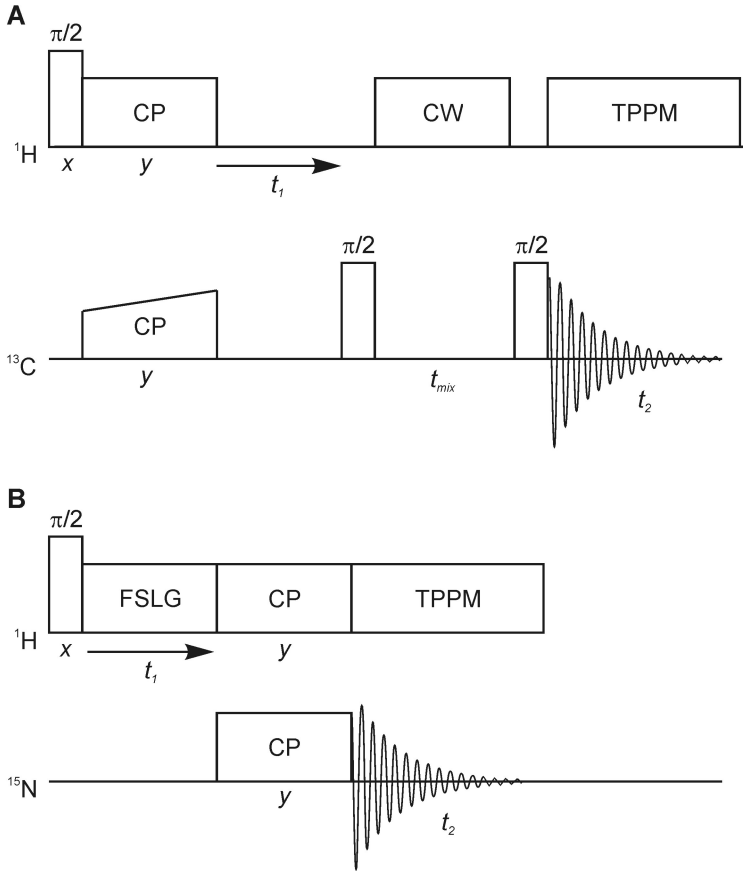


Figure 1.8: Schematic representation of the 2D ^{13}C-^{13}C MAS DARR (**A**) and 2D ^{1}H-^{13}C MAS FSLG (**B**) experiments.

with the intensity ν_1 satisfying the rotary-resonance condition $\nu_1 = n\nu_R$ (n=1 or 2), where ν_R is the rotation frequency. The spectral overlap between two relevant ^{13}C spins is realized between a spinning sideband of one ^{13}C spin and the ^{13}C-^{1}H dipolar pattern of another ^{13}C spin. Then, recoupling due to rotational resonance occurs for the ^{13}C-^{13}C pair and leads to polarization transfer under MAS. Finally, the ^{13}C magnetization is detected in the direct dimension t_2 under two-pulse phase-modulation heteronuclear decoupling [65]. The proton-driven spin diffusion experiment is similar to DARR, the proton decoupling is however switched off during the spin diffusion mixing period.

1.3.5 Heteronuclear correlation spectroscopy

The large homonuclear dipolar couplings of the proton nuclei make their direct detection difficult. In this thesis, a variant of the Lee-Goldburg technique [66], *i.e.* the frequency-switched Lee-Goldburg heteronuclear correlation spectroscopy [67,68] (Fig. 1.8B), is used for the determination of the proton chemical shifts. The ^{1}H magnetization is initially rotated into the xy plane by a $\pi/2$ x-pulse. Directly after the initial pulse, the protons are subject to a train of FSLG pulses for a time t_1. The application of a frequency switched off-resonance RF field between $\omega_{+\Delta LG}$ and $\omega_{-\Delta LG}$ results in an effective field $\mathbf{B}_{\text{eff}}$ in the rotating frame that is inclined at the magic angle with respect to the static magnetic field $\mathbf{B}_0$ [66]. The LG condition is given by Equation 1.11, where ω_1 = -γB$_1$:

$$\pm\Delta\text{LG} = \omega_{\pm\Delta\text{LG}} - \gamma B_0 = \pm\frac{1}{2}\sqrt{2}|\omega_1|. \tag{1.11}$$

The train of FSLG pulses is used to improve the efficiency of the homonuclear proton decoupling. Thus, the magnetization evolves under the ^{1}H chemical shifts and the heteronuclear couplings to ^{13}C nuclei during t_1. After t_1, the ^{1}H magnetization is transferred through CP to the neighboring ^{13}C nuclei for detection in t_2. In this way, the 2D FSLG spectrum correlates broad ^{1}H resonances with the relatively narrow resonances of the ^{13}C nuclei and allows for increased resolution of the proton chemical shifts.

1.4 Aim and scope of this thesis

In this thesis, solid-state MAS NMR spectroscopy has been applied in combination with ^{13}C- and ^{15}N-labeling of the bilin chromophore to study the photochemical machinery of phytochrome.

Chapter 2 deals with the MAS NMR study of free PCB in its microcrystalline state. ^{13}C and ^{15}N labeling of the PCB moiety allows for complete ^{13}C and ^{15}N assignments deduced from 2D ^{13}C-^{13}C and ^{13}C-^{15}N correlation spectroscopy. It is shown that the PCB moieties are present in the crystal in two forms, called A and B, at a ratio A:B = 1:1. In combination with computational methods, a structural model for the PCB dimer is proposed.

Chapter 3 focuses on the electronic ground state of the PCB chromophore in Cph1Δ2 in the parent states Pr and Pfr. The analysis of the isotropic

^{13}C chemical shifts reveals the electronic changes along the conjugated π-system and the modification of chromophore/protein interactions. The NMR data shown in this chapter are used to present a model for signal transduction in phytochrome.

Chapter 4 describes the Pfr → Pr back-reaction. The two intermediates, Lumi-F and Meta-F, have been thermally trapped inside the magnet at low temperature and studied by ^{1}H, ^{13}C and ^{15}N MAS NMR spectroscopy. The results show that the back-reaction proceeds in two steps and provide further insight into the mechanism of signal transduction in phytochrome.

Chapter 5 provides a general discussion on the results and conclusions obtained in this thesis. Finally, an outlook to future experiments is presented.

Chapter 2

CP/MAS NMR study on microcrystalline phycocyanobilin

2.1 Introduction

Bilins are linear tetrapyrroles. This class of compounds has been named as bile pigments of mammals, however, they are also found in lower vertebrates, invertebrates as well as in red algae and green plants. In mammals, tetrapyrroles are generated as products of heme catabolism, which results in the formation of the linear tetrapyrroles biliverdin and bilirubin [69]. In plants and algae, linear tetrapyrrolic moieties are present, for example, as cofactors of the photoreceptor Phy and the cyanobacterial light-harvesting phycobiliproteins. One member of the bilin family, PCB (Fig. 2.1), is the chromophore of the antenna protein phycocyanin [70] as well as of the cyanobacterial phytochrome Cph1 [71].

Tetrapyrrole moieties are known to adopt a helical structure in solution [23, 72, 73]. In the late 1990's, Schaffner and co-workers have studied PCB in $CDCl_3$:Pyridine-d_5 and CD_3OD solutions, where it adopts a helically coiled form with an (all-*Z*, all-*syn*)-conformation [24]. In the case of phycocyanobilin dimethyl ester, two types of coiled tetrapyrrolic moieties are present in $CDCl_3$ and CD_2Cl_2 solutions at low concentration: a helically coiled form and another form characterized by some degree of stretching of the chain.

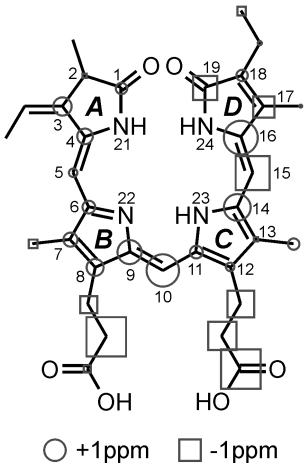


Figure 2.1: Structure of phycocyanobilin in the *ZZZsss* geometry as determined in solution [24]. The differences in the ^{13}C chemical shifts between the A and B forms (σ_{B}-σ_{A}) are projected on the chemical structure.

Upon increase in concentration, the relative proportion of the stretched form decreases and dimers of helically coiled PCBE appear [74]. In the same work, also a partial set of ^{13}C assignments has been obtained.

Semi-empirical AM1 studies [25, 75] and transient-grating spectroscopy [76] on PCB have proposed that three families of ground-state conformers coexist in solution. The predominant family adopts a cyclic-helical conformation (*ZZZsss*) with two types of helices, a right-handed (**P**) and a left-handed (**M**) helix [23, 24]. The other minimum-energy structures are obtained by rotation around the single bond of the C5 and C10 methine bridges, leading to two partially extended *ZZZass* and *ZZZsas* conformations [25, 75]. However, a precise structural analysis of PCB and its dimethyl ester is difficult because of the dynamics between the many possible conformations, the complex solvent effects and the limited solubility in most common solvents. Therefore, a structural analysis in the solid state provides a possibility to overcome these problems.

Although the 1,19-dioxobilin family has been intensively studied by X-ray crystallography [77], no description of PCB in its crystalline state is available yet. MAS NMR [78] has been developing to a method allowing for structure determination of aggregates [79], disordered systems [80] and membrane

proteins [81, 82]. In this chapter, the structure of PCB in microcrystalline samples is analyzed by a combination of MAS NMR and quantum mechanical calculations.

2.2 Results

2.2.1 ^{13}C chemical shift assignment

The one-dimensional ^{13}C CP/MAS spectrum of PCB in its microcrystalline state is shown in Figure 2.2. Although PCB contains 33 carbon atoms, around 45 centerbands are observable in the ^{13}C CP/MAS spectrum. The spinning sidebands have been determined by experiments at other spinning frequencies (data not shown) and are indicated with asterisks. PCB contains 11 aliphatic carbons in the side-chains, while 14 signals arising from the aliphatic carbons are observed between 0 and 40 ppm. Similarly, the carbonyl/carboxyl region of the spectrum (170-180 ppm) shows 6 signals that correspond with the response from 4 carbonyl carbons. In the aromatic region of the spectrum between 120 and 160 ppm, the signals of the pyrrole carbons strongly overlap, making the determination of the exact number of carbons involved difficult. On the other hand, in the region of methine carbons (120-80 ppm), at least five signals appear.

Liquid-state ^{1}H-^{13}C heteronuclear single quantum coherence and heteronuclear multiple bond correlation NMR spectra obtained in CD_3OD are shown in Appendix A (Fig. A.1). An almost complete set of ^{13}C assignments is presented in Table 2.1. While the solution spectra do not show any doubling of signal, the solid-state NMR data exhibit resonances which are clearly split. For instance, the liquid-state NMR spectrum of PCB exhibits signals at 98.3, 113.4 and 176.0 ppm, which were assigned to C15, C10 and C19, respectively. Similar resonances are present in the CP/MAS spectrum, however, these resonances are clearly doubled (96.0 and 93.6, 114.5 and 112.2, 173.7 and 172.0 ppm). The Lorentzian deconvolution of these doubled resonances (data not shown) reveals that the peak area ratios of all these doublets are 1:1. The observation of a consistent set of doubled signals in a 1:1 area ratio in the 1D CP/MAS NMR spectrum provides convincing evidence for the presence of two inequivalent forms of PCB in equal proportions in the microcrystal.

The 2D ^{13}C-^{13}C RFDR MAS NMR spectrum of the u-[^{13}C,^{15}N]-PCB has been recorded in order to separate and assign the carbon resonances (Fig.

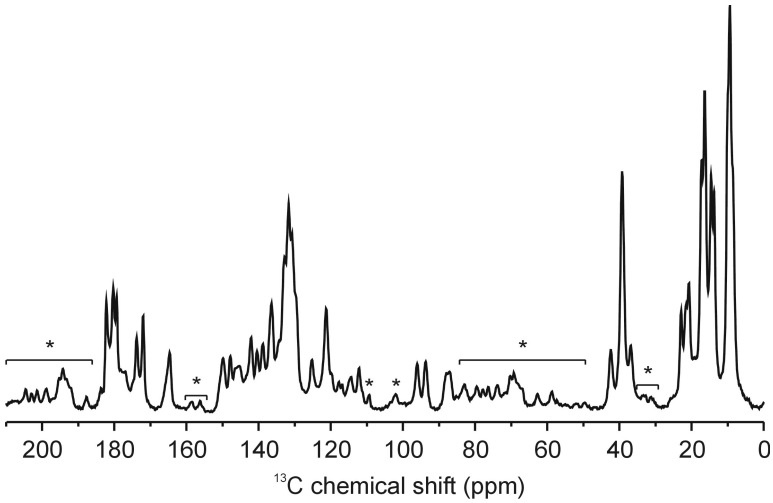


Figure 2.2: 1D ^{13}C CP/MAS NMR spectrum of PCB obtained at 17.6 T, 277 K and 11800 Hz. The asterisks indicate the spinning sidebands.

2.3). The 2D spectra unambiguously confirm the presence of two PCB forms, named A and B, in the microcrystal (Table 2.1). To illustrate the assignment procedure, the correlation network of the A form of the PCB spin system is indicated in Figure 2.3. The resonance at 173.7 ppm, correlating with two aromatic carbons (132.0 and 140.1 ppm) as well as with three aliphatic carbons (10.5, 14.3 and 17.0 ppm), can be assigned in a straightforward manner to the C19 carbon atom of the carbonyl moiety of the ring ***D***. The resonances of the C17 and C18 atoms can be assigned *via* their correlations with the aliphatic carbons atoms. The C16 and C17 spin systems correlate weakly, contrary to the correlations observed for the methine bridge C15, allowing for the assignment of the carbons C16, C15 and C14. For the assignment of the signals in the particularly crowded correlation area of the carbons C11, C12, C13, C14, the cross-peaks with the aliphatic carbons $C13^1$ and $C12^1$ are essential. The correlation peaks of the carbons between C9, C10 and C11 are nicely resolved and provide clear assignments of the carbons forming the C10 methine bridge. The good resolution of the response from the carbon atoms of rings ***A*** and ***B*** (C1 to C9) allows for the unambiguous assignment of the resonances. The signals of C1/C2 were resolved from $C8^2$/$C8^3$ and $C12^2$/$C12^3$ by the correlations with $C2^1$, C3 and C4. Finally, the correlation network between the aromatic and the side-chain carbons is shown in the up-

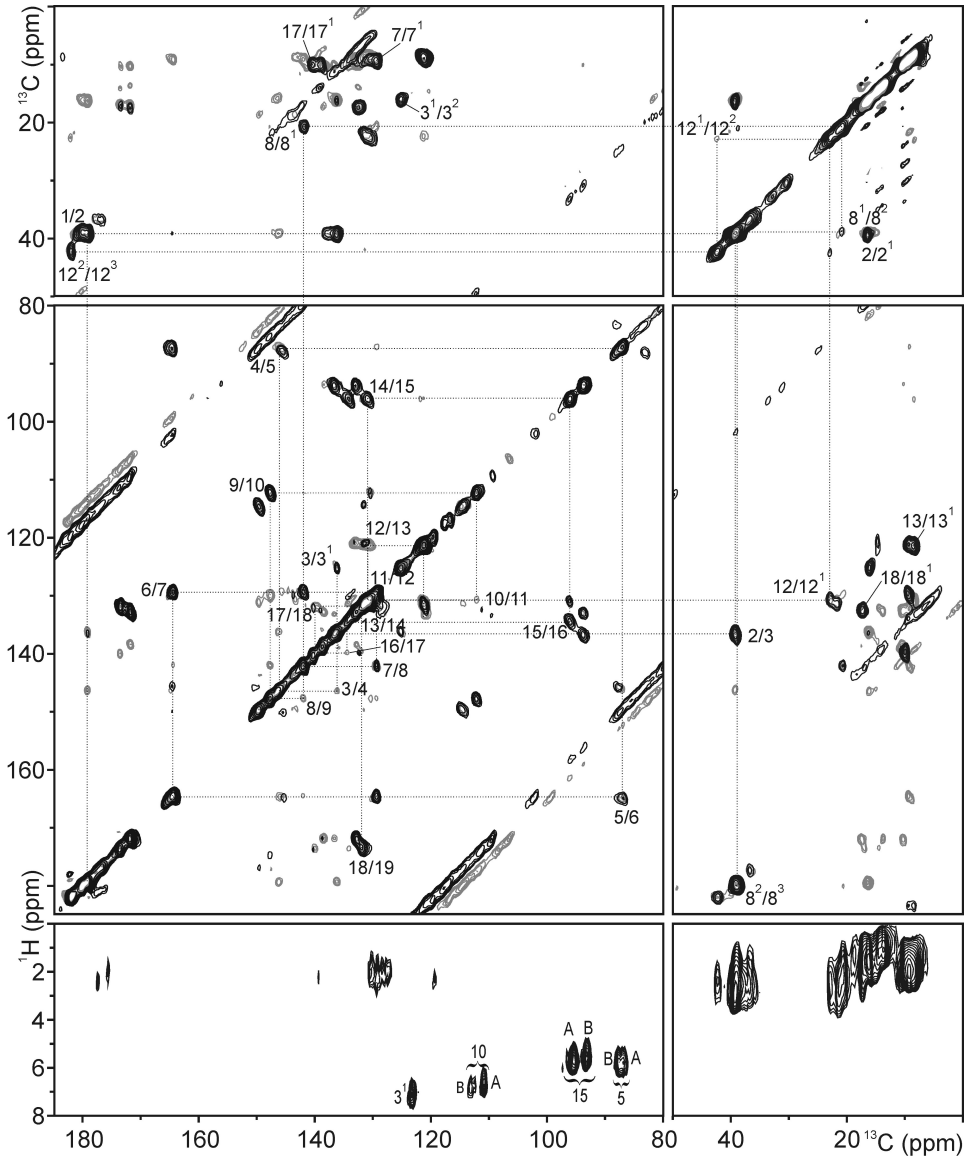


Figure 2.3: The upper panels show the contour plots of ^{13}C-^{13}C RFDR MAS NMR spectrum of u-[^{13}C,^{15}N]-PCB recorded in a field of 17.6 T using spinning frequencies of 11800 Hz (black) and 12500 Hz (grey), and mixing times of 1.8 ms and 3.2 ms, respectively. The lower panels represent the contour plot of the ^{1}H-^{13}C FSLG MAS NMR dipolar correlation spectrum at a spinning frequency of 11800 Hz.

Position	σ_{liq}	σ_A	σ_B	σ_B-σ_A
C1	181.0	179.4	180.3	0.9
C2	39.0	39.3	39.0	-0.3
$C2^1$	15.8	16.3	16.3	0.0
C3	136.7	136.2	137.5	1.3
$C3^1$	124.3	125.2	125.2	0.0
$C3^2$	14.8	16.1	16.1	0.0
C4	147.6	146.2	147.3	1.1
C5	88.5	87.1	88.0	0.1
C6	166.1	164.7	165.6	0.9
C7	132.4	129.5	130.5	1.0
$C7^1$	9.4	9.3	8.7	-0.6
C8	144.8	142.1	143.3	1.2
$C8^1$	21.7	20.7	18.8	-1.9
$C8^2$	38.8	38.6	36.6	-2.0
$C8^3$	179.3	180.5	177.7	-2.8
C9	n.d.	147.8	149.5	1.7
C10	113.4	112.2	114.5	2.3
C11	133.2	130.6	131.5	0.9
C12	134.8	130.8	131.4	0.6
$C12^1$	21.4	22.8	21.6	-1.2
$C12^2$	38.5	42.4	39.6	-2.8
$C12^3$	179.1	182.2	181.7	-0.5
C13	125.1	121.3	121.0	-0.3
$C13^1$	8.8	8.4	9.2	0.8
C14	133.2	131.1	133.0	1.9
C15	98.3	96.0	93.6	-2.4
C16	138.3	134.3	136.7	2.4
C17	142.9	140.1	138.6	-1.5
$C17^1$	9.3	10.5	10.3	-0.2
C18	133.8	132.0	132.8	0.8
$C18^1$	17.3	17.0	17.3	0.3
$C18^2$	13.3	14.3	13.7	-0.6
C19	176.0	173.7	172.0	-1.7

Table 2.1: ^{13}C chemical shifts of PCB in CD_3OD solution (σ_{liq}) and of the two sets of signals observed in the solid-state (σ_A and σ_B).

per left and middle right panels. The high resolution of these signals allows for the assignments of most of the side-chain carbon atoms. However, the correlation peaks of the carbon atoms of the propionic acid side-chains are poorly resolved in the RFDR spectrum.

A PDSD spectrum was collected to resolve the correlation networks of the propionic acid side-chain carbons (Fig. A.2). The resolution of the correlation signals is improved by the PDSD sequence and all side-chain carbon atoms can be unambiguously assigned (Table 2.1). Interestingly, the correlation peaks of the pyrrole rings ***A*** and ***B*** of the B form, in particular for the carbon

atoms C1 to C8, are significantly broader than the corresponding signals of the A form. The correlation peaks may be affected by dynamics, suggesting different mobility in the region of pyrrole rings ***A*** and ***B***.

The 2D frequency-switched Lee-Goldburg heteronuclear ^{1}H-^{13}C correlation spectrum of the u-[^{13}C,^{15}N]-PCB using a CP contact of 256 μs is presented in the lower panels of the Figure 2.3. Spectra obtained with CP contact times of 512 and 1024 μs are shown in Appendix A (Figs. A.3A and B, respectively). In the left panel, the proton resonances correlating with the methine bridge carbons are readily resolved. In line with the doublings observed for the carbon response, also the proton signals exhibit different chemical shifts in the A and B forms (Table 2.2). The chemical shifts of the protons bound to the carbon atoms C10 (6.4 and 6.6 ppm) and C15 (5.5 and 5.3 ppm) are clearly different in the A and B forms, while the protons attached to the carbons C3^{1} and C5 exhibit a similar chemical shifts in both A and B forms (6.8 and 5.5 ppm, respectively). Moreover, the H10 ^{1}H-^{13}C correlation signal of the A form is more intense than in the B form, suggesting that the proton at C10 has a different ^{1}H environment in A and B forms. The correlations with saturated carbons are depicted in the right panel. The small ^{13}C chemical shift dispersion of the methyl groups results in strongly overlapping signals, which cannot be assigned.

2.2.2 ^{15}N chemical shift assignment

The ^{15}N CP/MAS spectrum of u-[^{13}C,^{15}N]-PCB is shown in Figure 2.4. Three strong resonances at 154.2, 150.4, 133.1 ppm are dominating. Due to their chemical shifts and their anisotropy pattern with modest sideband intensities, these three signals originate from protonated nitrogen atoms [83, 84]. On the other hand, the centerband resonance at 260.8 ppm having much lower intensity arises from an unprotonated nitrogen atom. The anisotropy pattern of this signal shows intense spinning sidebands. Contrary to the carbon spectra, the ^{15}N resonances are not clearly split. However, the peak at 154.2 ppm exhibits a shoulder, which can be resolved by Lorentzian deconvolution as a signal at 156.9 ppm. The two other resonances of protonated nitrogen atoms can be fitted sufficiently with a single Lorentzian function (data not shown).

The 2D ^{15}N-^{13}C correlation spectrum of u-[^{13}C,^{15}N]-PCB is shown in Figure 2.5. ^{15}N-^{13}C heteronuclear correlations obtained by a double CP experiment allow to assign the ^{15}N resonances using the ^{13}C assignment (Table

Position	σ_{liq}	σ_A	σ_B	σ_A-σ_B
H2	3.21	n.d.	n.d.	
$H2^1$	1.34	n.d.	n.d.	
$H3^1$	6.54	6.8	6.8	0.0
$H3^2$	1.93	1.9	1.9	0.0
H5	5.99	5.5	5.5	0.0
$H7^1$	2.08	1.8	1.8	0.0
$H8^1$	2.93	2.1	1.4	0.7
$H8^2$	2.43	n.d.	n.d.	
$H8^3$	n.d.	n.d.	n.d.	
H10	6.96	6.4	6.6	-0.2
$H12^1$	2.98	2.0	2.7	-0.7
$H12^2$	2.45	2.3	n.d.	
$H12^3$	n.d.	n.d.	n.d.	
$H13^1$	2.16	n.d.	n.d.	
H15	6.14	5.5	5.3	0.2
$H17^1$	2.14	1.7	1.6	0.1
$H18^1$	2.30	1.4	1.5	-0.1
$H18^2$	1.09	1.1	0.8	0.3

Table 2.2: ^{1}H chemical shifts of PCB in CD_3OD solution (σ_{liq}) and of the two sets of signals observed in the solid state (σ_A and σ_B).

2.3). The ^{15}N-^{13}C heteronuclear correlation peaks allow for an unambiguous assignment of all nitrogen atoms. The up-shifted signal at 133.1 ppm is assigned to nitrogen N24, as shown by the correlation to the carbons C16 and C19. Similarly, the resonances at 150.4 and 154.2 ppm are assigned to N23 and N21, respectively. The signal at 260.8 ppm is attributed to nitrogen N22, revealing that the unprotonated nitrogen is located at the ring ***B*** of the tetrapyrrole moiety.

Finally, the 2D ^{1}H-^{15}N heteronuclear correlation FSLG spectrum of the u-[^{13}C,^{15}N]-PCB has been recorded (Fig. A.4). The hydrogens bound to N21 and N24 exhibit chemical shifts at 12.2 and 11.2 ppm, respectively, while the proton bound to N23 is slightly upshifted at 10.7 ppm.

Despite the presence of the shoulder at 156.9 ppm, no correlation peak was found at this frequency neither in the ^{1}H-^{15}N nor in the ^{15}N-^{13}C heteronuclear correlation spectrum. The ^{13}C signals of the ring ***A*** are broad in the B form. The ^{15}N signal at 156.9 ppm may arise from N21 of the PCB moiety in the B form. The slightly different ^{15}N chemical shifts of N21 in the A and B forms may be due to a different geometry of the ring ***A*** and/or a different hydrogen-bonding interaction of this nitrogen in the B form.

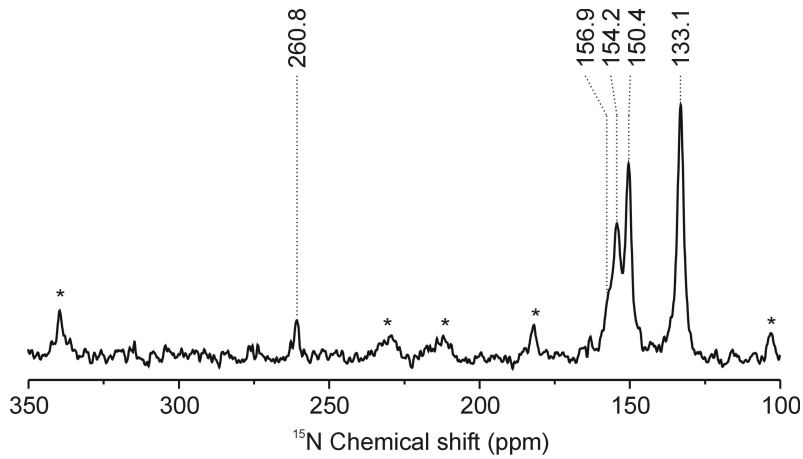


Figure 2.4: ^{15}N CP/MAS NMR spectrum of u-[^{13}C,^{15}N]-PCB recorded at 277 K in a field of 17.6 T using a spinning frequency of 7 kHz. The spinning sidebands are indicated with asterisks.

2.3 Discussion

2.3.1 PCB tautomers

The ^{15}N CP/MAS NMR spectrum of PCB reveals that three nitrogen atoms are protonated. For asymmetrically substituted bilin derivatives, such partitions of acidic hydrogen atoms bound to nitrogen lead to a total of twenty potential tautomers (four bis-lactam, twelve *mono*-lactam and four *bis*-lactim forms). The 2D ^{15}N-^{13}C correlation spectrum in Figure 2.5 demonstrates that both outer ring nitrogens, *i.e.*, N21 and N24, are protonated. Hence, the PCB molecules are in a *bis*-lactam state and the potential tautomerization modes are restrained to the dipyrrin types of tautomerization involving the nitrogens of rings ***B*** and ***C***. It has been shown that PCB-like compounds adopt a helical conformation in which the inner (N$\cdots$H—N) hydrogen-bonding plays a predominant role in the stabilization of the molecular structure [85, 86]. On the other hand, the tautomerism within the central rings of asymmetrically substituted 1,19-dioxobilin, *i.e.*, either the N22$\cdots$H—N23 or the N22—H$\cdots$N23 tautomer, is still under debate [77, 87–89]. The ^{13}C and ^{15}N CP/MAS NMR data shown in this chapter (Figs. 2.3 and 2.5) allow for an unambiguous assignment of all nitrogens of PCB and show that the pyrrolenine nitrogen atom is exclusively placed on the inner ring ***B***.

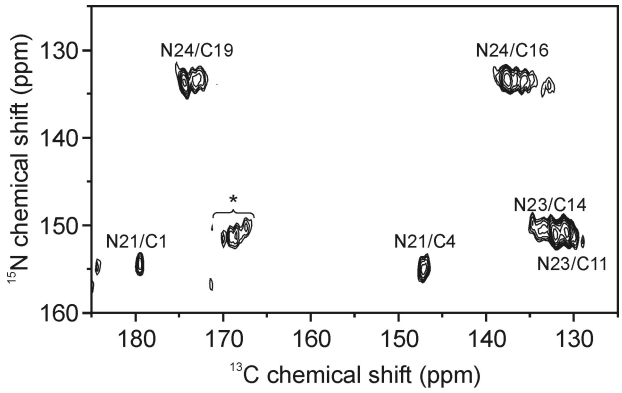


Figure 2.5: Contour plot of the 2D ^{15}N-^{13}C heteronuclear dipolar correlation spectrum of u-[^{13}C,^{15}N]-PCB recorded at 277 K in a field of 17.6 T using a spinning frequency of 8 kHz. The spinning sidebands are indicated with asterisks.

2.3.2 Differences between forms A and B

The ^{13}C NMR study of PCB in its microcrystalline state reveals the presence of two PCB forms in the microcrystal. The differences in the ^{13}C chemical shifts are mainly observed around the C10 and C15 methine bridges and at both of the propionic acid side-chains, while only little variation in ^{13}C chemical shift was detected for the C1 to C7 region of the molecule (Fig. 2.1). In addition, the resolved proton signals for the hydrogens at the C3^1 and C5 positions exhibit the same chemical shift in both A and B forms. Unlike the H3^1 and H5, the H10 and H15 protons show some difference in their chemical shifts (0.20 and 0.15 ppm, respectively, Table 2.2). Taking the ^{13}C and ^{1}H chemical shift variation between A and B forms into account, it can be concluded that PCB adopts two geometries in the microcrystal. The geometry of the ring ***A*** and the C5 methine bridge appear similar in both forms A and B, while the remaining parts of PCB are probably distinguished by the torsional angles about the single bonds at the methine bridges C10 and C15.

In addition to steric constraints, hydrogen-bonding may play an important role in the stabilization of a specific conformation. Due to the presence of the two carboxylic groups at the C8^3 and C12^3 positions, hydrogen-bonds between the propionic acid chains are possible. The pronounced ^{13}C chemical shift variations observed at the propionic acid side-chain, in particular at

Position	σ_{liq}	$\sigma_{A/B}$
N21	157.9	154.7
N22	245.5	260.8
N23	153.0	150.3
N24	131.3	133.1

Table 2.3: ^{15}N chemical shifts of PCB in CD_3OD solution and solid state.

the $C8^2$, $C12^1$, $C12^2$ and $C12^3$ positions, suggest conformational differences originating from different hydrogen-bonding networks between the carboxylic groups. Finally, the broad ^{13}C resonances of the carbon atoms $C8^1$ and $C12^3$ of the B form suggest a high mobility of these side-chains.

2.3.3 PCB Dimers

X-ray crystallographic analyses of open-chain tetrapyrroles like 2,3 dihydrobilatriene-abc derivatives [90, 91] and biliverdin dimethylester [85] have shown that these compounds form dimers in the crystalline state. The dimers are stabilized by intermolecular hydrogen-bonding interactions between the N–H and C=O groups of the outer pyrrole rings. In the case of PCB, the ^{13}C NMR data show unambiguously that the two A and B forms are present in equal ratio in the microcrystal. The comparison of the ^{13}C chemical shifts of PCB obtained by liquid-state and solid-state NMR suggests that the helical (all-*Z*, all-*syn*)-geometry is conserved in both A and B forms in the microcrystal. In addition, it has been suggested that dimerization of PCBE occurs in solution [74, 89]. Despite the different terminal group of the side-chain at C8 and C12 in PCB (acid) and PCBE (ester), there is converging evidence that the dimerization is likely to occur for PCB in the solid state.

The formation of intermolecular N—H$\cdots$C=O hydrogen-bonds may play a role in the stabilization of PCB in a specific geometry. Four types of dimers involving intermolecular hydrogen bonds between the outer rings can potentially be formed (***A***–***A***', ***D***–***D***', ***A***–***D***' and ***D***–***A***').

It is known that the helical structure of 1,19-dioxobilins are determined by the hydrogen-bonding interaction between the unprotonated inner ring nitrogen and the hydrogen atoms of two close-by protonated nitrogen atoms [77]. It has been shown in section 2.2.2 that N22 is unprotonated in both A and B forms. Hence, in the case of PCB, this interaction is of the form N21—H$\cdots$N22$\cdots$H—N23. Thus, dimerization involving the rings ***D*** is the

most likely to occur.

2.3.4 Geometry optimization and dimer characterization

Quantum chemical density functional theory (DFT) calculations using the B3LYP exchange-correlation functional [92] in combination with the 6-31G* basis set [93] have been used for geometry optimization (Dr. Franz Mark, personal communication). The DFT study reveals the existence of two low-energy families of PCB dimers. The first family of dimers involves hydrogen-bonding interactions between the rings ***D*** and ***D***' (Fig. 2.6A). One of the subunits in the dimers forms a **P** helix, the other an **M** helix. The two PCB moieties are bound together by means of two hydrogen-bonds (N24—H$\cdots$O19' and O19$\cdots$H'—N24') with distances of 2.83 and 2.88 Å. Small differences in torsional angles of the double and single bonds at the C15, C10 and C5 methine bridges are due to the intermolecular steric interactions. Hence, the two monomers have a similar helical shape but are not symmetric.

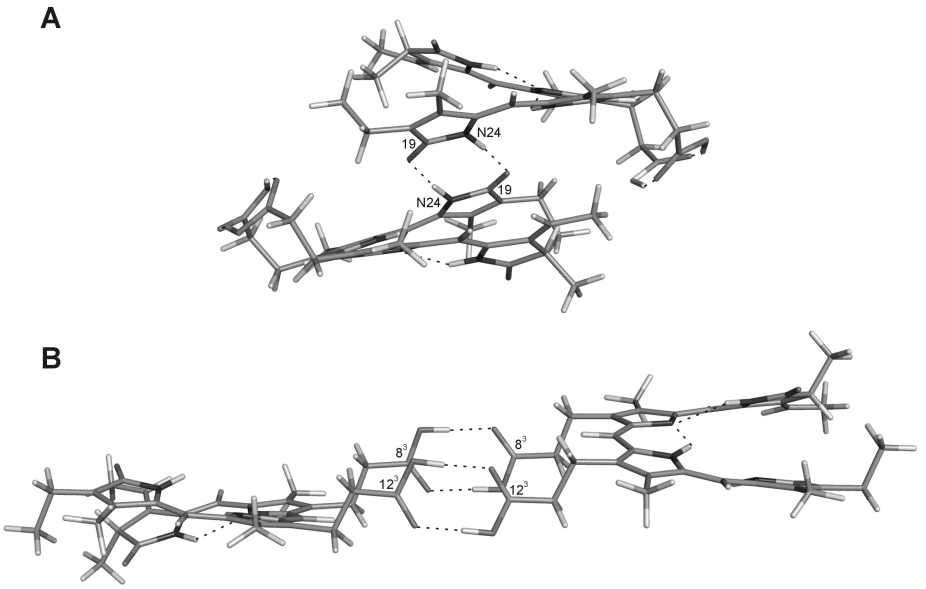


Figure 2.6: View of the low-energy families of dimers ***D***–***D***' (**A**) and P–P' (**B**) obtained by geometry optimization at the B3LYP/6-31G* level of theory.

The formation of the second lowest-energy family of dimers, called P–P', occurs *via* the propionic side-chains of the PCB molecules. Hence, the geometry of the three methine bridges of each monomer P is solely governed by the intramolecular hydrogen-bonding system N21—H$\cdots$N22$\cdots$H—N23 and by the intramolecular steric interactions between its side-chains without being significantly affected by the other monomer P'. In the lowest-energy P–P' dimer, the two subunits are composed of two enantiomeric **M** helical monomers (Fig. 2.6B).

Due to the enantiomeric relation between the P and P' monomer, the NMR spectrum of this family would consist of a unique set of chemical shifts. On the other hand, the two slightly different monomers found in the ***D***–***D***' family would generate two sets of chemical shifts. Since the MAS NMR analysis of PCB in its microcrystalline state demonstrates the presence of two forms, it is most likely that the two sets of chemical shifts are due to the occurrence of the ***D***–***D***' family of dimers in the crystal.

2.4 Materials and methods

2.4.1 Sample preparation

Uniformly [^{13}C,^{15}N]-labeled PCB was obtained by growing axenic cultures of *Synechocystis* sp. PCC 6803 cells at room temperature in a modified BG11 medium under constant illumination with continuous white light [94]. Cells reached a stationary phase after 3-4 weeks ($OD_{750} \sim 3$) and were harvested by centrifugation at 5000g for 20 min at 4 °C. The pellet was resuspended in 30 mL of 0.75 M K_nPO_4 buffer (pH 7) and 5 mM EDTA (pH 8), and broken with a French press (two passages, 21500 N). The cellular debris was pelleted at 25000g for 30 min at 4 °C. Ammonium sulfate was added to the supernatant (3/2, v/v) and the sample was spun in a swing-out rotor for 20 min at 5000 rpm (4 °C). The pelleted sample was washed with 30 mL of ice-cold methanol and centrifuged at 5000 rpm for 10 min. Pellets were resuspended in methanol (1/15, v/v), incubated 18 h at 54 °C, and centrifuged (15 min, 5000 rpm, 4 °C). The supernatant was collected and concentrated to 5 mL. The residue was purified by reverse-phase HPLC using published procedures [46].

2.4.2 Mass spectrometry

The ^{13}C and ^{15}N isotope enrichments were measured by mass spectrometry. PCB was diluted in methanol containing 1% acetic acid. The mass spectrum was acquired in positive ion mode by direct infusion (5 $\mu L \cdot min^{-1}$) using a LTQ FT hybrid mass spectrometer (ThermoFischer, Bremen, Germany) equipped with an electrospray ionization source. The capillary was typically held at 3.5 kV, the transfer capillary was maintained at 280 °C and the tube lens was set to 240 V. 15 scans were accumulated for each experiment. A ^{13}C and ^{15}N isotope enrichment of about 90% has been deduced from the mass spectrum.

2.4.3 NMR experiments

For the MAS NMR measurements, about 2 mg of u-[^{13}C,^{15}N]-PCB was placed into a 4-mm CRAMPS rotor. All MAS NMR experiments were performed at 277 K with an Avance 750 spectrometer (Bruker BioSpin, Karlsruhe, Germany), equipped with a triple-resonance MAS probe head and operating at a resonance frequency of 750.1 MHz for ^{1}H, 188.6 MHz for ^{13}C and 76.0 MHz for ^{15}N. RFDR and PDSD pulse sequences were used to record ^{13}C-^{13}C homonuclear correlations. For both 2D experiments, proton $\pi/2$ pulses were set to 3.1 μs and a CP contact time of 2.0 ms was used. A ramped CP sequence (100-80%) with a cycle delay of 1 s was applied. Heteronuclear two-pulse phase modulation decoupling was applied during acquisition [65]. For the RFDR experiment, a continuous wave decoupling of 80.6 kHz was used to decouple the protons during the mixing time. For the PDSD experiment, the proton decoupling was switched off during the spin diffusion mixing period to obtain ^{1}H-mediated transfer of ^{13}C polarization along the molecular network. Heteronuclear ^{1}H-^{13}C and ^{1}H-^{15}N correlations were obtained by FSLG experiments using short CP times of 256 μs and a ^{1}H $\pi/2$ pulse length of 3.1 μs. The ^{1}H chemical shift scale was calibrated from a FSLG spectrum of solid tyrosine·HCl salt.

^{15}N-^{13}C double CP/MAS spectrum of u-[^{13}C,^{15}N]-PCB was recorded with the same spectrometer using a triple resonance CP-MAS probe head with a spinning rate of 8 kHz. ^{15}N polarization was created with a 80-100% ramped amplitude CP matching and a contact time of 2.0 ms. During ^{15}N evolution TPPM decoupling with a RF field strength of 81 kHz was used. For the CP transfer from ^{15}N nuclei to the ^{13}C aromatic carbons, the ^{15}N carrier

frequency was placed at 143 ppm [95]. During the dipolar contact time of 2.0 ms for the ^{15}N-^{13}C transfer, a weak RF field of 22.5 kHz for ^{15}N was employed. The RF field strength for ^{13}C was 31 kHz for the ^{15}N-^{13}C band selective CP. During the ^{15}N-^{13}C transfer, continuous wave decoupling was applied at the ^{1}H frequency. TPPM was employed for decoupling during acquisition. ^{15}N chemical shifts were referenced to liquid ammonia with use of an external standard of ^{15}N-glycine (34.3 ppm).

Chapter 3

MAS NMR on the Pr and Pfr parent states

3.1 Introduction

A characteristic feature of all phytochromes is the photoreversibility between two states: the absorption of red light initiates photochemical activity of the thermally stable Pr state ($\lambda_{max} \sim 660$ nm) which travels through a series of intermediates [96] and eventually generates the far-red absorbing Pfr state. The Pfr state ($\lambda_{max} \sim 710$ nm), with a moderate thermal stability of several hours to days, is converted back to Pr upon absorption of a far-red photon. The origin of this red shift is not known. All phytochromes bind an open-chain tetrapyrrole (bilin) as a chromophore, whose photochemistry triggers the conversion between the Pr and Pfr states. The X-ray structures of the chromophore binding PAS-GAF bi-domain of *Deinococcus radiodurans* [18] and *Rhodopseudomonas palustris* [52], both assembled with biliverdin, have been reported. The structure of a complete PAS-GAF-PHY sensory module of Cph1 from *Synechocystis* sp. PCC 6803 phytochrome in its Pr state demonstrated that the PCB cofactor is completely sealed from access to bulk solvent [53]. Although a comparison between these 3D structures reveals some differences of the chromophore binding pocket, most of the chromophore-protein interactions are conserved. In all crystal structures, the open-chain tetrapyrrole chromophore has been reported to adopt a *ZZZssa* geometry of the three methine bridges.

The chromophore in different phytochromes has been intensively studied by various spectroscopic methods. It is commonly accepted that the conversion from Pr to Pfr is initiated by a $Z \rightarrow E$ photoisomerization of the methine bridge between rings ***C*** and ***D*** [29, 40, 43, 97]. However, the exact geometry of the chromophore in the Pfr state and the role of the chromophore binding pocket in the phototransformation have yet to be established.

Little is known about the details of the photochemical machinery that allows for intramolecular signal transduction from the chromophore to the protein surface. Mutational studies on Cph1 [19, 98] have demonstrated the crucial role of Asp-207 (Cph1 numbering of residues is used throughout the chapter) for intramolecular signal transduction (Fig. 1.6). It has been proposed that in Cph1 Tyr-176, whose side-chain is close to ring ***D***, acts as a molecular gate to photoisomerization of the C15=C16 double bond [44]. In the bacteriophytochrome RpBphP2, two tyrosine residues, Tyr-207 and Tyr-272 that equivalent to Tyr-198 and Tyr-263 in Cph1, respectively, are thought to play an important role during the Pr → Pfr conversion [52].

CP/MAS NMR has evolved into a uniquely versatile tool for the structure elucidation in systems of high molecular mass and solid materials. In conjunction with selective isotope labeling, CP/MAS NMR allows for the study of large protein complexes down to the atomic level [99]. In this chapter, the N-terminal sensory modules of the cyanobacterial phytochrome Cph1 and the 65-kDa fragment of oat phytochrome A have been studied by ^{13}C and ^{15}N CP/MAS NMR. These phytochromes were assembled *in vitro* with uniformly ^{13}C- and ^{15}N-labeled PCB cofactor. In this way, selective observation of the chromophore in the protein matrix can be achieved. A full NMR analysis of the cofactor in both Pr and Pfr states is presented. Significant changes around ring ***D*** and the propionic side-chain of ring ***C*** are observed and explained by a model for signal transduction.

3.2 Results

3.2.1 Assignments of ^{13}C CP/MAS NMR spectra of Pr and Pfr states in Cph1Δ2

The 2D ^{13}C-^{13}C DARR spectrum of the u-[^{13}C,^{15}N]-PCB-Cph1Δ2 in the Pr state was recorded with two ^{1}H-^{1}H mixing times of 5 ms and 50 ms (Fig. 3.1, black and grey, respectively). Using a 50 ms mixing time, the carbon

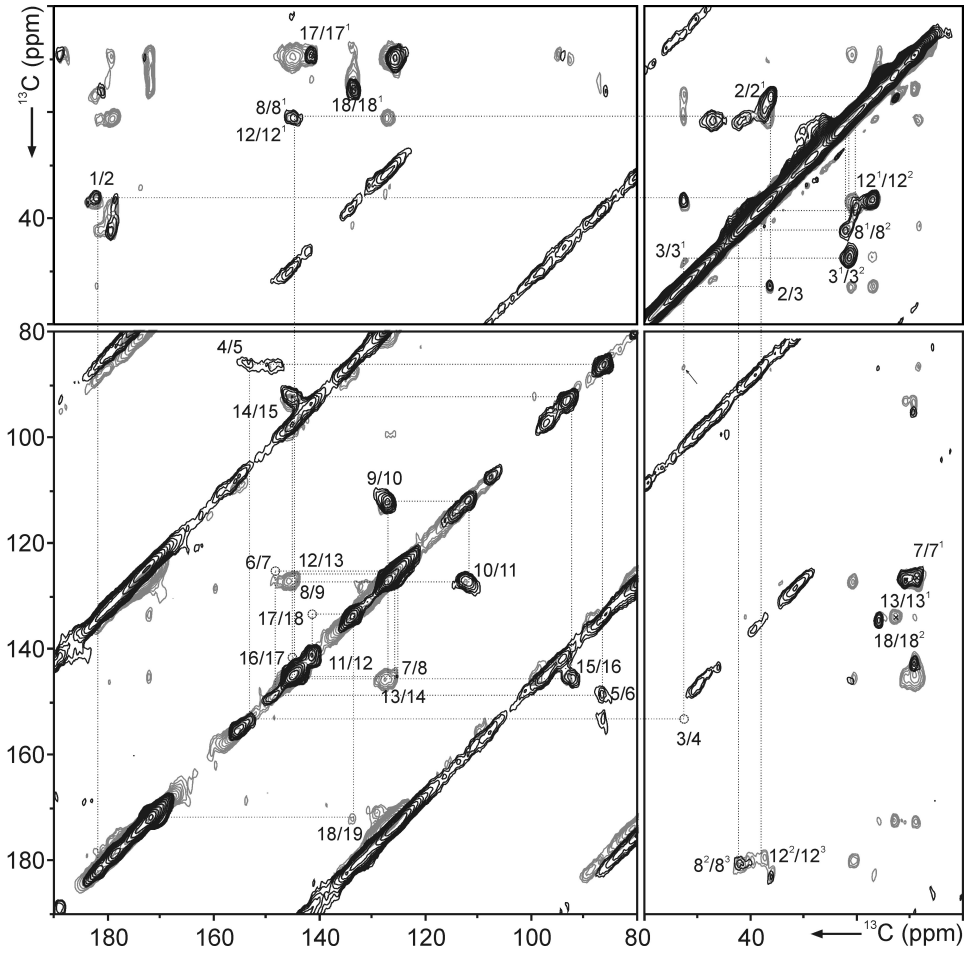


Figure 3.1: Contour plot of the 2D ^{13}C-^{13}C DARR NMR spectra of u-[^{13}C,^{15}N]-PCB-Cph1Δ2 in the Pr state. Proton mixing times of 5 and 50 ms were used for the Pr datasets (black and grey, respectively) recorded at 233 K with spinning frequencies of 9 and 10 kHz. The lines indicate sequences of nearest neighbor correlations.

resonance at 182.5 ppm correlates with two aliphatic carbons allowing for an unambiguous assignment of carbons C1, C2 and C2^1 (see Table 3.1). For carbons C1 and C2, a slight doubling is observed. The well resolved correlation peaks in the aliphatic region (60 to 0 ppm) reveal the correlation network between the C2, C2^1, C3, C3^1 and C3^2 carbon atoms. None of the DARR spectra displays the C3/C4 cross-peak, however, the C3/C5 correlation is visible using a mixing time of 50 ms. The assignment of position C5 has been

	Cph1Δ2			*phyA*65		
Position	Pr	Pfr	Pfr-Pr	Pr	Pfr	Pfr-Pr
C1	182.5	182.8	0.3	182.6	182.5	-0.1
$C1^a$	184.2	—	1.4	—	—	
C2	37.1	37.2	0.1	36.8	37.0	0.2
$C1^a$	38.1	—	-0.9	—	—	
$C2^1$	17.5	18.5	1.0	17.7	17.7	0.0
C3	53.4	54.3	0.9	53.9	53.9	0.0
$C3^1$	47.6	50.0	2.4	47.6	49.1	1.5
$C3^{1a}$	—	—	—	45.8	—	3.3
$C3^2$	21.8	21.4	-0.4	21.7	21.3	-0.4
$C3^{2a}$	—	—	—	23.0	—	-1.7
C4	153.9	154.0	0.1	n.d.	n.d.	
C5	87.1	88.5	1.4	85.8	87.1	1.3
C6	149.1	148.8	-0.3	n.d.	n.d.	
C7	126.1	126.1	0.0	124.7	124.6	-0.1
$C7^1$	9.2	9.3	0.1	7.2	7.5	0.3
C8	144.5	143.6	-0.9	146.4	143.4	-3.0
$C8^1$	22.7	23.1	0.4	21.8	23.0	1.2
$C8^{1a}$	21.5	—	1.6	—	—	—
$C8^2$	43.1	41.7	-1.4	41.5	41.1	-0.4
$C8^{2a}$	41.1	—	0.6	—	—	
$C8^3$	180.5	180.5	0.0	179.9	179.7	-0.2
$C8^{3a}$	179.7	—	0.8	—	—	—
C9	127.7	131.0	3.3	127.7	130.6	2.9
C10	112.7	112.3	-0.4	113.0	111.9	-1.1
C11	127.7	131.0	3.3	127.7	130.6	2.9
C12	145.5	145.8	0.3	146.4	144.5	-1.9
$C12^1$	21.1	20.6	-0.5	21.8	21.0	-0.8
$C12^2$	37.5	38.3	0.8	41.5	39.0	-2.5
$C12^3$	179.5	175.2	-4.3	177.5	174.7	-2.8
C13	126.3	130.6	4.3	123.7	130.1	6.4
$C13^1$	11.3	11.3	0.0	10.0	12.1	2.1
C14	145.7	151.5	5.8	146.6	150.5	3.9
C15	93.5	91.7	-1.8	93.3	92.3	-1.0
C16	145.7	151.1	5.4	146.6	150.5	3.9
C17	142.2	137.7	-4.5	142.6	138.6	-4.0
$C17^1$	9.8	10.1	0.3	10.3	10.3	0.0
C18	134.3	140.4	-6.1	133.3	140.1	6.8
$C18^1$	16.1	15.6	-0.5	16.6	n.d.	
$C18^2$	13.3	13.3	0.0	n.d.	n.d.	
C19	172.8	168.9	-3.9	172.4	169.6	-2.8

Table 3.1: ^{13}C chemical shifts obtained for Cph1Δ2 and *phyA*65 containing an u-[^{13}C,^{15}N]-PCB chromophore.

confirmed by a 1D ^{13}C CP/MAS NMR spectrum of the ^{13}C5-PCB-*phyA*65 (Appendix B, Fig. B.1). The C4/C5 and C5/C6 correlations are visible in the spectrum recorded with a short proton mixing time of 5 ms. The two

neighbors of carbon C5 are difficult to distinguish although a weak correlation with C7 suggests that ^{13}C6 resonates with a chemical shift of 149.1 ppm. The ^{13}C-^{13}C correlation network along the pyrrole rings ***B*** and ***C*** is shown in Figure 3.1 and allows for the assignment of the carbon atoms up to position C16. The C16/C17 and C17/C18 correlation peaks are weakly visible, the assignments of C17 and C18 have been obtained from the C18/C19 correlation as well as from the methyl and ethyl side-chain (C17^1, C18^1 and C18^2). The ^{13}C assignment reveals that the central rings ***B*** and ***C*** of the chromophore are highly symmetrical in the Pr state. The ^{13}C-^{13}C correlations in the aliphatic domain show a single correlation network for one of the propionic side-chains (23.1, 41.7 and 180.5 ppm) and a split correlation network for the second propionic side-chain (22.5, 42.8, 180.6 ppm, and 21.5, 41.1, 179.7 ppm). Since the C8/C8^1 and C12/C12^1 correlation signals overlap, the two propionic side-chains cannot be assigned unambiguously. However, the chemical shift differences occurring in comparison with the Pfr state (see below) make an assignment of the propionic side-chain with the single correlation network to carbon C12 more reasonable.

The 2D ^{13}C-^{13}C DARR spectra of Cph1Δ2 in the Pfr state have been recorded with two ^{1}H-^{1}H mixing times (5 and 50 ms) and are depicted in Figure 3.2 (black and grey, respectively). The ^{13}C assignments have been obtained in the same manner as for the Pr state. In the Pfr state, the C8/C8^1 and C12/C12^1 correlation peaks do not overlap. In addition, the C12/C13, C13/C13^1 and C13^1/C14 cross-peaks are visible in the 2D spectrum and allow for the unambiguous assignment of the two propionic side-chains. While in the side-chain of ring ***B*** two sets of chemical shifts appear for the Pr state, only a single set is detected for the Pfr state. This is similar to the observation of doubling at the ring ***A*** carbons C1 and C2. Since also optical spectroscopy, operating on a fast timescale, observes two distinguished forms of the PCB cofactor in the Pr state [100,101], it can be assumed that the two conformers coexist in solution. As the origin of this heterogeneity, mobility of the nearby N-terminal-helix (Thr-4 to Leu-18) that seals parts of the chromophore binding site along ring ***A*** and ***B*** can be postulated. The disappearance of the doublings in the Pfr state may be caused by a decreased mobility in this region, thus leading to conformational homogeneity.

A ^{1}H-^{13}C heteronuclear 2D spectrum of the region of the methine carbons of u-[^{13}C,^{15}N]-PCB in Cph1Δ2 is shown in Figure B.2. The signal labeled

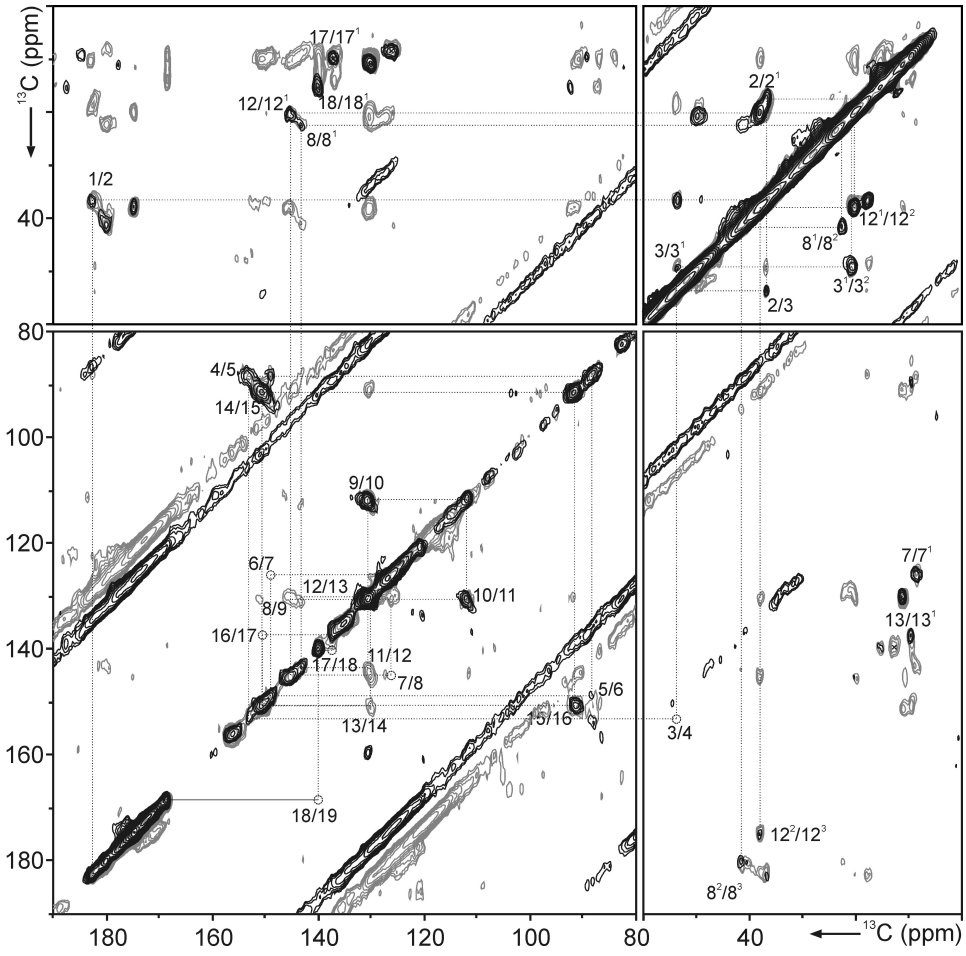


Figure 3.2: Contour plot of the 2D ^{13}C-^{13}C DARR NMR spectra of u-[^{13}C,^{15}N]-PCB-Cph1Δ2 in the Pfr state recorded at 233 K in a field of 17.6 T using proton mixing times of 5 and 50 ms (black and grey, respectively) and spinning frequencies of 9 and 10 kHz, respectively.

with an asterisk originates from the protein. The low-field response of H10 has also been observed previously for the Pr state by liquid-state NMR [102] and appears to be an intrinsic property of open-chain tetrapyrrole compounds [103]. Upon photoconversion to the Pfr state, the chemical shift of H5 remains unchanged, while at H10 and H15 high-field shifts of 0.4 ppm are observed. A shift for H15 can in principle be expected due to the isomerization of the C15=C16 double bond [103].

	Cph1Δ2				*phyA*65		
Position	Pr	Pfr	Pr-Pfr		Pr	Pfr	Pr-Pfr
N21	158.1	158.6	-0.5	}	159.5, 156.8	159.7, 157.3	
N22	160.5	155.8	4.7				
N23	147.0	142.6	4.4		146.7	143.5	3.2
N24	131.9	138.0	-6.1		133.6	137.7	-4.1

Table 3.2: ^{15}N chemical shifts obtained for Cph1Δ2 and *phyA*65 containing an u-[^{13}C,^{15}N]-PCB chromophore.

3.2.2 ^{15}N CP/MAS NMR of u-[^{13}C,^{15}N]-PCB-Cph1Δ2

The ^{15}N CP/MAS NMR spectra of the u-[^{13}C,^{15}N]-PCB-Cph1Δ2 in the Pr and Pfr states are presented in Figure 3.3, column A. The ^{15}N21-PCB was chemically synthesized and assembled to Cph1Δ2 to assign the ^{15}N response of the ring ***A*** nitrogen (Fig. 3.3B). The broad resonance at $\sim$ 120 ppm is due to the amide nitrogens of the protein backbone originating from ^{15}N nitrogens in natural abundance. The spectrum of the Pr state shows three distinct ^{15}N maxima at 159, 147 and 132 ppm, while the spectrum of pure Pfr exhibits three cofactor maxima at 158, 143 and 138 ppm. The asterisks indicate the position of protein backbone signals in natural abundance. A deconvolution using a Voigt function with a Lorentzian:Gaussian ratio of 1:1 was applied to resolve the overlapping signals and to obtain the accurate chemical shifts (Fig. B.3). The chemical shifts of the simulated chromophore peaks have been determined at (*i*) 160.5, 158.1, 147.0 and 131.9 ppm for Pr and (*ii*) 158.6, 155.8, 142.6 and 138.0 ppm for Pfr (Table 3.2).

The 1D ^{15}N spectra of ^{15}N21-PCB-Cph1Δ2 (Fig. 3.3B) reveal that the ring ***A*** nitrogen atom exhibits a chemical shift at around 158 ppm in both Pr and Pfr states. Thus the peaks at 158.1 and 158.6 ppm are assigned to the ring ***A*** nitrogen in the Pr and Pfr states, respectively. As shown in **Chapter 2**, the ring ***D*** ^{15}N of the u-[^{13}C,^{15}N]-PCB in its free state resonates with a chemical shift of 133.1 ppm. The ^{15}N signals at 132 and 138 ppm in the Pr and Pfr state are tentatively assigned to N24, while the peaks at 160.5 and 147.0 ppm in the Pr state and at 155.8 and 142.6 ppm in the Pfr state are attributed to the ^{15}N responses of rings ***B*** and ***C***. In both states, one of the inner ring ^{15}N signals appears downshifted by about 10 ppm in comparison with the other.

Since all nitrogens of the cofactor are protonated [39, 94, 104], the tetrapyrrole is positively charged in both Pr and Pfr states. The X-ray structure

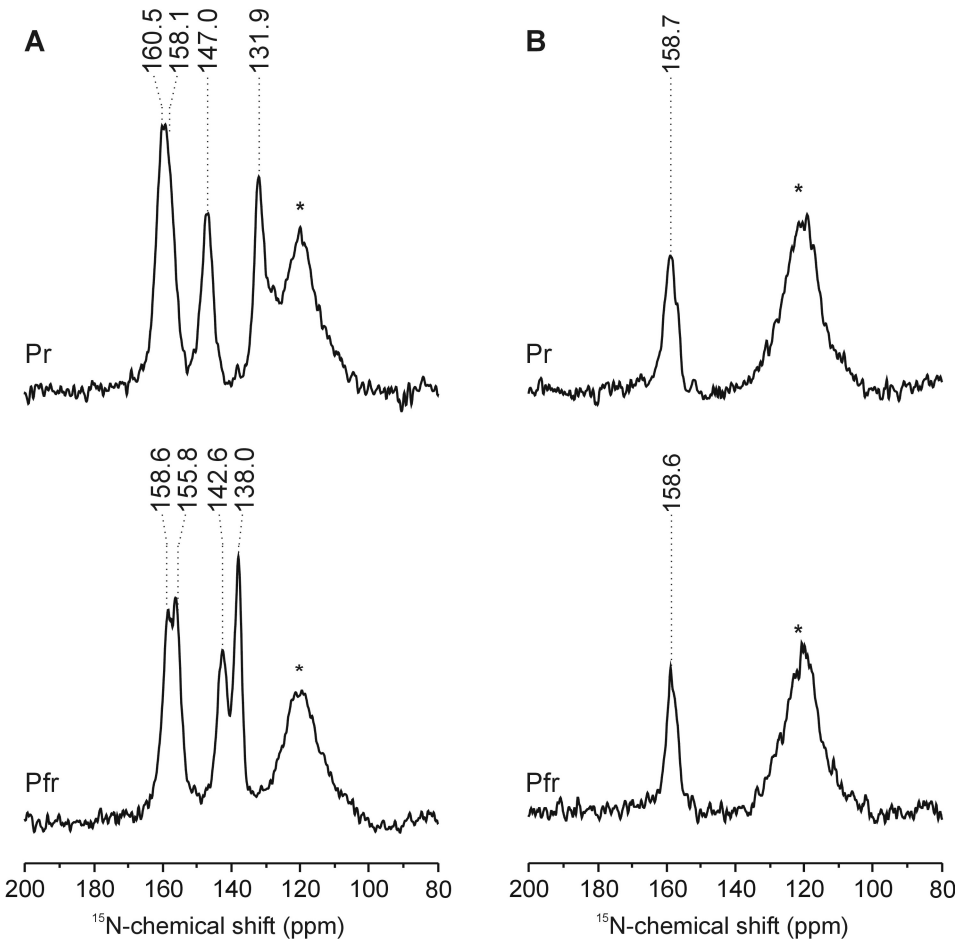


Figure 3.3: 1D ^{15}N CP/MAS NMR spectra of u-[^{13}C,^{15}N]-PCB-Cph1Δ2 (**A**) and ^{15}N21-PCB-Cph1Δ2 (**B**) recorded at 243 K in a field of 17.6 T and a spinning frequency of 8 kHz. The asterisks indicate the signal due to the protein backbone originating from ^{15}N nitrogens in natural abundance.

of Cph1 (PDB ID 2VEA) shows that the amide oxygen of Asp-207 is at hydrogen-bonding distance to N21, N22 and N23. The distance between this oxygen and N22 is as short as 2.72 Å, *i.e.*, three time shorter than the standard deviation of the average N$\cdots$O distance in a N—H$\cdots$O hydrogen-bonding interaction [105]. The asymmetry of the hydrogen-bonding environment may explain that the ^{15}N signal of N22 is shifted relative to the response of N23. The peaks at 160.5 and 147.0 ppm are tentatively assigned to N22 and N23,

respectively. In analogy, the signal at 155.8 and 142.6 are respectively assigned to N22 and N23 in the Pfr state.

3.2.3 Pr → Pfr conversion in Cph1Δ2

The change in ^{13}C chemical shifts generated by the Pr → Pfr conversion are depicted in Figure 3.4A. After photoconversion mostly the rings ***C*** and ***D*** are affected, while smaller changes are observed also in rings ***A*** and ***B***. It is generally accepted that the first step of the Pr → Pfr conversion is the photoisomerization of the C15=C16 double bond. The change in chemical shift for the carbons at the C15 methine bridge and at N24 bring further evidence for a photoisomerization occurring at the C15=C16 double bond. In addition, the entire ring ***D*** shows considerable changes in its ^{13}C shifts, denoting a modification of its interaction with the protein surroundings. The Pr → Pfr transformation affects also slightly the two methine bridges between rings ***A***–***B*** and ***B***–***C***. At the ***B***–***C*** methine bridge, the resonances of C9 and C11 are equally downshifted by 3.3 ppm. The significant downshift at the C3^1 position by 2.4 ppm suggests a modification of the chromophore–protein linkage. The C12^3 carbon atom exhibits a significant 4.3 ppm upfield shift after photoconversion pointing to a change of the environment of the carboxylic moiety. According to the crystal structures this carboxyl group of the propionic side-chain of ring ***C*** interacts *via* two water molecules with the conserved His-290, which in turn interacts with ring ***D*** [51–53]. On the other hand, there are no indications for changes at the propionic side-chain of ring ***B***, which forms a salt-bridge *via* two hydrogen-bonds to the conserved Arg-254 in the Pr state [53]. Apparently, this interaction remains unaffected in the Pfr state.

3.2.4 Pr → Pfr conversion in the plant phytochrome *phyA*

The 1D ^{13}C CP/MAS NMR spectra of u-[^{13}C,^{15}N]-PCB-Cph1Δ2 in the Pr (black) and Pfr (grey) states are shown in Figure 3.5A. The Pr-Pfr difference spectrum (Fig. 3.5B) reveals the changes of chemical shifts generated by the Pr → Pfr photoconversion. Positive signals represent the Pr state and the negative signals arise from the Pfr state. In comparison, Figures 3.5C and 3.5D show the corresponding spectra for the plant-derived phytochrome u-[^{13}C,^{15}N]-PCB-*phyA*65. The Pr (black) and Pfr (grey) states are displayed in

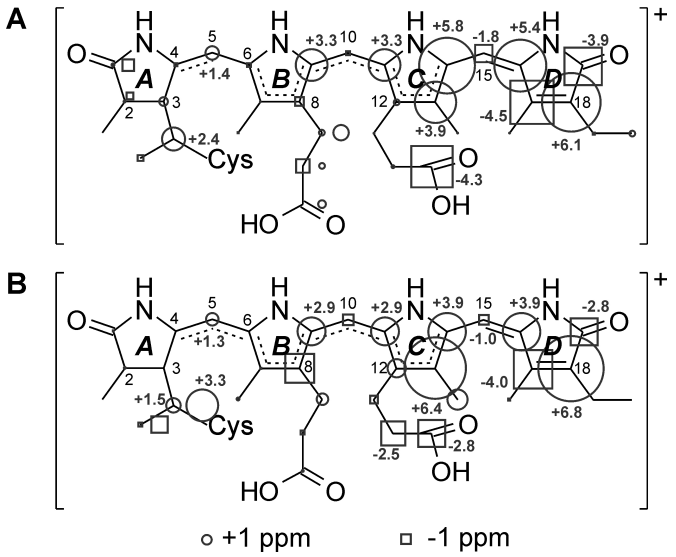


Figure 3.4: Changes in ^{13}C chemical shifts of the u-[^{13}C,^{15}N]-PCB chromophore in Cph1Δ2 (**A**) and *phy*A65 (**B**). The Pr state is taken as reference and the size of the circles and squares refers to the difference in ^{13}C chemical shift in the Pfr state. The carbons showing two resonances are labeled with two symbols. The positive charge due to the protonation of the ring ***B*** nitrogen is thought to be delocalized mainly over rings ***B*** and ***C***, and the non planarity of the C14–C15 single bond breaks the the conjugation with ring ***D***.

Figure 3.5C and the Pr-Pfr difference spectrum is presented in Figure 3.5D. The two difference spectra (Fig. 3.5B and D) show similarities, in particular in the methine and aromatic carbons regions. A small but clearly detectable difference however is noted in the spectral region around 125 ppm. The 1D ^{15}N CP/MAS NMR spectra of the u-[^{13}C,^{15}N]-PCB-Cph1Δ2 in the Pr and Pfr states are presented in Figure B.4. The similarity of the ^{13}C and ^{15}N spectra of Cph1Δ2 and *phy*A65 suggests that the chromophore geometry and the immediate protein environment are comparable in both species.

The 2D ^{13}C-^{13}C DARR NMR spectra of the Pr state and of the Pfr/Pr mixture (ratio ∼ 1:1) of *phy*A65 (Fig. B.5) lead to the ^{13}C assignments in both Pr and Pfr states (Table 3.1). The change in chemical shift accompanying the Pr → Pfr conversion is shown in Figure 3.4B. Also, the comparison of Figures 3.4A and B demonstrates that the phototransformation affects the chromophore in Cph1Δ2 and *phy*A65 in a similar manner. In *phy*A65, however, the C13 and C13^1 signals shift more than for Cph1Δ2. This explains the

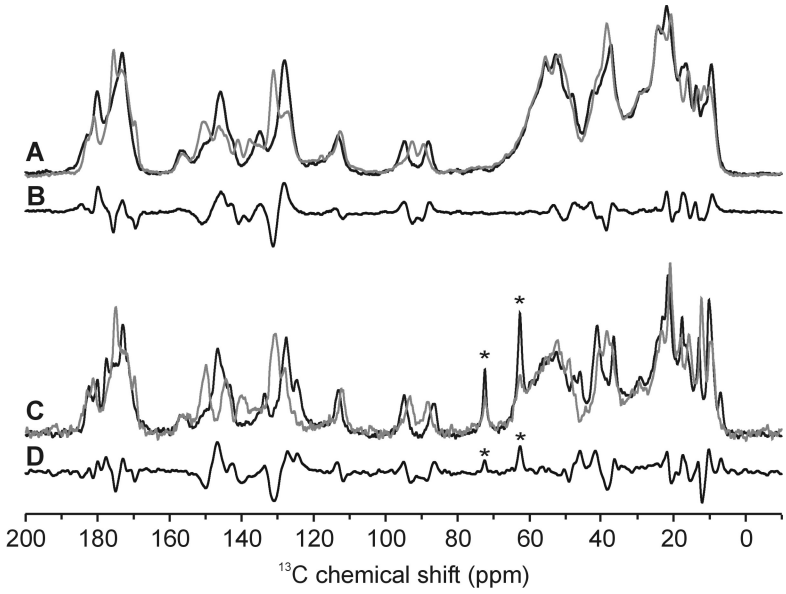


Figure 3.5: 1D ^{13}C CP/MAS NMR spectra of u-[^{13}C,^{15}N]-PCB in Cph1Δ2 and *phyA*65 in the Pr (**A** and **C**, black, respectively) and Pfr (**A** and **C**, grey, respectively) states. The Pr-Pfr difference spectra in Cph1Δ2 and *phyA*65 are shown in **B** and **D**, respectively. Positive signals refer to Pr and negative signals to Pfr. The asterisks indicate the position of glycol signals in natural abundance.

difference observed at 123 ppm between the difference spectra 3.4B and D.

As shown by vibrational techniques, the conformations of the bilin chromophore in the Pr and Pfr states in native plant phytochrome (*phyA*124) resemble those in the photosensory modules *phyA*65 of oat phytochrome [39,41] and Cph1 of *Synechocystis* [106]. The NMR data presented in this chapter provide additional clear evidence that the chromophore and its interactions with the protein are conserved in both states, possibly across the entire Cph1/plant phytochrome family. In view of these similarities, the observations for the whole Cph1 and plant phytochrome will be discussed in a common framework.

3.3 Discussion

3.3.1 Chromophore photoconversion

As shown in Figures 3.4A and B, the photoconversion of PCB mostly affects rings ***C*** and ***D***. This is in line with a photoisomerization occurring along the C15=C16 double bond. During this process the chromophore is involved throughout its entire structure, hence, the photoisomerization is not a local event but modifies the entire chromophore/protein interaction. A significant effect is also seen at the C10 methine carbon that is situated between the almost coplanar rings ***B*** and ***C***. In contrast, the shifts around methine carbon C5 that links rings ***A*** and ***B*** are small. The observed pattern can be rationalized by the assumption of five effects: (*i*) The chromophore is tensely fixed in the Pfr state, (*ii*) the conjugation increases in the Pfr state, (*iii*) the hydrogen-bonding interaction of the ring ***D*** carbonyl increases in the Pfr state, (*iv*) a local change of the electronic structure around ring ***C*** is identified, and (*v*) a significant change of the protein interacting with the ring ***C*** carboxylic group takes place.

(*i*) A loss of conformational heterogeneity at the ring ***B*** propionic side-chain implies an improved fit of the chromophore in the protein. Several cross-peaks at rings ***A*** and ***B*** become sharper in the Pfr spectrum, *e.g.*, carbons C4 and C6. The signal doubling observed for carbons C1 and C2 in the Pr state disappears in the Pfr state. These observations suggest that an induced fit mechanism balances an increase of mechanical tension occurring in the Pfr state, as is also observed by ^{15}N MAS NMR [104] and vibrational spectroscopy [43]. Such tension would also explain the shift observed at C3^1 that covalently links the chromophore *via* a thioether linkage to Cys-259.

(*ii*) The entire conjugation pattern undergoes a significant modification. In Figure 3.4 on the left side of ring ***C***, even numbered carbons are marked for a downfield shift (circle), while odd numbered carbons are up-shifted (square). On the right side of ring ***C***, however, the opposite pattern appears. Such pattern change, involving the entire conjugated chain implies a change in bond order. Assuming enhanced tension in the Pfr state, it can be proposed that an increase of bond-order for single bonds, increasing their rotational energy and providing the required stiffness, takes place concomitantly with a decrease in bond order for the double bonds.

(*iii*) There is a clear upshift at the carbonyl of ring ***D*** associated with

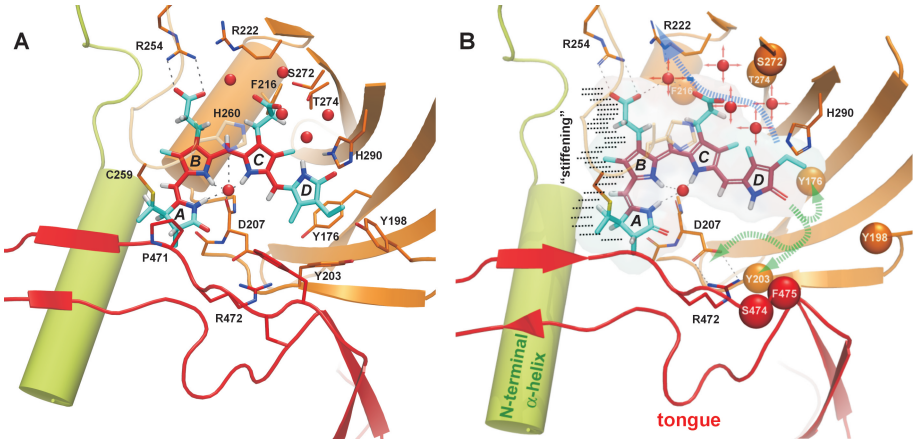


Figure 3.6: The PCB binding site of Cph1Δ2. Structural view on the protein environment of the PCB chromophore in the Pr state [53] highlighting the hydrogen-bonding network (**A**). Overview of putative structural changes caused by Pfr state formation (**B**). The dashed arrows indicate potential paths of signal transmission within the chromophore binding site. The observed loss of conformational freedom along rings ***A*** and ***B*** is highlighted by dotted lines. This figure was made by PyMol [107].

decreased electron density at carbons C17 and C19. A clear change of this group has also been shown by FTIR spectroscopy [39, 40]. In the Pr state of Cph1 (Fig. 3.6A) a weak hydrogen-bond is formed between the ring ***D*** carbonyl and His-290 due to its energetically unfavorable angle of 102° (O-Hε-Nε) caused by the low tilt of ring ***D*** *vs.* ring ***C*** (26.3°). An increase of hydrogen-bonding interactions can take place for the ring ***D*** carbonyl during Pfr state formation. Such an increased polarization at the terminal group may cause an increasing conjugation throughout the entire chain of the chromophore and hence the red-shift of Pfr absorption. It is reasonable to assume that a strong hydrogen-bonding involving the carbonyl of ring ***D*** stabilizes the chromophore in the Pfr state.

(*iv*) While the chemical shifts of carbons in rings ***B*** and ***C*** are almost mirror symmetrical around C10 in the Pr state, this symmetry is partially broken in the Pfr state. While in the other rings an alternating pattern along the conjugated chain occurs, solely in ring ***C*** all carbons are downshifted in the Pfr state. This is indicative of an increase of electron density in the Pfr state at this ring. The perturbation of the alternating pattern at ring ***C*** suggests that the origin of the change of the conjugation pattern is localized

here. It is possible that in the Pr state the conjugation is interrupted at or around ring ***C*** due to the interplanar tilt between rings ***C*** and ***D***, and that the observed alternating pattern is caused by the extension of the conjugated system beyond ring ***C***. Such an effect could also explain the red-shift of the absorption spectrum upon generating the Pfr state. In any case, ring ***C*** appears to be the hotspot for the change of the electronic structure.

(*v*) At the propionic side-chain of ring ***C***, a significant up-shift of the ^{13}C resonance at the carboxylic group occurs. It can be assumed that this group faces strongly altered interactions with the protein environment. This change may correspond to a modification previously observed by FTIR spectroscopy [39,40] which has been interpreted as an alteration of either a protein amide or carboxyl group. In contrast to the ring ***B*** propionic side-chain, the ring ***C*** propionic group is well hydrated within a cluster of five water molecules and makes only an indirect interaction with the Arg-222 *via* a water molecule (Fig. 3.6A). Interestingly, a structural comparison between Cph1 and the BphPs shows that Arg-222 may either adopt an outward-oriented conformation towards the GAF-PAS interface or point into the core region of the GAF domain itself.

Hence, from this analysis, the following picture of the Pr → Pfr phototransformation emerges: The chromophore forms a strong hydrogen-bond *via* its ring ***D*** carbonyl, increasing both the strength and length of the conjugation network and stabilizing the chromophore in a tensed shape (Fig. 3.6B). The rings ***A*** and ***B*** are tightly packed in the protein pocket. The observed changes in ^{15}N chemical shifts in the rings ***C*** and ***D*** may be explained by such tension linked to traction at this side of the chromophore, leading to a banana-shaped cofactor in the Pfr state. In addition, it is also possible that the changes in ^{13}C and ^{15}N chemical shifts are linked to a redistribution of the positive charge along the chromophore during the conversion from Pr to Pfr to mediate the bond order alteration and promote an induced fit in the Pfr state.

3.3.2 Charge localization in phytochrome

As shown by the MAS NMR study of the free PCB in **Chapter 2**, solely the nitrogen of ring ***B*** is unprotonated. Therefore, the ring ***B*** is a pyrrolenine ring with a "pyridine" kind of nitrogen and ring ***C*** is a pyrrole ring. The nitrogen atom of the pyrrole ring is protonated, the hydrogen being in plane

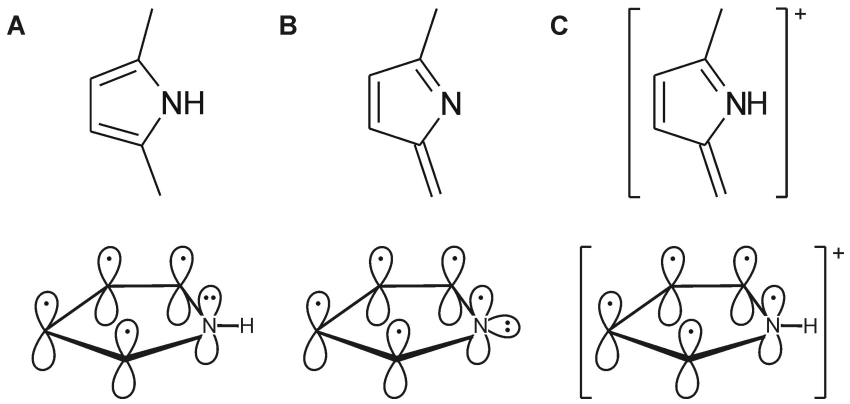


Figure 3.7: Structure of pyrrole (**A**), pyrrolenine (**B**) and protonated pyrrolenine rings (**C**).

with the ring and, according to the Hückel rule, the two π-electrons of the lone pair of the nitrogen atom are delocalized in the aromatic ring (Fig. 3.7A). The two π-electrons of the lone pair can be considered as a conjugation defect in the sense of polymer physics [108]. In the case of the pyrrolenine ring, the nitrogen is conjugated with the π-system (Fig. 3.7B). The assembly of PCB in the protein pocket leads to the protonation of the nitrogen of the pyrrolenine ring. The protonated pyrrolenine ring is positively charged and the nitrogen is conjugated with the π-system (Fig. 3.7C).

Due to the conjugation of the π-system in open-chain tetrapyrrole, the positive charge can be potentially delocalized over the four the nitrogen atoms/rings (Fig. 3.8). The crystal structures of phytochromes do not show the presence of a strong counterion in the vicinity of the chromophore, therefore the positively charged chromophore appears to be in an unstable state. In the Pr state, the two inner rings have very similar ^{13}C chemical shifts, suggesting a symmetric electronic structure of the conjugated π-system in the rings ***B*** and ***C***. This suggests that the positive charge is mainly spread over the two inner rings ***B*** and ***C*** and that the mesomeric forms **II** and **III** are prevailing in the Pr state (Fig. 3.8). In addition, studies of model compounds of phytochrome have shown that the an appreciable positive charge resides on the central atom C10 [109].

The conversion to the Pfr state is accompanied by a general downshift of the ^{13}C resonances at the ring ***C***. This indicates a modification of the electro-

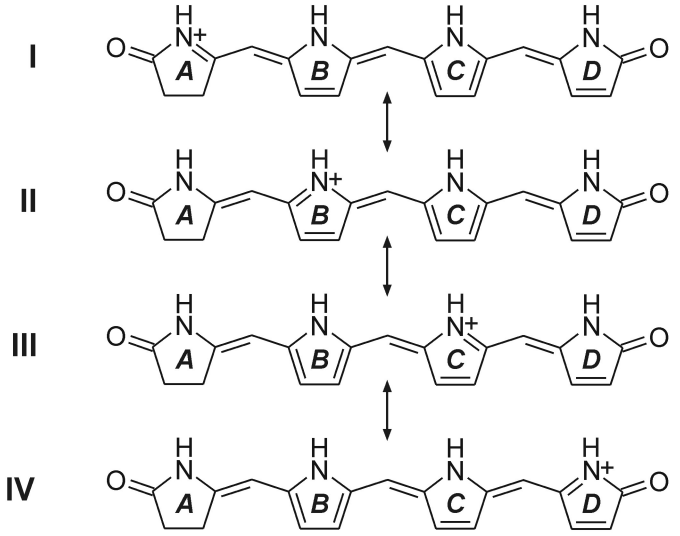


Figure 3.8: Resonance structures of protonated PCB chromophore in phytochrome. The positively charged nitrogen is conjugated and the others are representing conjugation defects in the conjugated system.

nic structure along this ring, which may be associated with a redistribution of the positive charge along the chromophore. Indeed an extended delocalization of the positive charge over the ***B*** and ***C*** rings as well as the ***D*** ring, *i.e.* Figure 3.8 forms **II**, **III** and **IV**, may contribute to increase the stability of the chromophore in the Pfr state. By switching with light, the protein can conveniently balance the charge in such a system and mediate an induced fit by the charge polarization of the chromophore and the polar protein surroundings in the Pfr state.

3.3.3 Signal transduction pathway

The question arises at which positions the chromophore dynamics is coupled to the protein environment to allow signal transduction to the protein surface. Important information can be extracted from Figures 3.4A and B. The changes occurring on the left side of ring ***C*** can be explained by a change of conjugation. On the other hand, on the right side of ring ***C*** multiple effects are overlaying and two of them are clearly due to changed chromophore-protein interaction. There are significant changes localized at the carboxylic

group of the propionic side-chain of ring ***C*** as well as at the carbonyl group of ring ***D***. The X-ray structures of Cph1 and the DrBphP bacteriophytochromes show that His-290 (His-372 in *phyA*65 and His-299 in DrBphP) is bridged *via* two conserved water molecules to the carboxyl group of ring ***C*** and forms a hydrogen-bond to the carbonyl of ring ***D*** [18, 52, 53] (Fig. 3.6). Hence, it can be suggested that this highly conserved His-290 couples the photochemistry of the chromophore to the protein.

Since the ^{13}C signal of the ring ***A*** carbonyl and the ^{15}N signal of the ring ***A*** nitrogen exhibit only minor changes during the Pr → Pfr photoconversion, only local conformational changes of the protein matrix surroundings are likely to occur. On the other hand, changes of the hydrogen-bonding network by ring ***D*** photoisomerisation could alter the conserved salt bridge between Asp-207 and Arg-472 and thus transmit the signal to the protein surface, *e.g.*, by rearrangement of the tongue region (Fig. 3.6B). As possible conserved partners for strong hydrogen-bonding to the ring ***D*** carbonyl in the Pfr state nearby located hydrogen-bonding donors such as Asp-207, Tyr-198, Tyr-203, Tyr-263 and Ser-474 may be considered. Based on the crystal structure of PaBphP in its Pfr-like ground state [55], Tyr-263 may indeed be hydrogen-bonded to the C19 carbonyl (see also **Chapter 4**).

3.4 Materials and Methods

3.4.1 Sample preparation for MAS NMR spectroscopy

The u-[^{13}C,^{15}N]-PCB was prepared following published methods [94]. Preparation of Cph1Δ2 and *phyA*65 apo- and holoproteins were performed as described [21, 110]. For the measurements of the Pr state, samples were irradiated with light filtered through a far-red cut-off filter ($\lambda_{max} \sim 730$ nm). Pfr/Pr mixtures were produced by saturating irradiation at 660 nm. Cph1Δ2 phytochrome in its pure Pfr state was obtained by size-exclusion chromatography using Superdex 200 (Pharmacia/GE-Healthcare, USA) [111].

3.4.2 MAS NMR spectroscopy

1D ^{13}C CP/MAS spectra were recorded using a DMX-400 spectrometer, equipped with 4-mm CP/MAS probe. All data were recorded at 243K with a spinning frequency of 10 kHz. The proton $\pi/2$ pulse was set to 3.6 μs. The

^{1}H power was ramped 80-100% during CP. During the data acquisition, the protons were decoupled from the carbons by use of the TPPM decoupling scheme [65]. For u-[^{13}C,^{15}N]-PCB-Cph1Δ2 measurements in the Pr and Pfr states, approximately 15 mg of protein were placed in a 4-mm zirconia rotor. About 12 mg of u-[^{13}C,^{15}N]-PCB-*phyA*65 was used for the measurements of the Pr state and Pfr/Pr (1:1) mixture.

All 2D ^{13}C-^{13}C DARR experiments were performed in a field of 17.6 T with an Avance-WB750 spectrometer, equipped with a 4-mm triple resonance CP/MAS probe (Bruker, Karlsruhe, Germany). ^{1}H π/2- and ^{13}C π-pulse lengths were set at 3.1 μs and 5 μs, respectively. The ^{1}H power was ramped 80-100% during CP. Spin diffusion periods of 5 and 50 ms were applied. ^{1}H CW decoupling was about 80 kHz during the proton mixing and about 43 kHz for TPPM decoupling during acquisition. The 2D ^{13}C-^{13}C spectra of Cph1Δ2 were recorded with 1536 scans, and with 8 ms evolution in the indirect dimension, leading to experimental times of 80 hours. The spectra of the *phyA*65 protein were recorded with 2048 scans in 2.5 days. The data were processed with the Topspin software version 2.0 (Bruker, Karlsruhe, Germany) and subsequently analyzed using the program Sparky version 3.100 (T. D. Goddard & D. G. Kneller, University of California, San Francisco, USA).

1D ^{15}N CP/MAS spectra were recorded using an AV-750 spectrometer, equipped with 4-mm CP/MAS probe. The proton π/2- pulse was set to 3.1 μs, temperature was 243 K and the spinning frequency 8 kHz. ^{1}H-^{13}C heteronuclear experiments were performed at a DMX-400 spectrometer (Bruker, Karlsruhe, Germany) using a frequency switched Lee-Goldburg pulse sequence [68].

Chapter 4

The Pfr → Pr photoconversion process

4.1 Introduction

The parent states of phytochrome, Pr and Pfr, have been studied in **Chapter 3**. It has been shown that the forward Pr → Pfr phototransformation is characterized by the formation of a strong hydrogen-bonding interaction on the ring ***D*** carbonyl and an increase in length and strength of the conjugation of the π-system.

At both Pr → Pfr and Pfr → Pr phototransformations, intermediate states can be distinguished [39, 43, 96]. Their structural characterization may allow for detailed insight into the mechanism of the phototriggered processes. The photochromic photocycle of various phytochromes (Fig. 1.5) has been studied by absorption and vibrational spectroscopy. For the Pr → Pfr conversion, absorption spectroscopy has identified up to three intermediates, called Lumi-R, Meta-R_a, and Meta-R_c [112–114]. For the Pfr → Pr back-reaction, two intermediates (Lumi-F and Meta-F) have been observed [113], for a recent overview on the time-resolved spectroscopy of phytochrome see [115]. These intermediates have been studied by infrared and Raman spectroscopy on various organisms [27, 30, 39, 40, 42, 43, 89, 116]. These studies suggest that Lumi-R and Meta-R are structurally different from each other as well as from Pr and Pfr, however, early studies propose that the absorption maxima of Lumi-R and Lumi-F are similar to Pr (673 and 660 nm, respectively) [113]. It should

be noted that most conversion studies have been performed in a temperature-regulated manner, allowing to trap the first intermediate at very low temperature and generating stepwise the following intermediates by gentle increase of the temperature. Thus, the given absorption maxima can deviate from such obtained at ambient temperatures by time-resolved spectroscopy.

On the other hand, much less is known about the back-reaction, which is believed to occur essentially in a single step, directly after the photoexcitation, followed by only minor relaxation steps re-arranging the cofactor-protein interactions [43, 106]. In any case, forward- and back-reactions are very different processes and not simply mirror-symmetric transformations. The intermediates of the back-reaction, Lumi-F and Meta-F, have been shown in the CphA phytochrome from the cyanobacterium *Calothrix* sp. PCC 7601 to absorb at 635 and 640 nm, respectively [116]. The strong blue-shift in the initial phototransformation step is not fully understood. In addition, the specific characteristics of the Lumi-F and Meta-F intermediates have not yet been described.

In **Chapter 3**, the two parent states of the phytochrome system Pr and Pfr have been studied by ^{1}H , ^{13}C and ^{15}N CP/MAS NMR. In this chapter, the intermediates of the back-reaction of phytochrome Cph1, Lumi-F and Meta-F, are investigated by ^{1}H, ^{13}C and ^{15}N CP/MAS NMR. Uniformly ^{13}C and ^{15}N as well as selectively ^{15}N labeled samples are used for signal assignment. The intermediates were trapped directly in the magnet with illumination at low temperature. Light-triggered low-temperature MAS NMR investigations of intermediates have recently also been presented on rhodopsin [117], bacteriorhodopsin [118] and adenylyl transfer reaction of T4 DNA ligase [119].

4.2 Results

4.2.1 Conformational changes of the cofactor carbon atoms

The 2D ^{13}C-^{13}C MAS DARR spectra of the Lumi-F and Meta-F intermediates are show in Figures 4.1 and 4.2, respectively. From these data, almost complete sets of ^{13}C assignments have been obtained for both intermediate states (Table 4.1). In the 2D spectra of both Lumi-F and Meta-F, the resonances of the aromatic carbons have been assigned through their correlation with the methyl, ethyl or propionic substituents. The carbon atoms C9 and

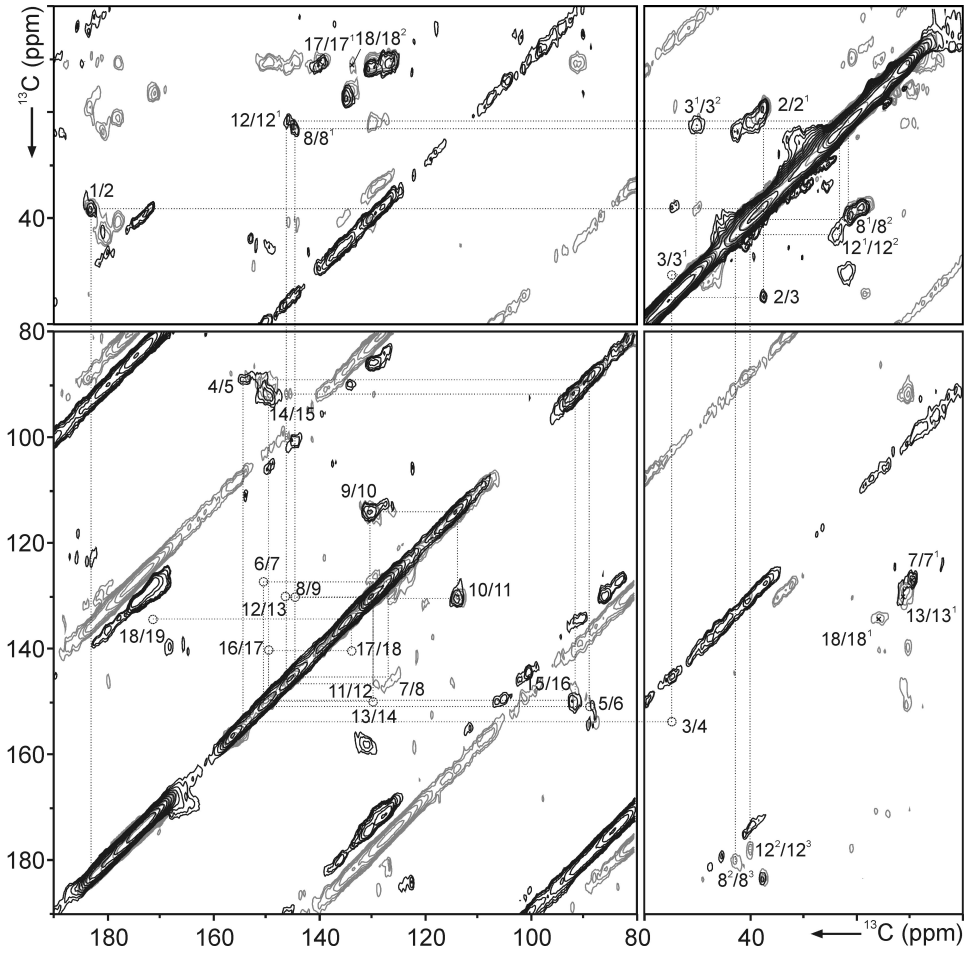


Figure 4.1: Contour plot of the 2D ^{13}C-^{13}C DARR NMR spectra of u-[^{13}C,^{15}N]-PCB-Cph1Δ2 in the Lumi-F state using proton mixing times of 5 and 50 ms (black and grey, respectively). Spectra recorded at 173 K and spinning frequencies of 9 and 10 kHz.

C11 as well as C14 and C16 overlap in both intermediate states (Table 4.1).

The changes of chemical shifts during the three transitions of the back-reaction (Pfr → Lumi-F, Lumi-F → Meta-F, Meta-F → Pr) for selected carbons is shown in Figure 4.3. The general features are: (*i*) The major changes occur at the carbons between C13 and C19, and (*ii*) the transformations during the two first transitions are significantly larger than during the third transition. The large chemical shift changes during the second transition are

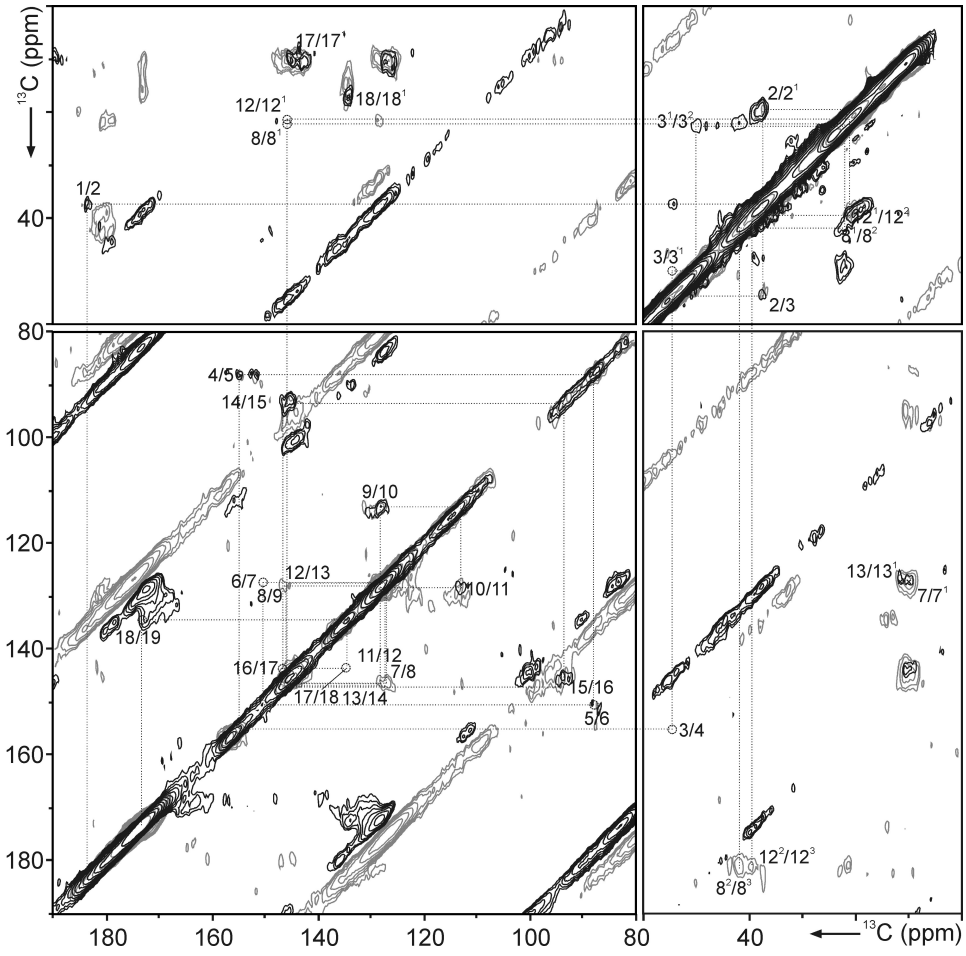


Figure 4.2: Contour plot of the 2D ^{13}C-^{13}C DARR NMR spectra of u-[^{13}C,^{15}N]-PCB-Cph1Δ2 in the Meta-F state using proton mixing times of 5 and 50 ms (black and grey, respectively). Spectra recorded at 203 K and spinning frequencies of 9 and 10 kHz.

unexpected. Hence, the transition from Lumi-F to Meta-F appears to be more than a simple relaxation process. Spatial details can be better recognized in Figure 4.4. At the C19 carbonyl group, the changes occur during the first two transitions to roughly the same extent. In **Chapter 3**, it has been concluded that the Pfr state is characterized by hydrogen-bonding interactions stronger than in Pr. It appears that the weakening of these interactions occurs in two steps. During the first transition, a significant change occurs selectively at

Position	Pfr	Lumi-F	Meta-F	Pr
C1	182.8	183.2	183.6	182.5
$C1^a$	—	—	—	184.0
C2	37.2	37.3	37.1	37.1
$C2^a$	—	—	—	38.1
$C2^1$	18.5	18.6	18.6	17.5
C3	54.3	54.3	54.0	53.4
$C3^1$	50.0	50.0	49.2	47.6
$C3^2$	21.6	21.9	22.0	21.8
C4	154.0	n.d.	154.0	153.9
C5	88.5	88.5	87.5	87.1
C6	148.8	n.d.	n.d.	149.1
C7	126.1	126.7	126.1	126.1
$C7^1$	9.3	9.5	9.3	9.2
C8	143.6	144.6	145.5	144.5
$C8^1$	23.1	23.4	22.0	22.5
$C8^{1a}$	—	—	—	21.5
$C8^2$	41.7	42.6	42.8	43.1
$C8^{2a}$	—	—	—	41.1
$C8^3$	180.5	180.8	180.6	180.5
$C8^{3a}$	—	—	—	179.7
C9	131.0	130.1	128.1	127.7
C10	112.3	113.8	112.9	112.7
C11	131.0	130.1	128.1	127.7
C12	145.8	145.7	145.5	145.5
$C12^1$	20.6	21.0	21.0	21.1
$C12^2$	38.3	40.0	38.3	37.5
$C12^3$	175.2	178.2	179.1	179.5
C13	130.6	129.9	126.2	126.3
$C13^1$	11.9	11.8	11.5	11.7
C14	151.5	149.5	145.4	145.7
C15	91.7	91.9	93.2	93.5
C16	151.1	149.5	145.4	145.7
C17	137.7	139.8	143.2	142.2
$C17^1$	10.1	10.1	10.2	9.8
C18	140.4	134.4	134.2	134.3
$C18^1$	15.6	15.6	16.1	16.1
$C18^2$	13.3	n.d.	n.d.	13.3
C19	168.4	171.8	172.7	172.8

Table 4.1: ^{13}C chemical shifts obtained for Cph1Δ2 containing an u-[^{13}C,^{15}N]-PCB chromophore.

position C18, and also a change of the chemical shift of the $C12^3$ carboxylic group of ring ***C*** occurs already during this first transformation. C18 shows no further changes, whereas during the second transition, in addition to a large C13 change, both ring carbon neighbors of the C10 and C15 bridges are affected. It appears that the dark single bond transformation following the

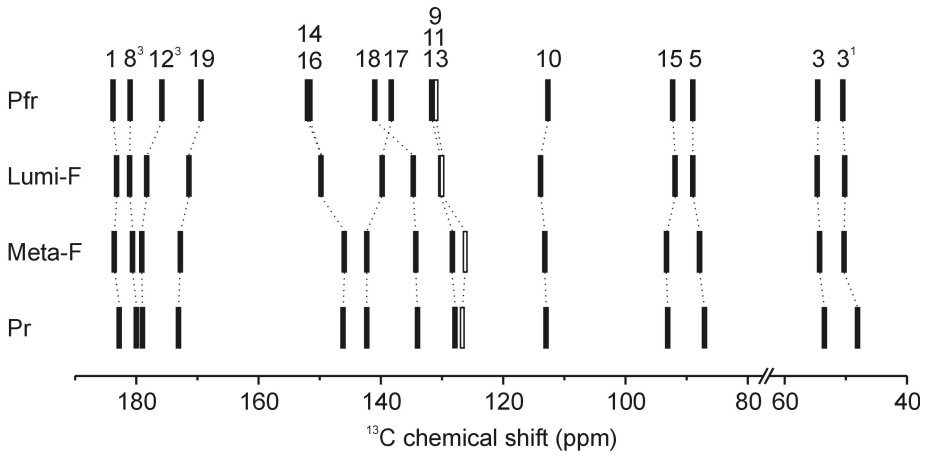


Figure 4.3: ^{13}C chemical shifts for selected carbon atoms during the Pfr → Pr back-reaction. For seek of clarity, the ^{13}C resonance of C13 is indicated by an open rectangle.

light-induced double bond isomerization affects the electronic structure even stronger. The unit formed by rings ***A*** and ***B*** shows less extensive effects, those that are seen affecting the C3^1 thioether linkage to Cys-259. In fact, perhaps the biggest surprise is that only very weak shifts were found to be associated with C15. Also interesting is that the ring ***B*** propionic carbons show only minimal changes.

4.2.2 Assignment of the nitrogen atoms

The 1D ^{15}N spectra of ^{15}N21-PCB-Cph1Δ2 labeled phytochrome in the Pr, Pfr, and the intermediate states are presented in Figure 4.5, Column A. The N21 nitrogen atom exhibits a ^{15}N chemical shift at around 158 ppm and appears to be only weakly affected during the Pfr to Pr back-reaction. This is in line with the weak changes along ring ***A*** during the Pfr → Pr conversion deduced from the ^{13}C chemical shifts. The equivalent ^{15}N CP/MAS spectra of the u-^{15}N-PCB-Cph1Δ2 are shown in Figure 4.5, Column B. The deconvolutions of the Lumi-F and Meta-F spectra using Voigt functions are shown in Appendix C, Figure C.1. In the Lumi-F states, two ^{15}N resonances overlap at 157.9 ppm and two other signals are observed at 146.0 and 136.5 ppm. The Meta-F intermediate presents four peaks at 161.1, 156.0, 144.8 and 127.1 ppm.

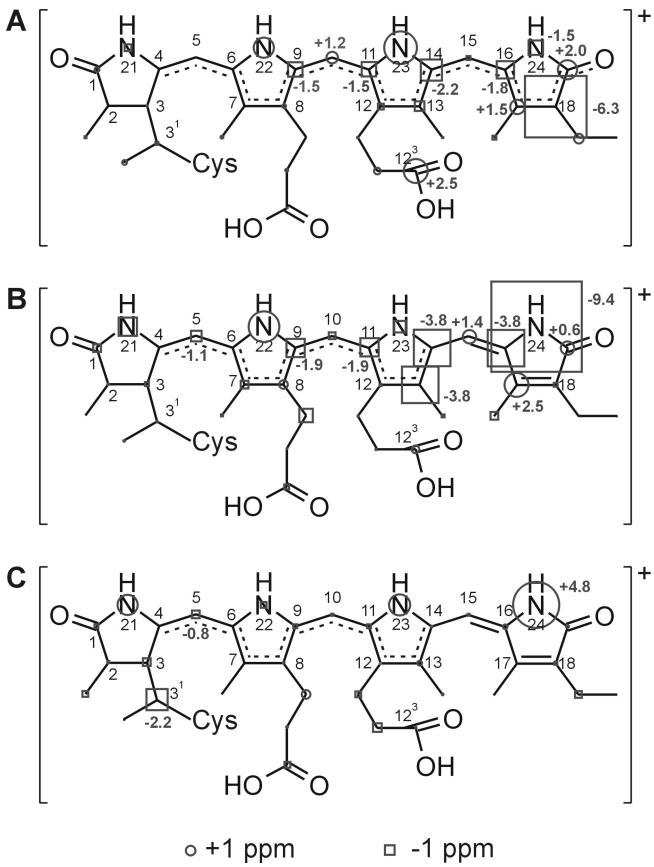


Figure 4.4: Change in ^{13}C and ^{15}N chemical shift of the u-[^{13}C,^{15}N]-PCB chromophore in Cph1Δ2 during the Pfr → Lumi-F (**A**), Lumi-F → Meta-F (**B**) and Meta-F → Pr (**C**) transitions. For each transition, the starting state is taken as reference and the size of the circles and squares refers to the difference in ^{13}C and ^{15}N chemical shifts in the next state.

One of the overlapping peaks at 157.9 ppm in the Lumi-F state is attributed to N21. The signal at 156.0 ppm in the Meta-F state is tentatively assigned to the ring ***A*** nitrogen (Table 4.2). It has been proposed in **Chapter 3** that the ring ***D*** nitrogen resonance occurs at 131.9 and 138.0 ppm in the Pr and Pfr state. In analogy, it can be assumed that the signals at 136.5 and 127.1 ppm arise from N24 in the Lumi-F and Meta-F intermediates, respectively. Similarly, the signals at 146.0 and 144.8 are tentatively assigned to N23 in Lumi-F and Meta-F, respectively. Finally, the two remaining signals at 157.9 and 161.1 ppm in Lumi-F and Meta-F originate from N22.

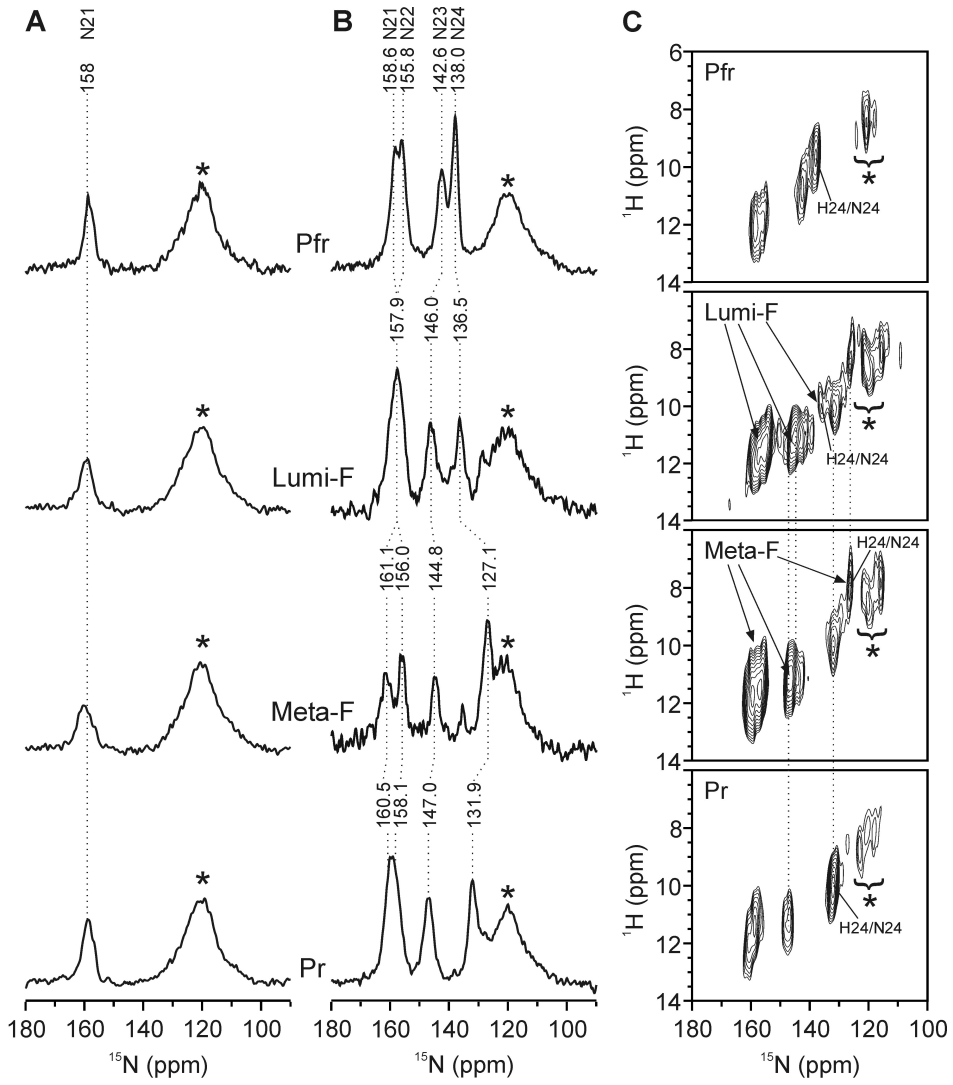


Figure 4.5: 1D ^{15}N spectra of ^{15}N21-PCB-Cph1Δ2 (column **A**) and u-^{15}N-PCB-Cph1Δ2 (column **B**) in the Pfr, Lumi-F, Meta-F and Pr states recorded at 17.6 T with a spinning frequency of 8 kHz and at 243 K, 173 K, 203 K, and 243 K, respectively. 2D ^{1}H-^{15}N FSLG heteronuclear correlation spectra of Pfr, Lumi-F, Meta-F, and Pr (Column **C**). The spectra of the intermediates were obtained from a Pfr:Pr (1:1) mixture.

4.2.3 Changes of the nitrogen atoms

The Pfr → Lumi-F transition causes a shift of the N22 and N23 responses by +2.1 and -3.4 ppm, respectively (Fig. 4.4), while changes of the other ni-

Position	Pfr	Lumi-F	Meta-F	Pr
N21	158.6	157.9	156.0	158.1
N22	155.8	157.9	161.1	160.5
N23	142.6	146.0	144.8	147.0
N24	138.0	136.5	127.1	131.9

Table 4.2: Tentative ^{15}N chemical shift assignment of u-[^{13}C,^{15}N]-PCB chromophore in Cph1Δ2 during the Pfr → Pr conversion.

trogen atoms are smaller (-0.7 and -1.5 ppm for N21 and N24, respectively). Also the proton chemical shifts (Fig. 4.5, column C) do not undergo any significant change during this step. The Lumi-F → Meta-F transition shows a strong change at N24, which shifts 9.4 ppm downfield. Interestingly, this change is linked to an upfield shift of the H24 pyrrole proton from ∼10 to ∼8 ppm (Fig. 4.5, column C), suggesting a modification of hydrogen-bonding in the Meta-F intermediate state. In addition, also the signal assigned to the ring ***B*** nitrogen shifts from 157.9 to 161.1 ppm, however, no significant proton shift can be observed. The Meta-F → Pr transition is also associated with significant chemical shift changes of the ring ***D*** nitrogen and the pyrrole proton, indicating that the a hydrogen-bonding interaction is restored at this position. The nitrogen atom N21 and N23 are also affected during this transition (+2.1 and +2.2 ppm, respectively).

4.3 Discussion

4.3.1 The Pfr → Lumi-F transition

It has been proposed that the chromophore in the Pfr state is in a conformationally strained state [43, 104, 120], requiring a strong fixation of the ring ***D*** in the pocket. To this end, a strong hydrogen-bond of the ring ***D*** carbonyl has been proposed, leading to enhanced conjugation from ring ***A*** to ring ***D*** that increases the stiffness of the cofactor [14, 120]. On the other hand, the significant chemical shift change at C18 is specifically associated with the Pfr to lumi-F primary photoreaction. This might result from a mechanical interaction of the C18 ethyl group associated with the strained cofactor state. Indeed, the thermal stability of oat phytochrome A in the Pfr state is improved when the size of the C18 sidechain group is increased [121]. In a recent X-ray structure on the Pfr-like state of *Pseudomonas aeruginosa* PaBphP [55], however, no residues close to the ethyl group are observed. Similarly, the Pr

structure of Cph1 [53] does not provide any clue to a possible interaction. This effect may be related to the changes on the electronic structure directly induced by the photoisomarization and the change of hydrogen-bonding interaction at the C19 carbonyl [120, 122]. Hence, it appears that the extended conjugation is already broken in the Lumi-F state, as demonstrated by its strongly blue-shifted absorption [116].

The ring ***D*** nitrogen is protonated and hydrogen-bonded in the Pfr state (Fig. 4.5, Column C). Since the changes in the ^{15}N shift of N24 as well as at the ^{1}H resonance of its bound proton are small, it can be assumed that the hydrogen-bonding interaction remains even after the photoisomerization, implying that the cofactor is not yet fully relaxed in the Lumi-F state. On the other hand, the hydrogen-bond at the C19 carbonyl weakens during the initial Pfr → Lumi-F transition. The fact that the hydrogen-bond of the ring ***D*** nitrogen remains almost unchanged in Lumi-F suggests that the hydrogen-bonding partner is very strong. From the crystal structure of Cph1Δ2 in the Pr state, the hydrogen-bonding partner has been shown to be a water molecule [53]. Comparing the ^{15}N chemical shifts of Pfr, Pr and the intermediate Meta-F, where this hydrogen-bond is broken, it is further concluded that the hydrogen-bonding partner in Pfr is stronger than water. It has been shown by mutational studies that Asp-207 is crucial for the formation of the Pfr state [19, 98]. As suggested by the X-ray structure of the Pfr-like state, the carboxylic group of the side-chain of Asp-207 could indeed be the strong hydrogen-bonding partner of N24 in the Pfr state.

The maintenance of the hydrogen-bond at N24 is difficult to reconcile with a full 180° rotation of ring ***D*** during the photoisomerization. Studying a phytochrome model compound in solution, Stanek and Grubmayr [103] have shown that the isomerization of the C15=C16 double bond affects strongly the ^{13}C chemical shift of the C15 carbon (7 ppm upshift upon E/Z isomerization). In solution, such an E/Z isomerization generates the flip of the ring ***D*** by about 180°. For the Pfr → Lumi-F transition, however, only a weak effect is observed at the C15, although it cannot be ruled out that other effects might mask the expected large change at this position. In any case, the first trapped photochemical event involves something different from a classical full 180° rotation of ring ***D*** associated with a complete E/Z isomerization as observed in solution.

Interestingly, the protein pocket around the C12^3 carboxylic group of the

ring ***C*** propionic side-chain appears to be already re-arranged in the Lumi-F intermediate. In particular the position of His-290 may be re-arranged into its Pr position and may already interact with the ring ***D*** carbonyl group.

4.3.2 The Lumi-F → Meta-F transition

The Pfr → Lumi-F transition is characterized by the photochemical *E*-to-*Z* C15=C16 double bond isomerization, while the Lumi-F → Meta-F transition is related to thermal processes. This transition is characterized by the full release of ring ***D*** from its tensed state as indicated by two significant changes: (*i*) the loss of hydrogen-bond interaction at the ring ***D*** nitrogen and (*ii*) a second stronger change of the C10 and C15 methine bridges. It appears that the chromophore is fully relaxed in Meta-F, while in Lumi-F the hydrogen bridge at the ring ***D*** nitrogen is still preventing a full rotation of the ring. It is surprising that during the Lumi-F → Meta-F transition the changes around methine bridges C10 and C15 are stronger than in the Pfr → Lumi-F transition.

4.3.3 The Meta-F → Pr transition

As the chromophore has already been relaxed in the Meta-F state, the changes along the conjugated system are very minor with respect to the ^{13}C chemical shift. Interestingly, the main effects occur at C3^1, the cofactor-matrix link, and at N24 which is re-bound *via* a hydrogen-bonding interaction to a water molecule as seen in the X-ray structure of the Pr state [53]. Additional minor changes indicate an overall re-arrangement of the chromophore-protein interactions, potentially involving – not observable – movements of the protein environment.

4.3.4 Model for the back-reaction

The ^{1}H, ^{15}N and ^{13}C CP/MAS NMR data indicate that the strained chromophore in Pfr is associated with four important effects (Fig. 4.5A): (*i*) The increased conjugation changing C–C single bonds to partially higher bond orders and double bonds to partially lower bond orders, (*ii*) the strong hydrogen-bond of the C19 carbonyl to Tyr-263, as shown in the crystal structure of PaBphP in its Pfr-like ground state, (*iii*) the strong hydrogen-bonding of

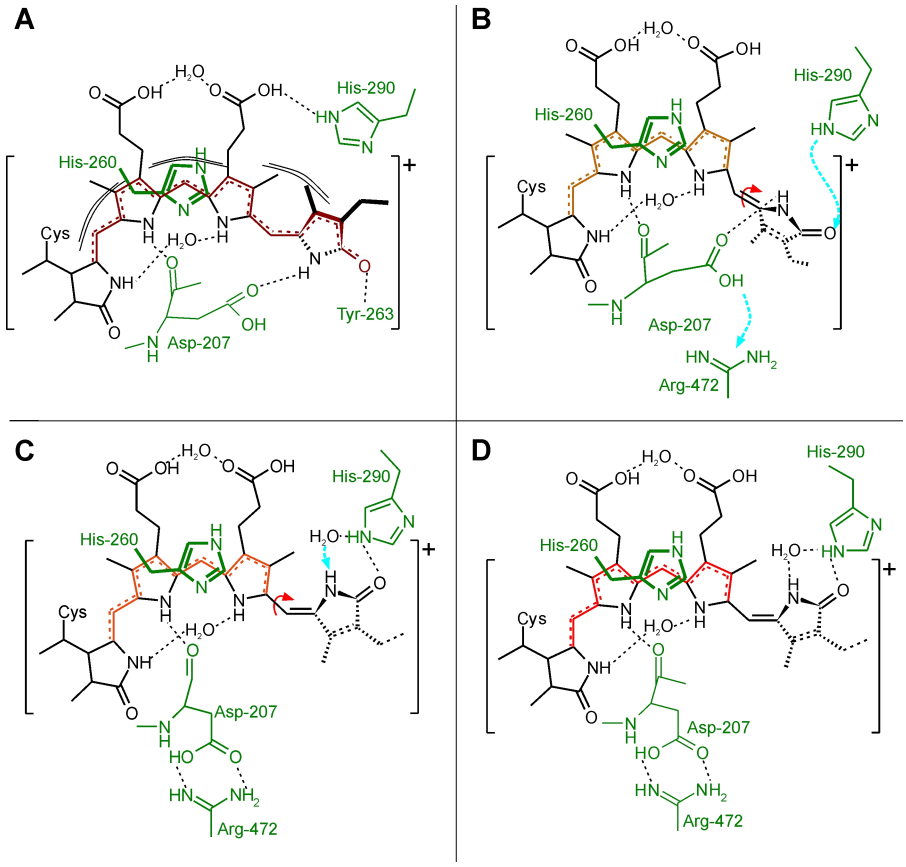


Figure 4.6: Proposed structures and conformational changes of the tetrapyrrole chromophore and its binding pocket in the Pfr (**A**), Lumi-F (**B**), Meta-F (**C**) and Pr (**D**) states. The conjugated system is shown in dark red (Pfr), orange-red (Lumi-F, Meta-F) and red (Pr). The rotations around the double and single bond of the C15 methine bridge are shown by solid arrows. The dashed arrows indicate potential paths of signal transmission within the chromophore binding pocket. Protein residues are indicated in green.

ring ***D*** nitrogen, presumably to Asp-207 and (*iv*) a potential mechanical blocking mechanism associated with the C18 ethyl group would be an obvious hypothesis, however the X-ray structural data do not reveal any interaction in this region. In addition, the X-ray structure of *Pseudomonas aeruginosa* PaBphP in the Pfr state shows that the His-290 homolog provides an anchor for the C12[3] carboxylic group of the chromophore.

The Lumi-F state (Fig. 4.5B) is characterized by (*i*) a shorter and weaker conjugation system, (*ii*) a partial relaxation of the cofactor due to incomplete rotation of the ring ***D*** caused by the release of the C19 carbonyl hydrogen-bonding interaction, as well as (*iii*) a matrix re-arrangement around the carboxylic group of the ring ***C*** propionic side-chain.

The Meta-F state (Fig. 4.5C) is described by (*i*) the full relaxation of the chromophore after breaking the hydrogen-bond of the ring ***D*** nitrogen to the carboxylic group of the side-chain of Asp-207 allowing to complete the rotation of the C15 single bond and (*ii*) the formation of a new hydrogen-bond between C19 carbonyl and His-290.

In the Pr state (Fig. 4.5D), in which the cofactor is fully relaxed and hydrogen-bonded, (*i*) a new hydrogen-bond at ring ***D*** nitrogen is formed by a water molecule, and (*ii*) protein relaxations have occurred.

The CP/MAS NMR data show that the back-reaction includes two intermediates which can be structurally clearly distinguished, and which adopt a conformation and electronic arrangement different than the two parent states Pr and Pfr.

4.3.5 Model for signal transduction

The data presented here describe the changes of the Cph1 chromophore from Pfr to the Pr ground state. Thus, the observed changes of the chromophore and the protein during the transition from Pfr to Lumi-F, followed by the Meta-F to Pr state reflect changes that are connected to both photoconversion and signal transduction.

The data shown in this chapter reveal that the Pfr → Pr photoconversion is associated with changes to the $C12^3$ carboxylic group of ring ***C*** and the entire ring ***D*** *via* its two hydrogen-bonds. Thus, the state change is linked to separate chromophore-protein interactions at opposite sides of the chromophore, *i.e.*, at $C12^3$ and the entire ring ***D***. The highly conserved His-290 – bound to the C19 carbonyl in Pr [53] and to the $C12^3$ carboxylic group in the Pfr-like ground state of PaBph3 [55] – faces inwards from a β-sheet at the surface of the molecule. Although the imidazole of its equally well conserved neighbor, His-291, is exposed to the solvent in both X-ray structures, a signaling mechanism is not obvious. Similarly, from the $C12^3$ no molecular signal pathway is immediately apparent although the interactions implied by the X-ray structures are very different in the Pr and Pfr states.

Conversely, no obvious changes are associated with the ring ***B*** propionic side-chain, although a salt bridge partner-swap between Arg-222 and Arg-254 is implied by the crystal structures and would accord with a similar possible re-arrangement in the oxygen-sensing domain of *Bradyrhizobium japonicum* FixL [53, 123].

On the other hand, the Asp-207/Arg-472 salt bridge connecting the PHY domain tongue to the chromophore region [53] is replaced by additional interactions with N24 and probably Ser-474 in the Pfr-like PaBph3 structure [55]. All these residues are highly conserved and are thus likely to fulfill essential functions in all phytochromes, Asp-207 being particularly important for stabilizing the Pfr state [19, 98]. The present data confirm that the hydrogen-bonding interaction between N24 and Asp-207 is associated with a break of the salt bridge between Asp-207 and Arg-472 in the Pfr state as implied by the PaBph3 structure [55]. It has to be pointed out, however, that the latter is not likely to be an entirely reliable model for the Pfr state in Cph1 and other plant-type phytochromes.

The tongue region comprises a most unusual hairpin structure inserted into the otherwise GAF/PAS-like PHY domain, making intimate contact with the extreme N-terminus of the molecule, itself unusual in forming a knot by passing through a loop in the GAF domain itself. The data presented in this chapter indicate that the Asp-207/Arg-472 association is likely to couple light-induced changes in chromophore geometry to the tongue and probably the N-terminus, thus it can be proposed that its disruption is central to photochromicity and/or the intramolecular signal transduction pathway. In the Lumi-F state, the ring ***D*** nitrogen is still hydrogen-bonded to Asp-207, while this interaction is disrupted in the Meta-F state, suggesting that the main re-arrangements of the protein are triggered at this step.

4.4 Materials and Methods

4.4.1 Sample preparation for MAS NMR spectroscopy

The u-[^{13}C,^{15}N]-PCB was prepared following the method presented in section 3.4.1. The chemical synthesis of the ^{15}N21-PCB sample has been carried out by Dr. C. Bongards (Max-Planck-Institut, Mülheim an der Ruhr, Germany). The synthesis is briefly described in the Appendix C.

4.4.2 MAS NMR spectroscopy

About 15 mg of u-[^{13}C,^{15}N]-PCB-Cph1Δ2 protein in the Pfr state were placed in a 4-mm zirconia rotor. The Lumi-F and Meta-F intermediate states were thermally trapped in the magnet by illumination through a far-red cut-off filter (λ_{max} = 730 nm) at 173 K and 203 K, respectively. The illumination setup used has been specially designed for a Bruker MAS probe [124]. 2D ^{13}C-^{13}C DARR experiments were performed at a field of 17.6 T on an Avance-WB750 spectrometer, equipped with a 4-mm triple resonance CP/MAS probe (Bruker, Karlsruhe, Germany). The ^{13}C-^{1}H dipolar interaction has been recovered by CW irradiation on ^{1}H RF intensity to satisfy the n = 1 condition. ^{1}H $\pi/2$- and ^{13}C π-pulse lengths were set at 3.1 and 5 μs, respectively. The ^{1}H power was ramped 80-100% during CP. Mixing times of 5 and 50 ms were used. ^{1}H CW decoupling was about 80 kHz during the proton mixing and about 43 kHz TPPM during acquisition. The DARR spectra were recorded with about 1 kscans, and with 8 μs evolution in the indirect dimension, leading to experimental times of about 60 h. The data were processed with the Topspin software version 2.0 (Bruker, Karlsruhe, Germany) and subsequently analyzed using the program Sparky version 3.100 (T. D. Goddard & D. G. Kneller, University of California, San Francisco, USA).

1D ^{15}N CP/MAS spectra were recorded using an AV-750 spectrometer, equipped with 4-mm CP/MAS probe. ^{1}H-^{15}N heteronuclear experiments were performed at the Avance-WB750, using a frequency switched Lee-Goldburg pulse sequence [68]. The proton $\pi/2$-pulse was set to 3.1 μs and the spinning frequency was 8 kHz.

Chapter 5

Discussion and outlook

In photoreceptors, the properties of the chromophore are influenced by the protein matrix. For instance, opsin contains the retinylidene cofactor in an 11-*cis*-12-*s*-*trans* conformation. MAS NMR spectroscopy has provided valuable information about the interaction between the retinylidene cofactor and its binding pocket in rhodopsin [125–127] by demonstrating that the non-bonding interaction between the C13 methyl group and the hydrogen of C10 give rise to a non-planar structure. The resulting torsions in the chromophore pre-configure the polyene for the photoisomerization occurring at the C11=C12 double bond [127–130]. A similar effect can be found for the phytochromes: PCB in its free state adopts a different conformation in solution (*ZZZsss*) than in its protein-bound state (*ZZZssa*), and the stabilization of the Pfr form (*ZZEssa*) is only accomplished by the protein.

PCB in its free state has been studied in **Chapter 2** and as chromophore in phytochrome in both **Chapter 3** and **Chapter 4**. Almost complete sets of ^{13}C and ^{15}N chemical shifts have been obtained for the free PCB and for the chromophore in the Pfr, Lumi-F, Meta-F and Pr states. In this chapter, the ^{13}C chemical shifts of PCB as free open-chain tetrapyrroles and chromophore in phytochrome are compared to elucidate the effect of the protein pocket.

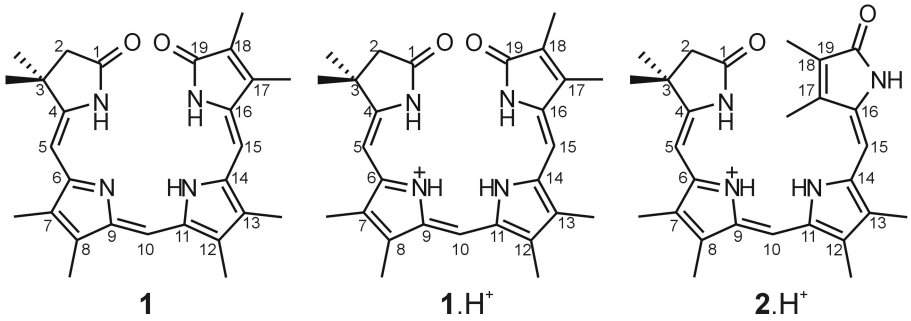


Figure 5.1: Structures of the **1** and **1**.H$^+$ model compounds in the *ZZZsss* geometry. **2**.H$^+$ is the *E*-diastereoisomer of **1**.H$^+$ in its *ZZEsss* geometry. The extent of positive charge is respresented on ring ***B***, as assumed in [103].

5.1 Comparison with model compounds

5.1.1 Effect of protein environment on PCB in phytochrome

In the late 1990's, Stanek and Grubmayr [103] have investigated the 2,3-dihydro-23*H*-bilin-1,19(21*H*,24*H*)-dione molecules **1**, **1**.H$^+$ and **2**.H$^+$ (Fig. 5.1). These three compounds are member of the 2,3-dihydrobilindione family. The compound **1** and its protonated form **1**.H$^+$ have been shown to adopt a helical shape with a *ZZZsss* geometry in $CDCl_3$ solution. The *E*-diastereoisomer of **1**.H$^+$, **2**.H$^+$, also occurs in a helical structure with a *ZZEsss* geometry. By comparing the chemical shift values of the carbons positioned symmetrically within the dipyrrin formed by rings ***B*** and ***C*** (C6 and C14, 152.4 *vs.* 142.1 ppm, respectively), Stanek and Grubmayr concluded that an extent of positive charge is located on ring ***B*** in **1**.H$^+$.

The change in ^{13}C chemical shift after the binding of PCB in the protein pocket in the Pr state is shown in Figure 5.2A. The effect observed at the ring ***A***, especially at the C3, C3^1, C3^2 and C4 (-82.8, -77.4, +5.7 and +7.7 ppm, respectively, Table 5.1) are in line with the formation of the thioether linkage with Cys-259 at C3^1.

The modification induced by the protonation of N22 occurring during the assembly of PCB in the protein pocket are visible at C6, C9, C12, C14 and C16. The effects of the protonation of N22 on the ^{13}C chemical shifts in the model compound **1** are depicted in Figure 5.2B. Comparing Figures 5.2A and B, the overall patterns of the change in ^{13}C chemical shift are similar. C6 and

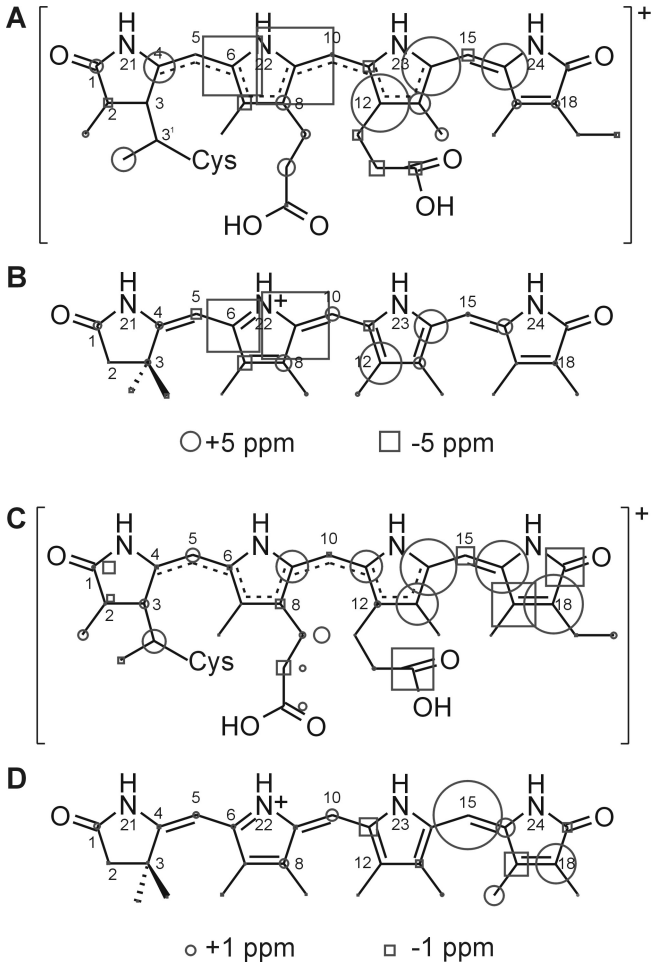


Figure 5.2: The upper part (**A** and **B**) shows the change in ^{13}C chemical shifts resulting from the assembly of PCB into Cph1Δ2 (PCB → Pr, **A**) and upon protonation of **1** (**1** → **1**.H$^+$, **B**). The lower part (**C** and **D**) represents the changes in ^{13}C chemical shifts accompanying Pr → Pfr conversion (**C**) and the difference in ^{13}C shifts between the models compound of the **1**.H$^+$ and **2**.H$^+$ (**D**). The free PCB (A form), **1**, Pr and **1**.H$^+$ are taken as reference in **A**, **B**, **C** and **D**, respectively. The upshifts of the ^{13}C resonances of C3 and C3^1 due to the formation of the thioether linkage with Cys-259 (82.8 and 77.4, respectively) are not represented in **A**.

Position	**1**	**1**.H$^+$	**1** → **1**.H$^+$	PCB	Pr	PCB → Pr
C1	175.9	177.9	2.0	179.4	182.5	3.1
C2	44.2	44.0	-0.2	39.3	37.1	-2.2
C3	39.5	40.9	1.4	136.2	53.4	-82.8
C3^1	29.4	28.5	-0.9	125.2	47.6	-77.4
C3^2	—	—	—	16.1	21.8	5.7
C4	159.3	161.1	1.8	146.2	153.9	7.7
C5	89.9	87.4	-2.5	87.0	87.1	0.1
C6	166.0	152.4	-13.6	164.7	149.1	-15.6
C7	131.0	127.5	-3.5	129.5	126.1	-3.4
C7^1	9.9	9.8	-0.1	9.3	9.2	-0.1
C8	139.5	143.6	4.1	142.1	144.5	2.4
C8^1	9.9	10.6	0.7	22.9	22.5	-0.4
C8^2	—	—	—	36.8	43.1	6.3
C8^3	—	—	—	180.0	180.5	0.5
C9	149.4	132.0	-17.4	147.8	127.7	-20.1
C10	111.3	114.8	3.5	112.2	112.7	0.5
C11	132.7	130.3	-2.4	130.6	127.7	-2.9
C12	128.6	139.4	10.8	130.8	145.5	14.7
C12^1	9.5	10.4	0.9	20.4	21.1	0.7
C12^2	—	—	—	42.4	37.5	-4.9
C12^3	—	—	—	182.2	179.5	-2.7
C13	124.2	127.1	2.9	121.3	126.3	5.0
C13^1	9.4	9.8	0.4	8.4	11.3	2.9
C14	133.5	142.1	8.6	131.1	145.7	14.6
C15	96.6	97.5	0.9	96.0	93.5	-2.5
C16	136.3	140.2	3.9	134.3	145.7	11.4
C17	141.7	142.1	0.4	140.1	142.2	2.1
C17^1	10.0	9.8	-0.2	10.1	9.8	-0.3
C18	127.6	128.6	1.0	132.0	134.3	2.3
C18^1	8.7	8.2	-0.5	16.8	16.1	-0.7
C18^2	—	—	—	14.3	13.3	-1.0
C19	173.6	173.5	-0.1	173.7	172.8	-0.9

Table 5.1: ^{13}C chemical shifts of **1** and **1**.H$^+$ are taken from [103]. PCB (A form) and Pr have been studied in **Chapter 2** and **Chapter 3**, respectively.

C9 are respectively upshifted by 13.6 and 17.4 ppm in the model compound, while the upshifts of these resonances are of 15.6 and 20.1 ppm upon assembly in the protein (Table 5.1). These strong changes can be directly related to the protonation on N22. The significant downshifts at C12 and C14 are also observed in both Figures 5.2A and B, indicating that the protonation of N22 induces a modification of the electronic structure of the tetrapyrroles moieties. The downshifts at C12 and C14 are markedly larger upon assembly of PCB in the protein (14.7 and 14.6 ppm, respectively) than in the model compound (10.8 and 8.6 ppm, respectively). The more pronounced up- and downshift of the ^{13}C chemical shifts in the protein suggest that the protein pocket has an

influence on the positive charge delocalization over the rings ***B*** and ***C*** in the Pr state.

On the other hand, despite the overall similarity of the pattern, the changes in the ^{13}C resonances along the C15 methine bridge are significantly stronger in the case of the PCB assembly in the protein compared to the protonation of the model compound. Hence, these differences indicate an additional effect of the protein environment at these positions. Indeed, the PCB molecule adopts a *ZZZsss* geometry in its free state (**Chapter 2** and [24]), while the X-ray structure in the Pr state revealed a *ZZZssa* geometry in the protein [53]. Therefore, the *syn*-to-*anti* conformational change of the C14-C15 single bond appears to be caused by the protein inducing a dihedral angle of 26.3° between the planes formed by rings ***C***–***D*** [53]. In the X-ray structure of Cph1Δ2, the *anti* conformation appears to be stabilized by the hydrogen-bonding interaction between the C19 carbonyl and N24 with His-290. In addition, the methyl substituent at C17 is close to the Tyr-263 hydroxyl (2.66 Å). Apparently, this steric interaction prevents a more planar conformation between rings ***C***–***D***. In this geometry, the C13^1 methyl group is in close contact with N24 (2.84 Å). It can be assumed that this steric interaction is responsible for the enhanced downshift of the C13 and C13^1 resonances. It cannot, however, currently be decided whether these effects around the C15 methine bond are caused solely by steric or also electronic effects.

5.1.2 Pr → Pfr conversion

The changes in ^{13}C chemical shifts caused by the Pr → Pfr conversion in Cph1Δ2 (Fig. 5.2C) have been analyzed in **Chapter 3**. The changes along the C15=C16 double bond and in the entire ring ***D*** in Cph1Δ2 have been related to the formation of the strong hydrogen-bonding interaction of the C19 carbonyl in the Pfr state, which lowers the bond order of the C15=C16 and the C17=C18 bonds and to a potential redistribution of the positive charge.

The differences in the ^{13}C resonances between **1**.H$^+$ and its *E*-diastereoisomer **2**.H$^+$ are depicted in Figure 5.2D. The patterns of the Figures 5.2C and D, in particularly along the C15 methine bridge, are significantly different. The alternating up- and downshift pattern is inverted from C8 to C15. The C14, C15 and C16 are shifted by +5.4, -1.8 and +5.0 ppm in Cph1Δ2, respectively, while the corresponding differences between **1**.H$^+$ and **2**.H$^+$ are

of -0.1, +7.1 and +1.9 ppm (Table 5.1). Although the alternating up- and downshifts of the ^{13}C resonances between C16 and C19 have the same phase, they are remarkably stronger for the protein-bound case and may indicate an increase of charge density alternation between the odd and even numbered carbon atoms at these positions.

Obviously, the double-bond isomerizations in both systems are of fundamentally different characters. For the isomerization in phytochrome, ring ***C*** has been proposed to be the hot spot for the change of the electronic structure, involving a potential redistribution of the positive charge along the chromophore (**Chapter 3**). The double bound isomerization of the model compound is expected to occur in a classical way, *i.e.* a rotation of 180°, as for example in the well-investigated stilbene [131]. In addition, the C14–C15 single bonds of the **1**.H$^+$ and **2**.H$^+$ model compounds have a *syn* conformation in solution, while this single bond forced into an *anti* conformation in both Pr and Pfr states [18, 51–53, 55]. The *anti* conformation of the C14–C15 in phytochrome induces an intramolecular interaction between the C13^1 and C17^1 methyl groups and may prevent planarity of the rings ***C*** and ***D*** in the Pfr state. The pattern of the change in ^{13}C chemical shift at the C15 methine bridge in Cph1Δ2 may originate from the contribution of three effects: steric interaction, hydrogen-bonding interaction and extended delocalization of the positive charge in the Pfr state.

5.1.3 Photoisomerization in phytochrome

In the free state, open-chain tetrapyrroles commonly adopt a helical shape with a *ZZZsss* geometry, as it has been shown for the biliverdin dimethyl ester-IXα in solution [132, 133] as well as in its crystalline state [85]. Upon irradiation with white light, the photochemistry of the biliverdin dimethyl ester IXα leads to *Z*-to-*E* photoisomerizations at one of the two outer methine bridge, *i.e.*, at C4=C5 and C15=C16, while no photoisomerization has been observed at the central C10 methine bridge [132, 134]. On the other hand, time-dependent DFT calculations suggest that an isolated protonated PCB moiety forms photochemically preferably C10-methine isomers [135].

In phytochrome, the photoisomerization is generally accepted to occur selectively at the C15=C16 double bond of the chromophore. The NMR data obtained in this thesis are in agreement with this assumption. Since the intrinsic reactivity of the free protonated chromophore may favor a photoreaction

at C10, the localization of the photoisomerization in phytochrome may be a result of chromophore/protein interactions, which modulate and tune the photochemical properties of the bound chromophore. All crystal structures of phytochromes show that PCB binds to the protein with *Z*, *anti* geometry at the C15 methine bridge. The rings ***A***, ***B*** and ***C*** are tightly packed into the protein pocket. The steric interactions, for example by His-260, as well as the hydrogen-bonding interactions fix the structure in a state in which rings ***A***, ***B*** and ***C*** are almost coplanar, and may thus prevent photoisomerization at the C5 and C10 methine bridges. This is in line with the moderate chemical shift changes observed at these positions (Fig. 5.2C). On the other hand, ring ***D*** is rotated by an angle of about 25 to 45° [18, 51–53] and resides in a cavity that allows for relatively unhindered rotation around the C15 methine bridge. The relative freedom of ring ***D*** and the torsion around the C14–C15 bond may direct the photoisomerization at the methine bridge between rings ***C*** and ***D***.

5.2 Results and prospects

The experimental results obtained in this thesis have demonstrated that the combination of isotope labeling and solid-state NMR spectroscopy is a powerful tool for the investigation of the photochemical switching machinery of phytochrome. The ^{1}H, ^{15}N and ^{13}C assignments provided information at the atomic level about the specific chromophore/protein interactions within the chromophore binding domain in the Pfr, Lumi-F, Meta-F and Pr states. The ^{13}C chemical shift data of the chromophore allow for determination of the electronic structure of the chromophore in these states. Due to selective isotope labeling of N21 and the study of the free PCB, one of the four ^{15}N signals, N21, has been assigned, and a tentative assignment of N22, N23 and N24 has been proposed for all studied states.

In **Chapter 3**, it has been shown that the chromophore is stabilized by hydrogen-bonding interaction at the C19 carbonyl group. The increase in length and strength of the conjugation of the π-system implies a strong hydrogen-bonding interaction at the carbonyl of ring ***D***, causing the red shift of the maximum of absorption in the Pfr state. It has been proposed that Tyr-263 acts as hydrogen-bonding partner of C19.

MAS NMR provided new insights into the mechanism of the back-reaction.

The ability to produce samples in the pure Pfr state combined with low-temperature MAS NMR and an illumination setup allowed for trapping and studying of the two intermediates of the back-reaction, Lumi-F and Meta-F (**Chapter 4**). It has been shown that N24 also contributes to the stabilization of the chromophore in the Pfr state *via* hydrogen-bonding interaction with Asp-207. The back-reaction process begins with the photoisomerization of the C15=C16 double bond, which is followed by the rupture of the hydrogen-bonding interaction of N24, enabling the rotation of the C14–C15 single bond to take place. The method presented here for the study of the Pfr → Pr conversion may also be applied to the investigation of the intermediates present in the pathway from Pr → Pfr.

The ^{13}C and ^{15}N chemical shifts presented in **Chapter 3** and **Chapter 4** are the ideal starting point for theoretical studies, which may probe the proposed increase in conjugation of the π-system in the Pfr state. In addition, DFT calculations may bring further insights about the location of the positive charge within the chromophore as well as the potential redistribution of this charge during the photocycle.

The ^{13}C and ^{15}N assignments in the Pfr, Lumi-F, Meta-F and Pr states presented in this thesis will help to design further MAS NMR experiments, which are required to elucidate the changes of the hydrogen-bonding network within the chromophore binding site. In particular, MeLoDi-type of long-distance ^{1}H-^{13}C or ^{1}H-^{15}N heteronuclear correlation MAS NMR experiments and selective labeling of individual amino acids will help to investigate the complex cofactor/protein interactions [126, 136]. In addition, the measurement of internuclear distances [137] and angles [138] by MAS NMR would provide the structural information required for the full description of the rotation of ring ***D*** and allow for probing of the behavior of the C5 and C10 methine bridges.

Due to the similarity of the NMR spectra of Cph1Δ2 and *phyA*65 in the two parent states Pr and Pfr (**Chapter 3**), most of the interactions occurring in Cph1Δ2 are believed to be also present in plant Phys. However, small but distinct differences in ^{13}C shift are observed, especially at the methine bridge between ring ***C*** and ***D***. The 1D ^{15}N spectra of the Cph1Δ2 and *phyA*65 assembled to an uniformly ^{15}N labeled PCB chromophore in the Pfr, Meta-F and Pr states are presented in Figure 5.3. In analogy to the ^{13}C NMR spectra, the pattern of the ^{15}N spectra of Cph1Δ2 and *phyA*65 are similar. However,

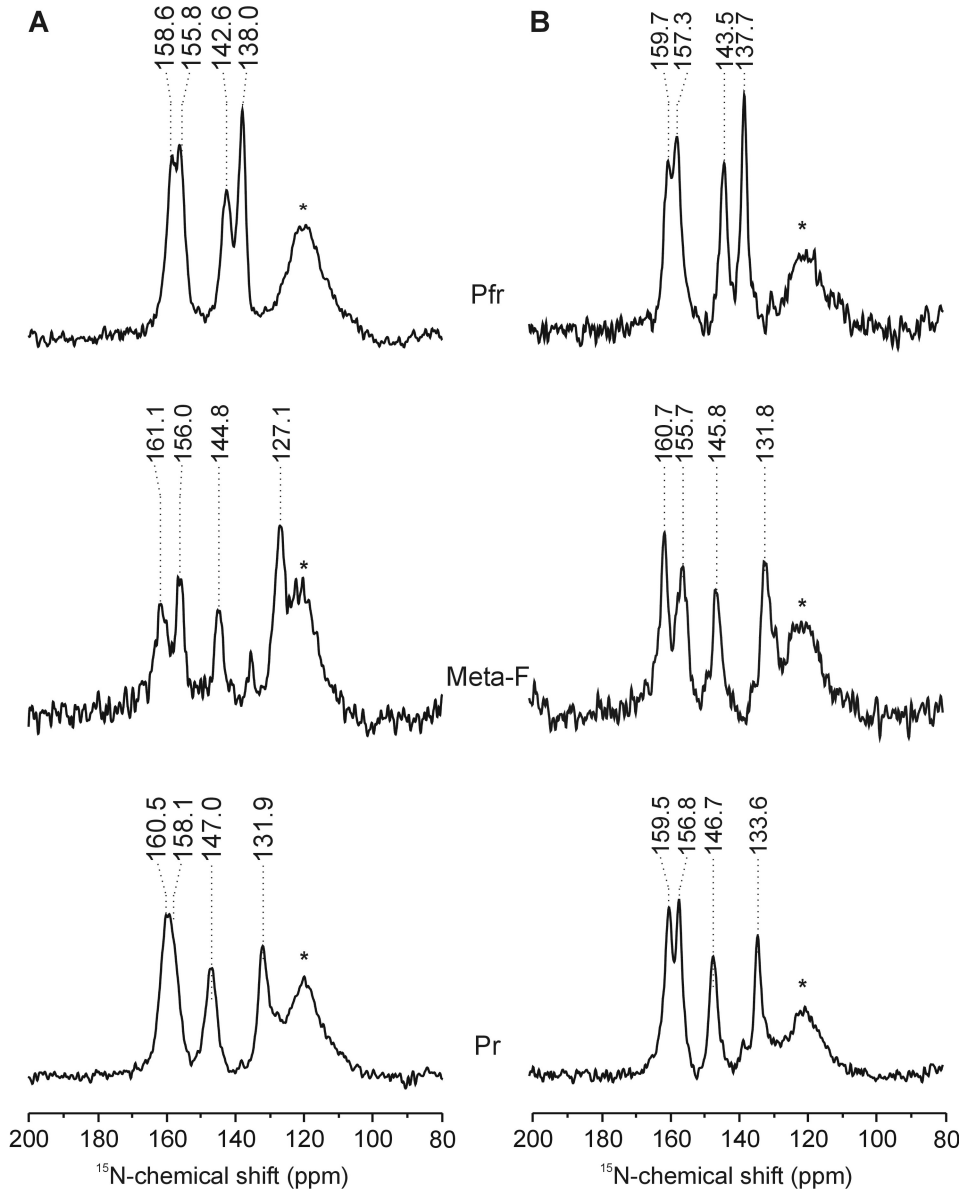


Figure 5.3: 1D ^{15}N CP/MAS NMR spectra of Cph1Δ2 (**A**) and *phyA*65 (**B**) containing an u-[^{13}C,^{15}N]-PCB chromophore. The spectra were recorded in a field of 17.6 T and a spinning frequency of 8 kHz.

clear differences are observed at N24, especially in the Meta-F states (127.1 and 131.8 ppm for Cph1Δ2 and *phyA*65, respectively). In **Chapter 4**, it has been proposed that the large difference in ^{15}N chemical shift of N24 in the Meta-F and Pr states (127.1 and 131.9 ppm, respectively) is due to the weakness or even the absence of hydrogen-bonding interaction at N24 in the Meta-F state. As shown in Figure 5.3, the resonance of N24 in *phyA*65 occurs at 131.8 and 133.6 ppm in Meta-F and Pr, respectively. In *phyA*65, N24 is downshifted by 1.8 ppm in the Meta-F state (compared to Pr), this downshift is significantly weaker than in Cph1Δ2 (4.7 ppm). Hence, it appears that in plant Phys the environment of N24 in the Meta-F state is already relatively similar to the one in Pr, while N24 is still very different in the Meta-F and Pr states in Cphs. That may explain why previous vibrational spectroscopic studies on plant Phy reported very similar spectra for Meta-F and Pr [43].

As concluding remark, the methodology described in this thesis sets the stage for studying the chromophore/protein interactions within Cphs and plant Phys during their respective photocycle. This will contribute to a better understanding of the light-induced chromophore activity and signal transduction pathway in Phys.

The mechanistic understanding of the photochemical processes in Phy may also allow for comparison with analogue studies on other photoreceptors and will allow looking into the fundamental principles of naturally occurring photo-switches. Understanding the basic principles of the natural photo-switches may also inspire construction of efficient artificial nano photo-switches.

Appendices

Appendix A

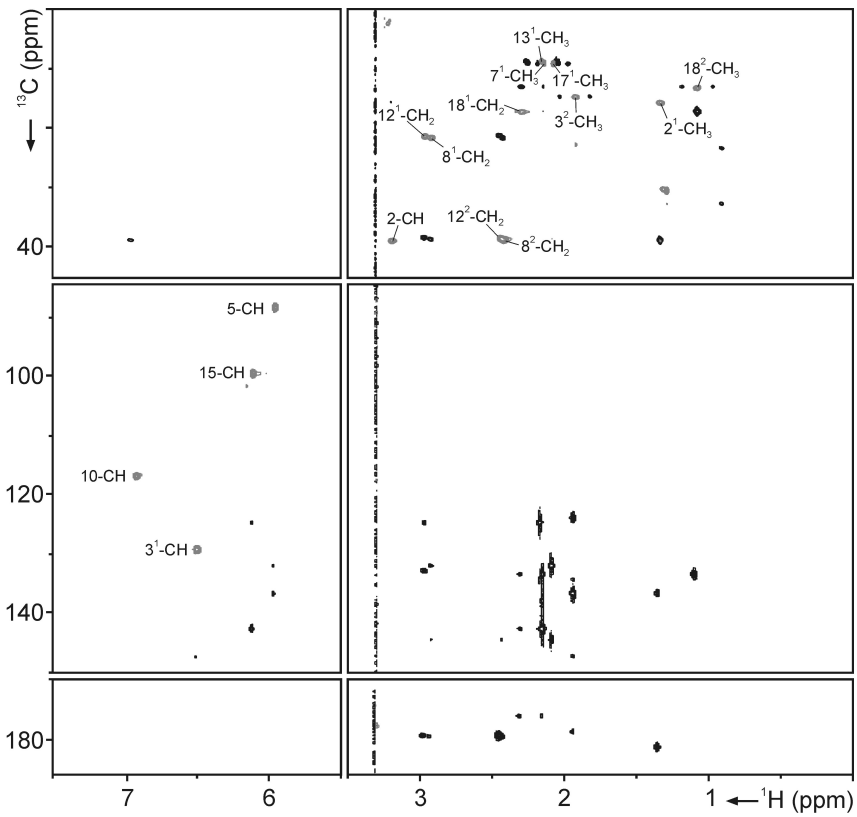


Figure A.1: Contour plot of the ^{1}H-^{13}C HSQC (black) and ^{1}H-^{13}C HMBC (grey) NMR dipolar correlation spectra of PCB in methanol-d$_4$ recorded in a magnetic field of 14.1 T at 277 K. The HSQC assignments of correlations are indicated.

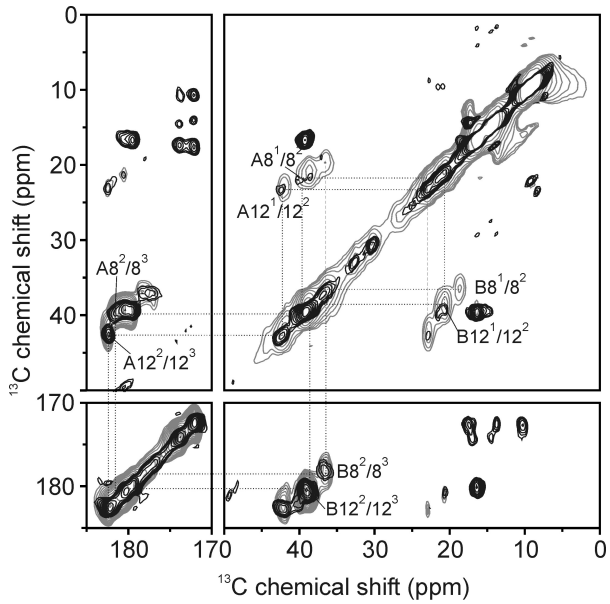


Figure A.2: Contour plot of the 2D ^{13}C-^{13}C RFDR (t_{mix} = 3.9 ms, black) and PDSD (t_{mix} = 2.4 ms, grey) MAS NMR spectra of u-[^{13}C, ^{15}N]-PCB-Cph1Δ2. The connectivity networks of the propionic acid side-chains are indicated by dotted lines.

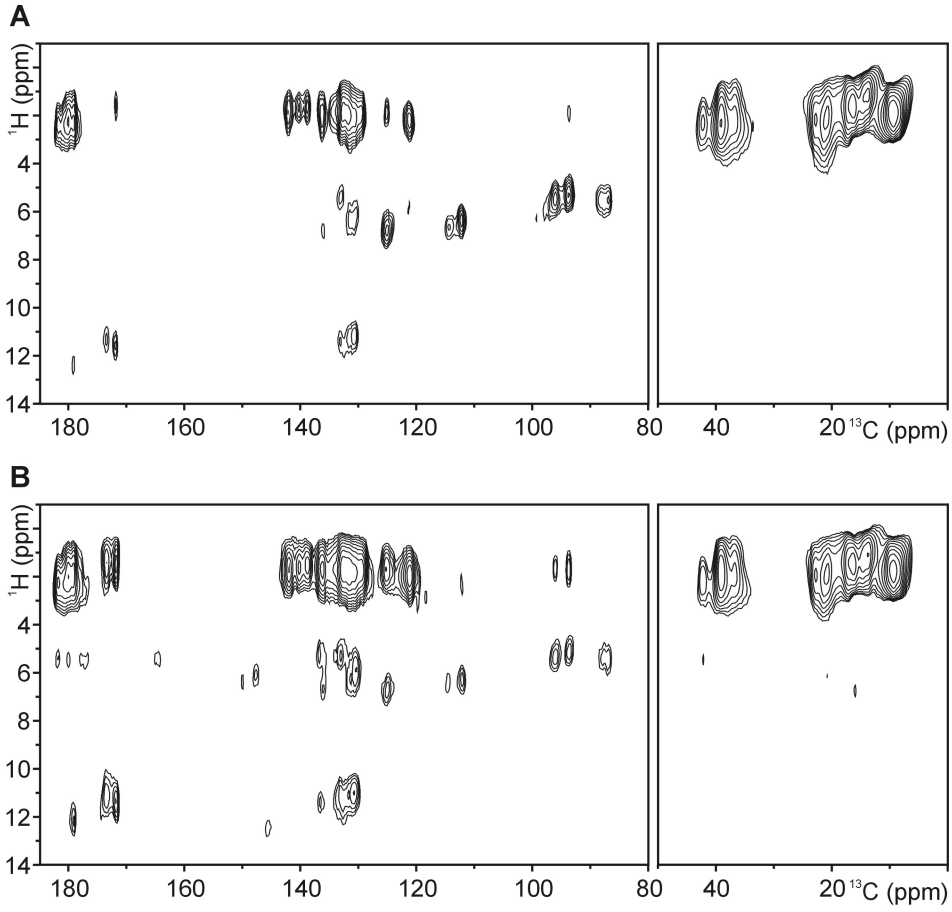


Figure A.3: Contour plot of the ^{1}H-^{13}C FSLG NMR dipolar correlation spectra of u-[^{13}C,^{15}N]-PCB recorded at 277 K in a magnetic field of 17.6 T using a spinning frequency of 12 kHz and CP contact times of 512 μs (**A**) and 1024 μs (**B**).

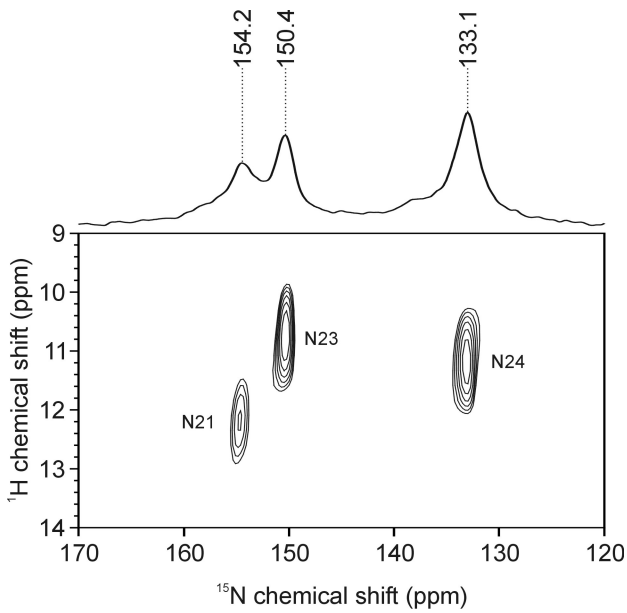


Figure A.4: Contour plots of the 2D ^{1}H-^{15}N heteronuclear dipolar correlation spectrum of u-[^{13}C,^{15}N]-PCB recorded at 277 K in a field of 17.6 T using a spinning frequency of 7 kHz.

Appendix B

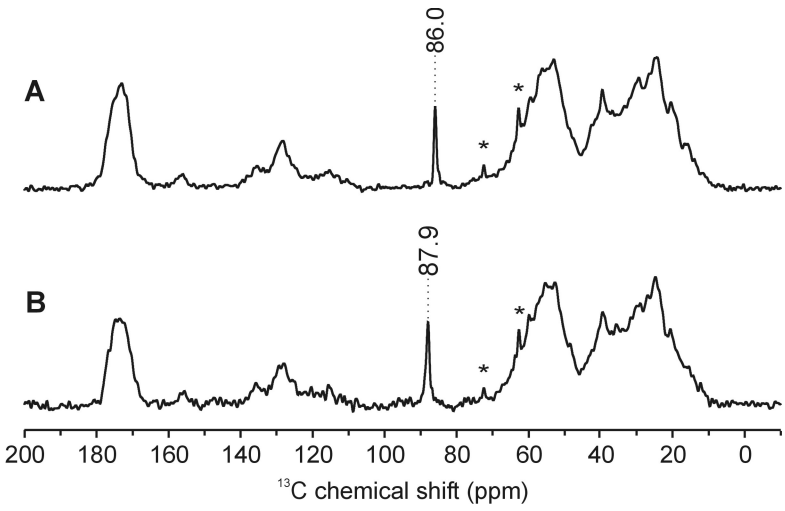


Figure B.1: 1D ^{13}C CP/MAS NMR spectra of ^{13}C5-PCB-*phyA*65 in the Pr (**A**) and Pfr (**B**) states recorded at 9.4 T, 10 kHz and 243 K. The asterisks indicate the ^{13}C response of the glycol present in the buffer.

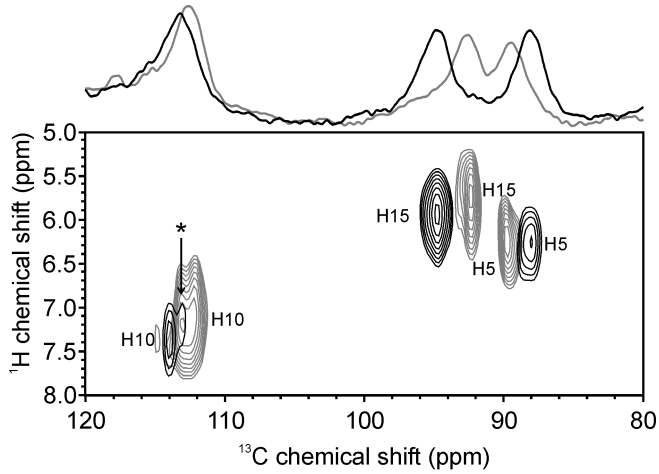


Figure B.2: Contour plot of 2D ^{1}H-^{13}C heteronuclear dipolar correlation spectra of the methine bridge region obtained from u-[^{13}C,^{15}N]-PCB-Cph1Δ2 in the the Pr (black) and Pfr (grey) states at a magnetic field of 9.4 T, 10 kHz and 243 K. The asterisk indicates the position of protein backbone signals in natural abundance.

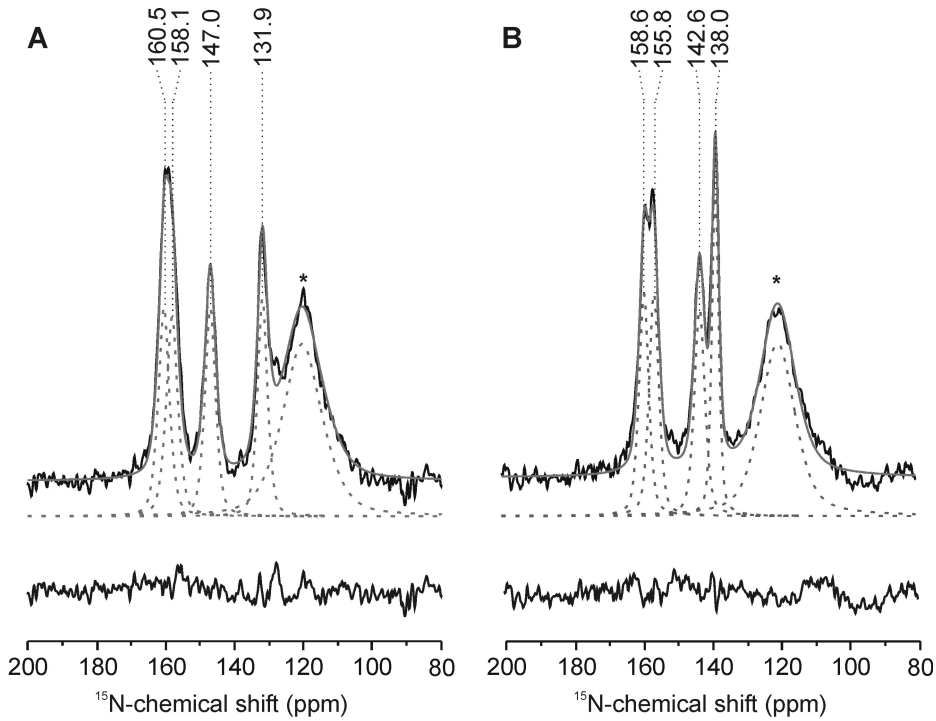


Figure B.3: Voigt deconvolution of the ^{15}N CP/MAS NMR spectra of u-[^{13}C,^{15}N]-PCB-Cph1Δ2 in the Pr (**A**, 80000 scans) and Pfr (**B**, 135000 scans) recorded in a magnetic field of 17.6 T at 243 K using a spinning frequency of 8 kHz. The upper part compares the experimental NMR spectrum with the sum of the Voigt fits. The lower part gives the individual Voigt fits (dashed lines) and the residual spectra. The asterisk indicates the ^{15}N response of the protein backbone in natural abundance.

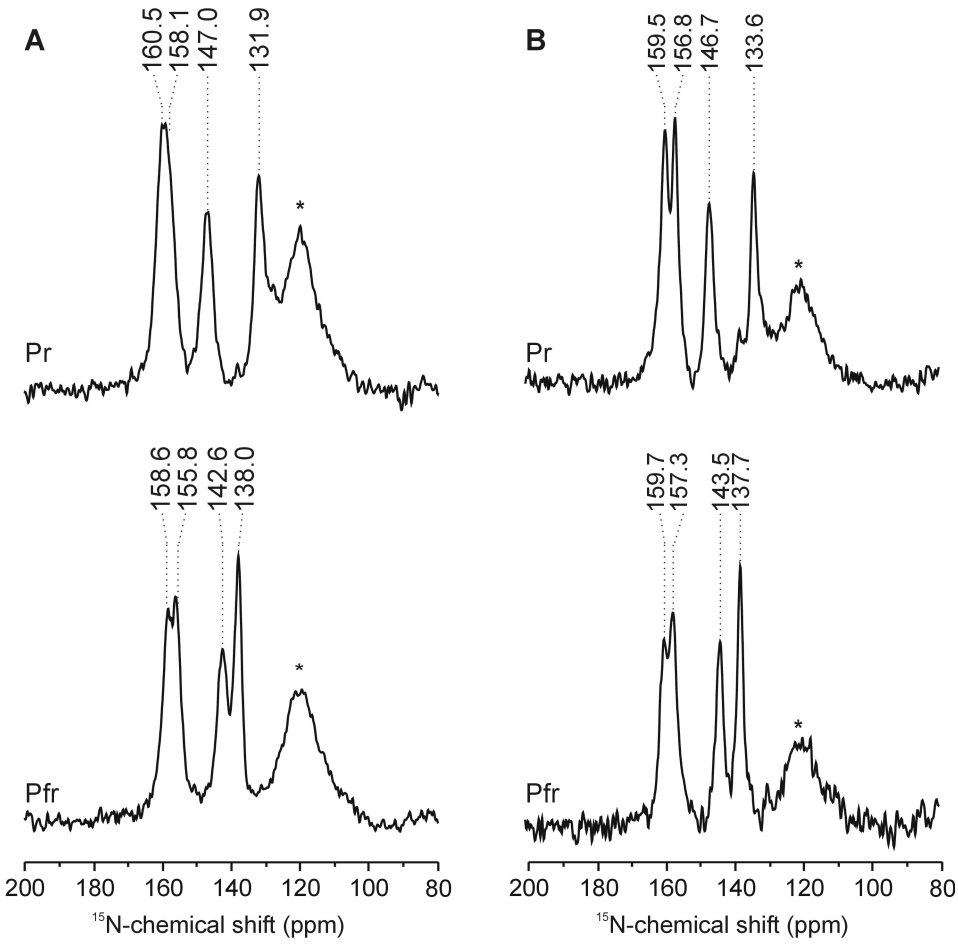


Figure B.4: ^{15}N CP/MAS NMR spectra of Cph1Δ2 (**A**) and *phyA*65 (**B**) containing an u-[^{13}C,^{15}N]-PCB in the Pr and Pfr states recorded in a magnetic field of 17.6 T at 243 K using a spinning frequency of 8 kHz. The ^{15}N response of the protein backbone in natural abundance is indicated by an asterisk.

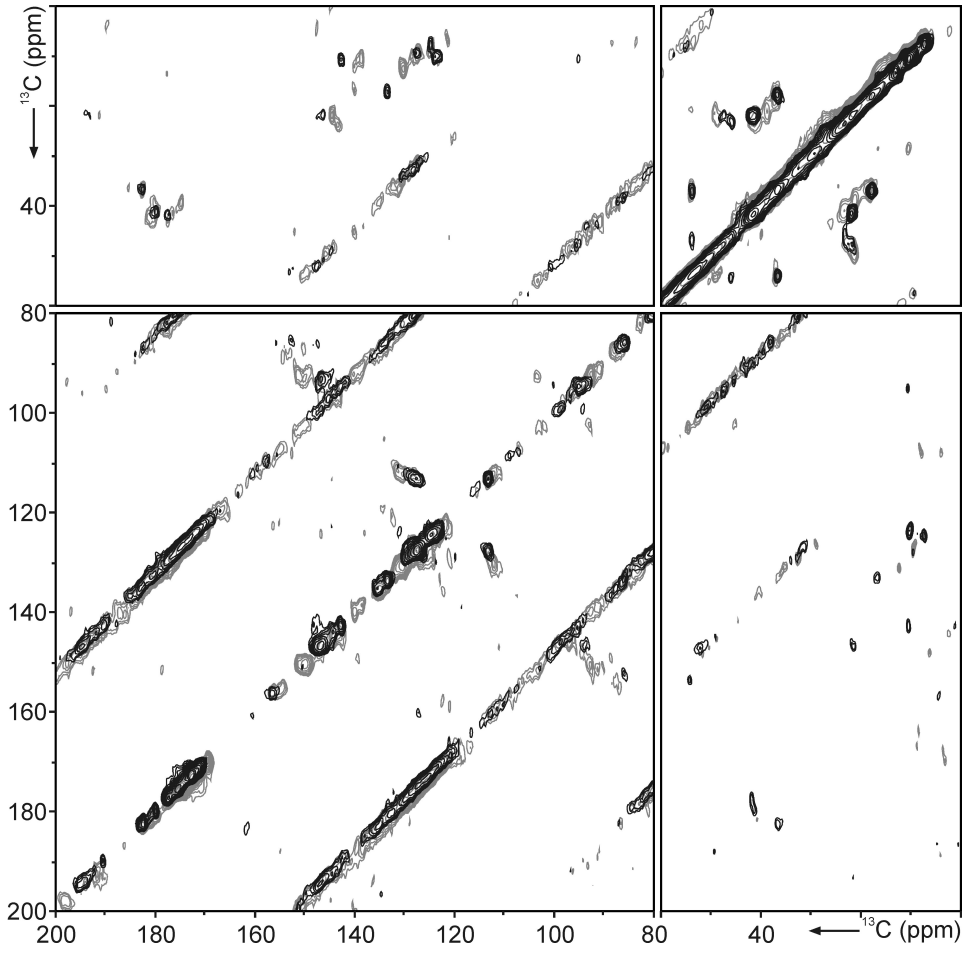


Figure B.5: Contour plot of the 2D ^{13}C-^{13}C DARR NMR spectra of u-[^{13}C,^{15}N]-PCB-*phyA*65 in the Pr (black) and Pfr states (grey). The spectra were recorded with proton mixing times of 5 ms, at 243 K and with a spinning frequency of 9 kHz.

Appendix C

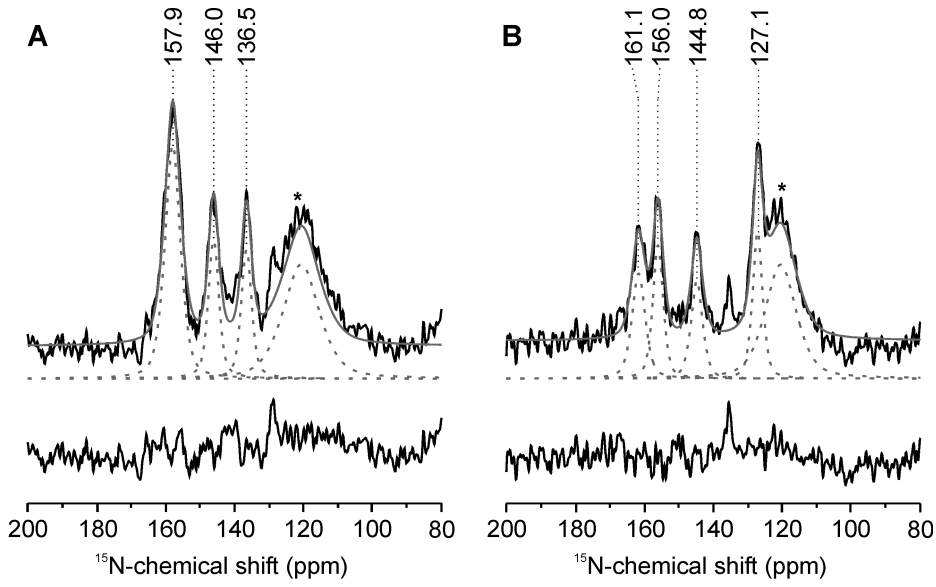


Figure C.1: Voigt deconvolution of the ^{15}N CP/MAS NMR spectra of u-[^{13}C,^{15}N]-PCB-Cph1Δ2 in the Lumi-F (**A**) and Meta-F (**B**) recorded in a magnetic field of 17.6 T at 173 K and 203 K, respectively, using a spinning frequency of 8 kHz. The upper part compares the experimental NMR spectrum with the sum of the Voigt fits. The lower part gives the individual Voigt fits (dashed lines) and the residual spectra.

Chemical synthesis of ^{15}N21-PCB-Cph1Δ2

^{15}N21-PCB was synthesized by Dr. Bongards (Max-Planck-Institut für Bioanorganische Chemie, Mülheim an der Ruhr, Germany). The synthesis of 4*E*-4-ethylidene-3-methyl-5-thioxo(^{15}N)pyrrolidin-2-one (**6**) follows the synthesis scheme presented in Figure C.2.

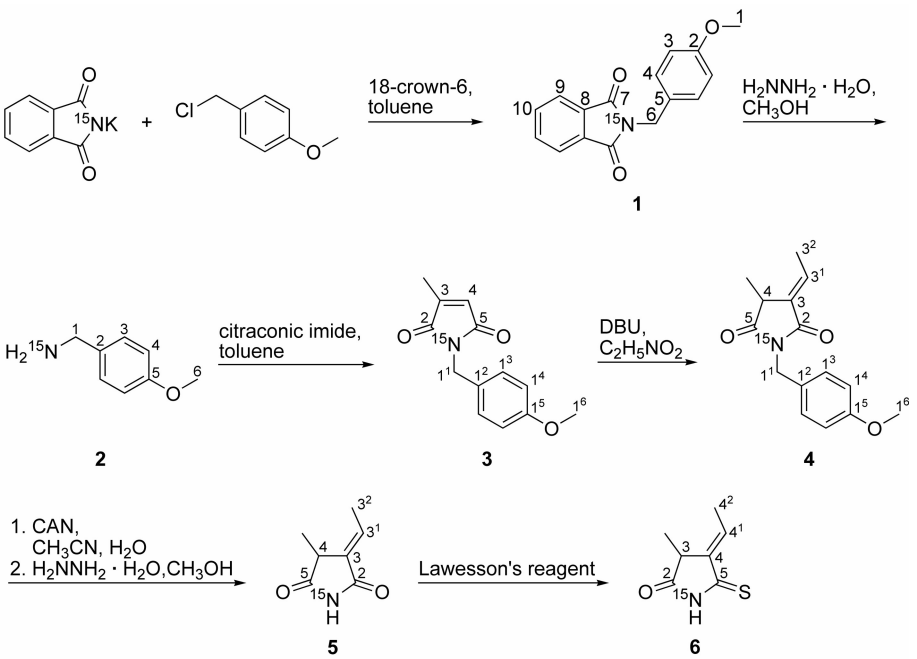


Figure C.2: Synthesis scheme applied for the the chemical synthesis of (4*E*)-4-ethylidene-3-methyl-5-thioxo(^{15}N)pyrrolidin-2-one (**6**).

2-(4-Methoxybenzyl)(^{15}N)-1*H*-isoindole-1,3(2*H*)-dione (**1**): A dispersion of ^{15}N-labeled potassium phthalimide (10.00 g, 53.7 mmol), 1-(chloromethyl)-4-methoxybenzene (6.1 mL, 44.8 mmol), and 18-crown-6 (1.18 g, 4.5 mmol) in toluene (58 mL) was stirred under argon at 100 °C for 5 h. After cooling to ambient temperature, water (150 mL) was added to the mixture. The resulting phases were separated, the aqueous phase was extracted with dichloromethane (4 × 50 mL) and the combined organic phases were dried over Na_2SO_4. Evaporation of the solvent and drying of the remaining pale yellow solid under reduced pressure yielded the reaction product **1** (12.01 g, 44.8

mmol, 100 %) which could be used in the following reaction without further purification.

1-(4-Methoxyphenyl)methan(^{15}N)amine (**2**): A dispersion of **1** (6.41 g, 23.9 mmol) and hydrazine hydrate (51 % hydrazine, 96 mL, 1.0 mol) in methanol (1.4 L) was refluxed for 5 h. After evaporation of the solvent under reduced pressure, the remaining oil was dissolved in dichloromethane (500 mL), washed with NaOH (1 M, 5 × 100 mL) and dried over Na_2SO_4. Evaporation of the solvent under reduced pressure yielded the reaction product **2** (3.20 g, 23.2 mmol, 97 %) as a yellow, clear oil.

In general, the preparation of **6** follows the synthetic route of the unlabeled ring ***A*** compound established by Kakiuchi *et al.* [139]. Transformation of the ^{15}N21-labeled ring ***A*** compound **6** to the full tetrapyrrole followed published procedures [140, 141].

Summary

The protein phytochrome is responsible for light-induced physiological changes (photomorphogenesis) in plants. This chromoprotein also occurs in bacteria, cyanobacteria and fungi. The activity of phytochromes relies on an open-chain tetrapyrrole chromophore which is covalently bound to a cysteine residue *via* a thioether linkage at the $C3^1$ or $C3^2$ position of the side chain of ring ***A***. In the case of Cph1Δ2, the three methine bridges of the PCB chromophore adopt a *ZZZssa* geometry in the biologically inactive Pr state. Upon absorption of red light, the C15=C16 double bond undergoes a *Z*-to-*E* photoisomerization leading to the conversion into the active Pfr state *via* three intermediates. The thermally stable Pfr state is converted back to Pr upon absorption of far-red light. The back-reaction presents two intermediates, called Lumi-F and Meta-F. The first step of the back-reaction is the *E*-to-*Z* isomerization of the C15=C16 double bond. The aim of this thesis is to provide an understanding of the light-induced chromophore mechanics and its coupling to the intramolecular signal transduction pathway. To this end, MAS NMR spectroscopy is applied to Cph and plant Phy proteins.

The study of the free PCB may be useful for understanding its complex behavior inside the protein matrix. **Chapter 2** deals with the investigation of the free PCB in the microcrystalline state. ^{1}H, ^{13}C and ^{15}N MAS NMR spectroscopy reveals that two forms of PCB moieties, called A and B, are present in equal proportions in the microcrystal. In addition ^{15}N CP/MAS data show that solely the nitrogen atom of ring ***B*** is unprotonated. The structure of PCB in the microcrystalline sample is determined by a combination of MAS NMR and quantum mechanical calculations. It is shown that the PCB moieties form ***D***–***D***' dimers linked by hydrogen-bonding interactions between the nitrogen of ring ***D*** and the carbonyl group of ring ***D***' and *vice versa*.

In **Chapter 3**, both parent states, Pr and Pfr, have been studied by ^{1}H, ^{13}C and ^{15}N CP/MAS NMR in the Cph1Δ2 and *phyA*65 phytochrome sensory modules containing an u-[^{13}C,^{15}N]-, ^{13}C5- or ^{15}N21-PCB labeled bilin chromophore. 2D homo- and heteronuclear experiments allowed for the assignment of the ^{13}C and ^{15}N chemical shifts in both states. The chromophore in Cph and plant Phy shows similar features in their respective Pr and Pfr states. The ^{15}N chemical shift analysis reveals that all four nitrogen atoms are protonated in both states. Differences in ^{13}C chemical shift reflect the changes of the electronic structure of the cofactor at the atomic level as well as its interactions with the chromophore binding pocket. The ^{13}C data are interpreted in terms of a strengthened hydrogen-bond at the ring ***D*** carbonyl in the Pfr state. The red shift of the maximum of absorption in the Pfr state is explained by the increasing length of the conjugation network beyond ring ***C*** including the entire ring ***D***. The enhanced conjugation within the π-system stabilizes the strained chromophore in the Pfr state. Concomitant changes at the ring ***C*** propionic side chain and the ring ***D*** carbonyl are explained by a modification of their hydrogen-bonding to His-290. These and other conformational changes may lead to modified surface interactions.

Chapter 4 describes the photochemically induced Pfr → Pr back-reaction. The light-triggered Pfr → Pr conversion is followed at low temperature by MAS NMR spectroscopy. Both Lumi-F and Meta-F intermediates have been thermally trapped in the magnet and all four states, Pfr, Lumi-F, Meta-F and Pr have been characterized. The mechanical process of the back-reaction involves the bond rotation around the C15 methine bridge, which occurs in two distinguishable steps: (*i*) In the Lumi-F state, the C15=C16 double bond is photoisomerized, (*ii*) the rotation along the C14–C15 single bond occurs during the transformation to Meta-F. The structural analysis reveals that the chromophore adopts a distorted conformation in Lumi-F. The Meta-F intermediate shows features similar to Pr, however, the final hydrogen-bonding interactions of the ring ***D*** nitrogen are still to be formed and a protein re-arrangement around ring ***A*** still has to take place. A model for the back-reaction is presented.

Tetrapyrrole moieties have been extensively studied by liquid-state NMR spectroscopy. In particular, the members of the 2,3-dihydrobilindione family are good model compounds for the chromophore in phytochrome. In **Chapter 5**, the ^{13}C chemical shifts of such compounds are compared to those of PCB

in its free state and as chromophore in phytochrome. In this way, information about the chromophore/protein interactions resulting from PCB assembly and upon the Pr → Pfr conversion is obtained. First, the change in ^{13}C chemical shifts in PCB caused by its assembly in the protein shows that rings ***B*** and ***C*** are symmetrical in the protein matrix, suggesting that the positive charge is delocalized over the two inner rings in the Pr state. Second, the chromophore assembly into the protein imposes new constrains to the chromophore. The strongest effect is located around the C15 methine bridge, which adopts a (*Z*, *anti*) geometry in the protein. The pattern of change in ^{13}C chemical shift caused by the *Z*-to-*E* isomerization in protonated model compound in solution is entirely different from that one observed upon the Pr → Pfr conversion. This demonstrates that the chromophore/protein interactions drastically influence the electronic structure. Finally, future perspectives for MAS NMR on phytochrome are discussed. For instance, distance and angle measurements by MAS NMR can provide information about the change in geometry of the chromophore throughout the photocycle. In addition, MeLoDi-type of NMR experiments can be used to investigate the chromophore/protein interaction at various stage of the photocycle. In this way, the photo-triggered activity of the chromophore can be related to the signal transduction in phytochrome.

Samenvatting

Het eiwit phytochroom is verantwoordelijk voor de licht-geïnduceerde fysiologische veranderingen (fotomorfogenese) in planten. Dit chromo-eiwit wordt ook in bacteriën, cyanobacteriën en schimmels gevonden. De activiteit van phytochroom is afkomstig van een open-keten tetrapyrrole chromofoor, die covalent gebonden is aan een cysteïne residu *via* een thio-ether-verbinding, op de zijketen van ring ***A***. In het geval van Cph1Δ2 nemen de drie methine bruggen van de PCB-chromofoor een *ZZZssa* geometrie in de biologisch inactieve Pr toestand aan. Tijdens de absorptie van rood licht ondergaat de C15=C16 dubbele binding een $Z \rightarrow E$ fotoisomerisatie, wat leidt tot de conversie naar de actieve Pfr toestand *via* drie intermediairen. De thermische stabiele Pfr toestand converteert terug naar Pr tijdens absorptie van ver-rood licht. De terugreactie presenteert twee intermediairen, genaamd Lumi-F en Meta-F. De eerste stap van de terugreactie is de $E \rightarrow Z$ isomerisatie van de C15=C16 dubbele binding. Het doel van dit proefschrift is om de licht-geïnduceerde mechanica van de chromofoor en zijn koppeling met het proces van intramoleculaire signaaltransductie te begrijpen.

Het onderzoek van de vrije PCB kan helpen om zijn complex gedrag in het eiwit te begrijpen. In **Hoofdstuk 2** wordt de vrije PCB in de microkristalachtige toestand onderzocht. ^{1}H, ^{13}C en ^{15}N magische hoek rotatie (MAS) en vaste-stof nucleaire magnetische resonantie (NMR) experimenten tonen aan dat twee vormen van PCB, genaamd A en B, in gelijke verhouding in het kristal aanwezig zijn. De ^{15}N NMR data verder wijzen aan dat alleen de stikstof van ring ***B*** ongeprotoneerd is. De structuur van PCB in zijn microkristalachtige toestand wordt met behulp van een combinatie van vaste-stof-NMR en kwantummechanica berekeningen bepaald. Het blijkt dat de PCB moleculen ***D***–***D***' dimmeren vormen, die door waterstofbrug interacties tussen

de stikstof van de ring ***D*** en de carbonylgroep van de ring ***D***' en *vice versa* verbonden zijn.

In **Hoofdstuk 3** worden beide stabiele toestanden Pr en Pfr in de Cph1Δ2 en *phyA*65 phytochromen met een uniform ^{13}C- en ^{15}N-, ^{13}C5- of ^{15}N21-gelabelde ingebouwde PCB-chromofoor, met ^{1}H, ^{13}C en ^{15}N 1D en 2D vaste-stof-NMR experimenten bestudeerd. Met behulp van 2D homo- en heteronucleaire pulstechnieken worden de ^{13}C en ^{15}N chemische verschuivingen van de PCB-chromofoor beschreven. De chromofoor in de cyanobacterieel en plant phytochroomen vertonen erg gelijk patronen in haar respectievelijke Pr en Pfr toestanden. De ^{15}N NMR data bewijzen dat alle vier stikstofatomen geprotoneerd zijn. Het verschil in chemische verschuiving reflecteert de verandering van de elektronische structuur van de chromofoor op het atomische niveau en de interacties tussen het eiwit en de PCB-chromofoor. De ^{13}C data worden als een versterkte waterstofbrug aan de carbonylgroep van ring ***D*** in het Pfr toestand geïnterpreteerd. De rode verschuiving van het optische absorptiemaximum in het Pfr toestand wordt verklaard door een toenemende lengte van het geconjugeerde systeem boven de ring ***C*** met de gehele ring ***D*** inbegrepen. De toegenomen conjugatie van het π-systeem stabiliseert de gespannen chromofoor in het Pfr toestand. De veranderingen aan de propionische zijketen van de ring ***C*** en aan de carbonylgroep van ring ***D*** worden als een verandering van de waterstofbrug met His-290 geïnterpreteerd. Dit en andere conformationele veranderingen kunnen tot een modificatie van de interacties aan de oppervlakte leiden.

Hoofdstuk 4 beschrijft de fotochemische geïnduceerde Pfr → Pr terugreactie. De licht-geïnduceerde Pfr → Pr conversie wordt met behulp van lage-temperatuur MAS NMR spectroscopie gevolgd. Beide Lumi-F en Meta-F intermediairen worden thermisch gevangen in de magneet. Alle vier toestanden, Pfr, Lumi-F, Meta-F en Pr worden gekarakteriseerd. Het mechanische proces van de terugreactie betreft de binding rotatie rond de C15 methine brug, dat in twee verschillende stappen omgezet wordt: (*i*) de C15=C16 dubbele binding is foto-geisomeriseerd naar de Lumi-F toestand, (*ii*) een rotatie rond de C14–C15 enkele binding vindt plaats tijdens de transformatie naar Meta-F. De structuuranalyse toont aan dat de chromofoor een verdraaide geometrie in Lumi-F aanneemt. De Meta-F intermediair vertoont een gelijk patroon als Pr, maar de waterstofbinding aan de stickstof van ring ***D*** moet nog gevormd worden en een aanpassing van de ring ***A***/eiwit interacties moet nog plaatsvinden.

Een model voor de terugreactie wordt voorgesteld.

Verscheidene groepen hebben tetrapyrrolische verbindingen met behulp van vloeistof-NMR bestudeerd. Leden van de 2,3-dihydrobilindione familie zijn in het bijzonder goede modelverbindingen voor de chromofoor in phytochroom. In **Hoofdstuk 5** zijn de chemische verschuivingen van deze verbindingen vergeleken met die van PCB in zijn vrije toestand en als chromofoor in phytochroom. Hierdoor wordt informatie verkregen over de chromofoor/eiwit interacties, die plaatsvinden tijdens de inbouw van PCB in het eiwit en tijdens de Pr → Pfr conversie. Ten eerste tonen de veranderingen in ^{13}C chemische verschuiving, ten gevolge van de inbouw in het eiwit, aan dat de ringen ***B*** en ***C*** symmetrisch zijn in de eiwit matrix. Dit suggereert dat de positieve lading over de twee binnenste ringen in het Pr toestand gedelokaliseerd is. Ten tweede, de incorporatie van PCB in het eiwit dringt andere verstoringen op aan de chromofoor. De sterkste invloed van de proteïne is gelokaliseerd op de C15 methine brug, die een (*Z*, *anti*) geometrie in het eiwit aanneemt. Het patroon van het verschil in ^{13}C chemische verschuiving door $Z \rightarrow E$ isomerisatie in de phytochroom en in de protoneerde modelverbinding in oplossing is volledig anders. Dit laat zien dat het isomeratie proces in phytochroom anders is dan in oplossing en dat de elektronische structuur door de chromofoor/eiwit interacties sterk beïnvloed wordt. Tenslotte worden toekomstige NMR experimenten besproken. Afstand- en hoekmetingen door MAS NMR kunnen informatie verstrekken over verandering in geometrie van de chromofoor in de fotocyclus. MeLoDi-type NMR experimenten kunnen gebruikt worden om de chromofoor/eiwit interacties op verschillende stadia van de fotocyclus te onderzoeken. Op deze wijze kan de licht-geïnduceerde activiteit van de chromofoor met de signaaltransductie in phytochroom verbonden worden.

Publications

T. Rohmer, H. Strauss, J. Hughes, H. de Groot, W. Gärtner, P. Schmieder, and J. Matysik. ^{15}N MAS NMR studies of Cph1 phytochrome: Chromophore dynamics and intramolecular signal transduction. *J Phys Chem B*, 110:20580–20585, **2006**.

E. Roy, T. Rohmer, P. Gast, G. Jeschke, A. Alia, and J. Matysik. Characterization of the Primary Radical Pair in Reaction Centers of *Heliobacillus mobilis* by ^{13}C Photo-CIDNP MAS NMR. *Biochemistry*, 47:4629–4635 **2008**.

T. Rohmer, C. Lang, J. Hughes, L.O. Essen, W. Gärtner, and J. Matysik. Light-induced chromophore activity and signal transduction in phytochromes observed by ^{13}C and ^{15}N magic angle spinning NMR. *Proc Natl Acad Sci USA*, 105:15229–15234, **2008**.

T. Rohmer, C. Lang, C. Bongards, K.B. Sai Sankar Gupta, J. Hughes, W. Gärtner, and J. Matysik. Magic-angle spinning NMR reveals mechanics of chromophore-protein interaction during the Pfr → Pr photoconversion process of phytochrome. *Submitted.*

T. Rohmer, C. Lang, W. Gärtner, J. Hughes, F. Mark, and J. Matysik. CP/MAS NMR study on microcrystaline phycocyanobilin. *Manuscript in preparation.*

T. Rohmer, J. Matysik, and F. Mark. Crystal effects on the geometry and NMR shieldings of bilirubin: A combined NMR spectroscopic and density functional theory study. *Manuscript in preparation.*

T. Rohmer, C. Lang, J. Hughes, W. Gärtner, and J. Matysik. MAS NMR on cyanobacterial and plant phytochromes: A comparison. *Manuscript in preparation.*

Curriculum vitae

In 1996, after obtaining the Baccalauréat in Sciences with specialization Physics and Chemistry at the Lycée Kleber, Strasbourg, France, I joined for three years the preparatory classes to the "Grandes Ecoles" at the Lycée Kleber. I was admitted at the Clermont-Ferrand's Superior National School of Chemistry (Ecole Nationale de Chimie de Clermont-Ferrand), France, where I studied organic and inorganic chemistry, chemical engineering and polymer chemistry. In 2002, I carried out an one-year voluntary internship under the guidance of Dr. Diggelmann and Dr. Lutz at the Syngenta's department of combinatorial chemistry, Basle, Switzerland. Then, I went as Erasmus exchange student to the Dublin City University, Ireland. From April to October 2004, I accomplished my master project "*Analysis of dithiocarbamate pesticides by LC/MS/MS*" under the supervision of Dr. Wanner at the Analysis and Research Center (Centre d'Analyses et de Recherche), Illkirch-Graffenstaden, France. I obtained my Master of Chemistry in October 2004.

In January 2005, I started my PhD project in the Solid-state NMR department led by Prof. Dr. Huub de Groot. Under the supervision of Dr. Jörg Matysik, I worked on the project: "*MAS NMR study of the photoreceptor phytochrome*". During my PhD time, I attended the AMPERE XIII NMR School (2005, Zakopane, Poland), Advanced European Solid-State NMR School in Biological Solids (2007, Brückentinsee, Germany) and the Seminar "Festkörper-NMR-Methoden und Anwendungen in der Materialforschung" (2008, Oberjoch, Germany). The results of my research were presented at international conferences in the form of posters. This includes the Euromar 2005, 2007 and 2008 conferences, the XXII$^{\text{nd}}$ International Conference on Magnetic Resonance in Biological systems, and the 27$^{\text{th}}$, 28$^{\text{th}}$ and 29$^{\text{th}}$ GDCh Annual Discussion Meetings. I presented my work in oral presentations at the 34$^{\text{th}}$ Meeting of the American Society for Photobiology (2008,

Burlingame, United States), the 21st GDCh lecture conference of the Photochemistry group (2008, Bielefeld, Germany), the annual meeting of the study group Theory and Spectroscopy of the chemical society section of the NWO (2009, Lunteren), and as invited speaker at the Small molecule NMR conference (2009, Chamonix, France). The work incorporated in this thesis has led to the *Ernst Award 2009* by the Magnetic Resonance Discussion Group of the German Chemical Society (Gesellschaft Deutscher Chemiker, GDCh).

Bibliography

[1] A. Batschauer. *Photoreceptors and light signalling*. Royal Society of Chemistry, Cambridge, United Kingdom, **2003**.

[2] W.R. Briggs and J.R. Spudich. *Handbook of photosensory receptors*. Wiley, Weinheim, Germany, **2005**.

[3] E. Schäfer and F. Nagy. *Photomorphogenesis in plants and bacteria: Function and signal transduction mechanisms*. Springer, Dordrecht, 3rd edition, **2006**.

[4] W.L. Butler, K.H. Norris, H.W. Siegelman, and S.B. Hendricks. Detection, assay, and preliminary purification of the pigment controlling photoresponsive development of plants. *Proc Natl Acad Sci USA*, 45:1703–1708, **1959**.

[5] R.D. Vierstra and P.H. Quail. Proteolysis alters the spectral properties of 124 kDa phytochrome from *Avena*. *Planta*, 156:158–165, **1982**.

[6] H.P. Hershey, R.F. Barker, K.B. Idler, J.L. Lissemore, and P.H. Quail. Analysis of cloned DNA and genomic sequences for phytochrome: Complete amino-acid sequences for two gene-products expressed in etiolated *Avena*. *Nucl Acids Res*, 13:8543–8559, **1985**.

[7] B. Karniol, J.R. Wagner, J.M. Walker, and R.D. Vierstra. Phylogenetic analysis of the phytochrome superfamily reveals distinct microbial subfamilies of photoreceptors. *Biochem J*, 392:103–116, **2005**.

[8] E. Giraud, S. Zappa, L. Vuillet, J.M. Adriano, L. Hannibal, J. Fardoux, C. Berthomieu, P. Bouyer, D. Pignol, and A. Vermeglio. A new type of bacteriophytochrome acts in tandem with a classical bacteriophytochrome to control the antennae synthesis in *Rhodopseudomonas palustris*. *J Biol Chem*, 280:32389–32397, **2005**.

[9] S.J. Davis, A.V. Vener, and R.D. Vierstra. Bacteriophytochromes: Phytochrome-like photoreceptors from nonphotosynthetic *eubacteria*. *Science*, 286:2517–2520, **1999**.

[10] Z.Y. Jiang, L.R. Swem, B.G. Rushing, S. Devanathan, G. Tollin, and C.E. Bauer. Bacterial photoreceptor with similarity to photoactive yellow protein and plant phytochromes. *Science*, 285:406–409, **1999**.

[11] K. Evans, J.G. Grossmann, A.P. Fordham-Skelton, and M.Z. Papiz. Small-angle X-ray scattering reveals the solution structure of a bacteriophytochrome in the catalytically active Pr state. *J Mol Biol*, 364:655–666, **2006**.

[12] A.M. Jones and H.P. Erickson. Domain structure of phytochrome from *Avena sativa* visualized by electron microscopy. *Photochem Photobiol*, 49:479–483, **1989**.

[13] M. Nakasako, T. Iwata, K. Inoue, and S. Tokutomi. Light-induced global structural changes in phytochrome A regulating photomorphogenesis in plants. *FEBS J*, 272:603–612, **2005**.

[14] N.C. Rockwell, Y.S. Su, and J.C. Lagarias. Phytochrome structure and signaling mechanisms. *Ann Rev Plant Biol*, 57:837–858, **2006**.

[15] B.L. Montgomery and J.C. Lagarias. Phytochrome ancestry: Sensors of bilins and light. *Trends Plant Sci*, 7:357–366, **2002**.

[16] B. Karniol and R.D. Vierstra. *Photomorphogenesis in plants and bacteria*. Springer, Dordrecht, **2006**.

[17] T. Lamparter, M. Carrascal, N. Michael, E. Martinez, G. Rottwinkel, and J. Abian. The biliverdin chromophore binds covalently to a conserved cysteine residue in the N-terminus of *Agrobacterium* phytochrome agp1. *Biochemistry*, 43:3659–3669, **2004**.

[18] J.R. Wagner, J.S. Brunzelle, K.T. Forest, and R.D. Vierstra. A light-sensing knot revealed by the structure of the chromophore-binding domain of phytochrome. *Nature*, 438:325–331, **2005**.

[19] J. Hahn, H.M. Strauss, F.T. Landgraf, H.F. Gimenez, G. Lochnit, P. Schmieder, and J. Hughes. Probing protein-chromophore interactions in Cph1 phytochrome by mutagenesis. *FEBS J*, 273:1415–1429, **2006**.

[20] J.C. Lagarias and H. Rapoport. Chromopeptides from phytochrome: The structure and linkage of the Pr form of the phytochrome chromophore. *J Am Chem Soc*, 102:4821–4828, **1980**.

[21] T. Lamparter, B. Esteban, and J. Hughes. Phytochrome Cph1 from the cyanobacterium *synechocystis* PCC6803: Purification, assembly, and quaternary structure. *Eur J Biochem*, 268:4720–4730, **2001**.

[22] B. Borucki, H. Otto, G. Rottwinkel, J. Hughes, M.P. Heyn, and T. Lamparter. Mechanism of Cph1 phytochrome assembly from stopped-flow kinetics and circular dichroism. *Biochemistry*, 42:13684–13697, **2003**.

[23] D.M. Arciero, J.L. Dallas, and A.N. Glazer. *In vitro* attachment of bilins to apophycocyanin: Determination of the structures of tryptic bilin peptides derived from the phycocyanobilin adduct. *J Biol Chem*, 263:18350–18357, **1988**.

[24] B. Knipp, M. Müller, N. Metzler-Nolte, T.S. Balaban, S.E. Braslavsky, and K. Schaffner. NMR verification of helical conformations of phycocyanobilin in organic solvents. *Helv Chim Acta*, 81:881–888, **1998**.

[25] A.H. Göller, D. Strehlow, and G. Hermann. The excited-state chemistry of phycocyanobilin: A semiempirical study. *ChemPhysChem*, 6:1259–1268, **2005**.

[26] F. Thümmler, W. Rüdiger, E. Cmiel, and S. Schneider. Chromopeptides from phytochrome and phycocyanin: NMR studies of the Pfr and Pr chromophore of phytochrome and *E*,*Z* isomeric chromophores of phycocyanin. *Z Naturforsch A*, 38:359–368, **1983**.

[27] F. Andel, J.C. Lagarias, and R.A. Mathies. Resonance Raman analysis of chromophore structure in the Lumi-R photoproduct of phytochrome. *Biochemistry*, 35:15997–16008, **1996**.

[28] Y. Mizutani, S. Tokutomi, and T. Kitagawa. Resonance Raman-spectra of the intermediates in phototransformation of large phytochrome - deprotonation of the chromophore in the bleached intermediate. *Biochemistry*, 33:153–158, **1994**.

[29] W. Rüdiger, F. Thümmler, E. Cmiel, and S. Schneider. Chromophore structure of the physiologically active form Pfr of phytochrome. *Proc Natl Acad Sci USA*, 80:6244–6248, **1983**.

[30] F. Andel, K.C. Hasson, F. Gai, P.A. Anfinrud, and R.A. Mathies. Femtosecond time-resolved spectroscopy of the primary photochemistry of phytochrome. *Biospectroscopy*, 3:421–433, **1997**.

[31] M. Bischoff, G. Hermann, S. Rentsch, and D. Strehlow. First steps in the phytochrome phototransformation: A comparative femtosecond study on the forward Pr $\longrightarrow$ Pfr and back reaction Pfr $\longrightarrow$ Pr. *Biochemistry*, 40:181–186, **2001**.

[32] M. Bischoff, G. Hermann, S. Rentsch, D. Strehlow, S. Winter, and H. Chosrowjan. Excited-state processes in phycocyanobilin studied by femtosecond spectroscopy. *J Phys Chem B*, 104:1810–1816, **2000**.

[33] K. Heyne, J. Herbst, D. Stehlik, B. Esteban, T. Lamparter, J. Hughes, and R. Diller. Ultrafast dynamics of phytochrome from the cyanobacterium *Synechocystis* reconstituted with phycocyanobilin and phycoerythrobilin. *Biophys J*, 82:1004–1016, **2002**.

[34] C. Schumann, R. Gross, N. Michael, T. Lamparter, and R. Diller. Subpicosecond mid-infrared spectroscopy of phytochrome Agp1 from *Agrobacterium tumefaciens*. *ChemPhysChem*, 8(11):1657–1663, **2007**.

[35] C. Schumann, R. Gross, M.M.N. Wolf, R. Diller, N. Michael, and T. Lamparter. Subpicosecond midinfrared spectroscopy of the Pfr reaction of phytochrome Agp1 from *Agrobacterium tumefaciens*. *Biophys J*, 94:3189–3197, **2008**.

[36] M.G. Müller, I. Lindner, I. Martin, W. Gärtner, and A.R. Holzwarth. Femtosecond kinetics of photoconversion of the higher plant photoreceptor phytochrome carrying native and modified chromophores. *Biophys J*, 94:4370–4382, **2008**.

[37] T. Lamparter, F. Mittmann, W. Gärtner, T. Börner, E. Hartmann, and J. Hughes. Characterization of recombinant phytochrome from the cyanobacterium *Synechocystis*. *Proc Natl Acad Sci USA*, 94:11792–11797, **1997**.

[38] T. Gensch, M.S. Churio, S.E. Braslavsky, and K. Schaffner. Primary quantum yield and volume change of phytochrome: A phototransformation determined by laser-induced optoacoustic spectroscopy. *Photochem Photobiol*, 63:719–725, **1996**.

[39] H. Foerstendorf, C. Benda, W. Gärtner, M. Storf, H. Scheer, and F. Siebert. FTIR studies of phytochrome photoreactions reveal the C=O bands of the chromophore: Consequences for its protonation states, conformation, and protein interaction. *Biochemistry*, 40:14952–14959, **2001**.

[40] H. Foerstendorf, E. Mummert, E. Schäfer, H. Scheer, and F. Siebert. Fourier-transform infrared spectroscopy of phytochrome: Difference spectra of the intermediates of the photoreactions. *Biochemistry*, 35:10793–10799, **1996**.

[41] C. Kneip, D. Mozley, P. Hildebrandt, W. Gärtner, S.E. Braslavsky, and K. Schaffner. Effect of chromophore exchange on the resonance Raman spectra of recombinant phytochromes. *FEBS Lett*, 414:23–26, **1997**.

[42] A. Remberg, I. Lindner, T. Lamparter, J. Hughes, C. Kneip, P. Hildebrandt, S.E. Braslavsky, W. Gärtner, and K. Schaffner. Raman spectroscopic and light-induced kinetic characterization of a recombinant phytochrome of the cyanobacterium *Synechocystis*. *Biochemistry*, 36:13389–13395, **1997**.

[43] J. Matysik, P. Hildebrandt, W. Schlamann, S.E. Braslavsky, and K. Schaffner. Fourier-transform resonance Raman-spectroscopy of intermediates of the phytochrome photocycle. *Biochemistry*, 34:10497–10507, **1995**.

[44] A.J. Fischer and J.C. Lagarias. Harnessing phytochrome's glowing potential. *Proc Natl Acad Sci USA*, 101:17334–17339, **2004**.

[45] Y. Oka, T. Matsushita, N. Mochizuki, T. Suzuki, S. Tokutomi, and A. Nagatani. Functional analysis of a 450-amino acid N-terminal fragment of phytochrome B in *Arabidopsis*. *Plant Cell*, 16:2104–2116, **2004**.

[46] I. Lindner, S.E. Braslavsky, K. Schaffner, and W. Gärtner. Model studies of phytochrome photochromism: Protein-mediated photoisomerization of a linear tetrapyrrole in the absence of covalent bonding. *Angew Chem Intl Ed Engl*, 39:3269–3271, **2000**.

[47] C.M. Park, J.Y. Shim, S.S. Yang, J.G. Kang, J.I. Kim, Z. Luka, and P.S. Song. Chromophore-apoprotein interactions in *Synechocystis* sp. PCC6803 phytochrome Cph1. *Biochemistry*, 39:6349–6356, **2000**.

[48] S.H. Wu and J.C. Lagarias. Defining the bilin lyase domain: Lessons from the extended phytochrome superfamily. *Biochemistry*, 39:13487–13495, **2000**.

[49] A. Remberg, P. Schmidt, S.E. Braslavsky, W. Gärtner, and K. Schaffner. Differential effects of mutations in the chromophore pocket of recombinant phytochrome on chromoprotein assembly and Pr-to-Pfr photoconversion. *Eur J Biochem*, 266:201–208, **1999**.

[50] I. Lindner, B. Knipp, S.E. Braslavsky, W. Gärtner, and K. Schaffner. A novel chromophore selectively modifies the spectral properties of one of the two stable states of the plant photoreceptor phytochrome. *Angew Chem Intl Ed Engl*, 37:1843–1846, **1998**.

[51] J.R. Wagner, J.R. Zhang, J.S. Brunzelle, R.D. Vierstra, and K.T. Forest. High resolution structure of *Deinococcus* bacteriophytochrome yields new insights into phytochrome architecture and evolution. *J Biol Chem*, 282:12298–12309, **2007**.

[52] X. Yang, E.A. Stojkovic, J. Kuk, and K. Moffat. Crystal structure of the chromophore binding domain of an unusual bacteriophytochrome, RpBphP3, reveals residues that modulate photoconversion. *Proc Natl Acad Sci USA*, 104:12571–12576, **2007**.

[53] L.O. Essen, J. Mailliet, and J. Hughes. The structure of a complete phytochrome sensory module in the Pr ground state. *Proc Natl Acad Sci USA*, 105:14709–14714, **2008**.

[54] P. Schwinté, H. Foerstendorf, Z. Hussain, W. Gärtner, M.A. Mroginski, P. Hildebrandt, and F. Siebert. FTIR study of the photoinduced processes of plant phytochrome phyA using isotope-labeled bilins and density functional theory calculations. *Biophys J*, 95:1256–1267, **2008**.

[55] X. Yang, J. Kuk, and K. Moffat. Crystal structure of *Pseudomonas aeruginosa* bacteriophytochrome: Photoconversion and signal transduction. *Proc Natl Acad Sci USA*, 105:14715–14720, **2008**.

[56] A. Abraham. *Principles of nuclear magnetism.* Oxford University Press, Oxford, United Kingdom, **1961**.

[57] M.J. Duer. *Introduction to solid-state NMR spectroscopy.* Blackwell Publishing Ltd., Oxford, United Kingdom, **2004**.

[58] K. Schmidt-Rohr and W. Spiess. *Multidimensional solid-state NMR and polymers.* Acamdemic Press Ltd., London, United Kingdom, **1994**.

[59] E.R. Andrew, A. Bradbury, and R.G. Eades. Nuclear magnetic resonance spectra from a crystal rotated at high speed. *Nature*, 182:1659–1659, **1958**.

[60] W. Kessemeier and R.E. Norberg. Pulsed nuclear magnetic resonance in rotating solids. *Phys Rev*, 155:321–337, **1967**.

[61] I.J. Lowe. Free induction decays of rotating solids. *Phys Rev Lett*, 2:285–287, **1959**.

[62] S.R. Hartmann and E.L. Hahn. Nuclear double resonance in rotating frame. *Phys Rev*, 128:2042–2053, **1962**.

[63] K. Takegoshi, S. Nakamura, and T. Terao. ^{13}C-^{1}H dipolar-driven ^{13}C-^{13}C recoupling without ^{13}C RF irradiation in nuclear magnetic resonance of rotating solids. *J Chem Phys*, 118:2325–2341, **2003**.

[64] K. Takegoshi, S. Nakamura, and T. Terao. ^{13}C-^{1}H dipolar-assisted rotational resonance in magic angle spinning NMR. *Chem Phys Lett*, 344:631–637, **2001**.

[65] A.E. Bennett, C.M. Rienstra, M. Auger, K.V. Lakshmi, and R. G. Griffin. Heteronuclear decoupling in rotating solids. *J Chem Phys*, 103:6951–6958, **1995**.

[66] M. Lee and W.I. Goldburg. Nuclear magnetic resonance line narrowing by a rotating RF field. *Phys Rev*, 140:1261–1271, **1965**.

[67] A. Bielecki, A.C. Kolbert, and M.H. Levitt. Frequency-switched pulse sequences: Homonuclear decoupling and dilute spin NMR in solids. *Chem Phys Lett*, 155:341–346, **1989**.

[68] B.J. van Rossum, H. Förster, and H.J.M. de Groot. High-field and high-speed CP/MAS ^{13}C NMR heteronuclear dipolar-correlation spectroscopy of solids with frequency-switched Lee-Goldburg homonuclear decoupling. *J Magn Res*, 124:516–519, **1997**.

[69] M.D. Maines. The heme oxygenase system: A regulator of second messenger gases. *Ann Rev Pharm Tox*, 37:517–554, **1997**.

[70] R.F. Troxler and L. Bogorad. Studies on formation of phycocyanin porphyrins and a blue phycobilin by wild-type and mutant strains of *cyanidium caldarium*. *Plant Physiol*, 41:491–499, **1966**.

[71] J. Hughes, T. Lamparter, F. Mittmann, E. Hartmann, W. Gärtner, A. Wilde, and T. Börner. A prokaryotic phytochrome. *Nature*, 386:663–663, **1997**.

[72] J. Crusats, A. Delgado, J.A. Farrera, R. Rubires, and J.M. Ribó. Solution structure of mesobilirubin XIIIα bridged between the propionic acid substituents. *Monatsh Chem*, 129:741–753, **1998**.

[73] H. Marko, N. Müller, and H. Falk. NMR investigations of the biliverdin-apomyoglobin complex. *Eur J Biochem*, 193:573–580, **1990**.

[74] S.E. Braslavsky, D. Schneider, K. Heihoff, S. Nonell, P.F. Aramendia, and K. Schaffner. Phytochrome models: Photophysics and photochemistry of phycocyanobilin dimethyl ester. *J Am Chem Soc*, 113:7322–7334, **1991**.

[75] A.H. Göller, D. Strehlow, and G. Hermann. Conformational flexibility of phycocyanobilin: An AM1 semiempirical study. *ChemPhysChem*, 2:665–671, **2001**.

[76] B. Dietzek, R. Maksimenka, G. Hermann, W. Kiefer, J. Popp, and M. Schmitt. The excited-state dynamics of phycocyanobilin in dependence on the excitation wavelength. *ChemPhysChem*, 5:1171–1177, **2004**.

[77] H. Falk. *The Chemistry of Linear Oligopyrroles and Bile Pigments*. Springer-Verlag, **1989**.

[78] D.D. Laws, H.M.L. Bitter, and A. Jerschow. Solid-state NMR spectroscopic methods in chemistry. *Angew Chem Intl Ed Engl*, 41:3096–3129, **2002**.

[79] I. de Boer, J. Matysik, M. Amakawa, S. Yagai, H. Tamiaki, A.R. Holzwarth, and H.J.M. de Groot. MAS NMR structure of a microcrystalline Cd-bacteriochlorophyll *d* analogue. *J Am Chem Soc*, 125:13374–13375, **2003**.

[80] A.B. Siemer, A.A. Arnold, C. Ritter, T. Westfeld, M. Ernst, R. Riek, and B.H. Meier. Observation of highly flexible residues in amyloid fibrils of the HET-s prion. *J Am Chem Soc*, 128:13224–13228, **2006**.

[81] F. Castellani, B. van Rossum, A. Diehl, M. Schubert, K. Rehbein, and H. Oschkinat. Structure of a protein determined by solid-state magic angle spinning NMR spectroscopy. *Nature*, 420:98–102, **2002**.

[82] A.J. van Gammeren, F.B. Hulsbergen, J.G. Hollander, and H.J.M. de Groot. Residual backbone and side-chain ^{13}C-^{13}C and ^{15}N resonance assignments of the intrinsic transmembrane light-harvesting-2 protein complex by solid-state magic angle spinning NMR spectroscopy. *J Biomol NMR*, 31:279–293, **2005**.

[83] Alia, J. Matysik, C. Soede-Huijbregts, M. Baldus, J. Raap, J. Lugtenburg, P. Gast, H.J. van Gorkom, A.J. Hoff, and H.J.M. de Groot. Ultrahigh field MAS NMR dipolar correlation spectroscopy of the histidine residues in light-harvesting complex II from photosynthetic bacteria reveals partial internal

charge transfer in the B850/His complex. *J Am Chem Soc*, 123:4803–4809, **2001**.

[84] Y.F. Wei, A.C. de Dios, and A.E. McDermott. Solid-state ^{15}N NMR chemical shift anisotropy of histidines: Experimental and theoretical studies of hydrogen bonding. *J Am Chem Soc*, 121:10389–10394, **1999**.

[85] W.S. Sheldrick. Crystal and molecular structure of biliverdin dimethyl ester. *J Chem Soc, Perkin Trans 2*, pages 1457–1462, **1976**.

[86] U. Wagner, C. Kratky, H. Falk, and H. Woss. Crystal structure and conformation of 10-aryl-bilatrienes. *Monatsh Chem*, 122:749–758, **1991**.

[87] H. Falk, K. Grubmayr, K. Magauer, N. Müller, and U. Zrunek. On the chemistry of pyrrole pigments. Phytochrome model studies: The tautomerism at N-22-N-23 of unsymmetrically substituted bilatrienes and 2,3-dihydrobilatrienes. *Israel J Chem*, 23:187–194, **1983**.

[88] M. Hölzl, A. Jarosik, and K. Grubmayr. Inducing *anti*-conformers of biliverdin chromophores by reducing sterical hindrance. *Monatsh Chem*, 136:747–754, **2005**.

[89] C. Kneip, P. Hildebrandt, K. Nemeth, F. Mark, and K. Schaffner. Interpretation of the resonance Raman spectra of linear tetrapyrroles based on DFT calculations. *Chem Phys Lett*, 311:479–484, **1999**.

[90] C. Kratky, H. Falk, K. Grubmayr, and U. Zrunek. On the molecular-structure of the phytochrome chromophore: X-ray-analysis of two 2,3-dihydrobilatriene-abc derivatives. *Monatsh Chem*, 116:761–776, **1985**.

[91] U.G. Wagner, C. Kratky, H. Falk, and G. Kapl. Synthesis and X-ray crystal-structure of a 15*E*-dihydrobilatriene-abc-derivate. *Monatsh Chem*, 117:1413–1422, **1986**.

[92] A.D. Becke. A new mixing of Hartree-Fock and local density-functional theories. *J Chem Phys*, 98:1372–1377, **1993**.

[93] M.J. Frisch, G.W. Trucks, H.B. Schlegel, G.E. Scuseria, M.A. Robb, J.R. Cheeseman, J.A. Montgomery Jr., T. Vreven, K.N. Kudin, J.C. Burant, J.M. Millam, S.S. Iyengar, J. Tomasi, V. Barone, B. Mennucci, M. Cossi, G. Scalmani, N. Rega, G.A. Petersson, H. Nakatsuji, M. Hada, M. Ehara, K. Toyota, R. Fukuda, J. Hasegawa, M. Ishida, T. Nakajima, Y. Honda, O. Kitao, H. Nakai, M. Klene, X. Li, J.E. Knox, H.P. Hratchian, J.B. Cross, C. Adamo, J. Jaramillo, R. Gomperts, R.E. Stratmann, O. Yazyev, A.J. Austin, R. Cammi, C. Pomelli, J.W. Ochterski, P.Y. Ayala, K. Morokuma, G.A. Voth, P. Salvador, J.J. Dannenberg, V.G. Zakrzewski, S. Dapprich, A.D. Daniels, M.C.

Strain, O. Farkas, D.K. Malick, A.D. Rabuck, K. Raghavachari, J.B. Foresman, J.V. Ortiz, Q. Cui, A.G. Baboul, S. Clifford, J. Cioslowski, B.B. Stefanov, G. Liu, A. Liashenko, P. Piskorz, I. Komaromi, R.L. Martin, D.J. Fox, T. Keith, M.A. Al-Laham, C.Y. Peng, A. Nanayakkara, M. Challacombe, P.M.W. Gill, B. Johnson, W. Chen, M.W. Wong, C. Gonzalez, and J.A. Pople. Gaussian 03, Revision C.02, Gaussian, Inc., Wallingford CT, 2004.

[94] H.M. Strauss, J. Hughes, and P. Schmieder. Heteronuclear solution-state NMR studies of the chromophore in cyanobacterial phytochrome Cph1. *Biochemistry*, 44:8244–8250, **2005**.

[95] M. Baldus, D.G. Geurts, S. Hediger, and B.H. Meier. Efficient ^{15}N-^{13}C polarization transfer by adiabatic-passage Hartmann-Hahn cross polarization. *J Magn Res*, 118:140–144, **1996**.

[96] S.E. Braslavsky, W. Gärtner, and K. Schaffner. Phytochrome photoconversion. *Plant Cell Environ*, 20:700–706, **1997**.

[97] S.P.A. Fodor, J.C. Lagarias, and R.A. Mathies. Resonance Raman analysis of the Pr and Pfr forms of phytochrome. *Biochemistry*, 29:11141–11146, **1990**.

[98] J.R. Wagner, J.R. Zhang, D. von Stetten, M. Günther, D.H. Murgida, M.A. Mroginski, J.M. Walker, K.T. Forest, P. Hildebrandt, and R.D. Vierstra. Mutational analysis of *Deinococcus radiodurans* bacteriophytochrome reveals key amino acids necessary for the photochromicity and proton exchange cycle of phytochromes. *J Biol Chem*, 283:12212–12226, **2008**.

[99] H. Heise, W. Hoyer, S. Becker, O.C. Andronesi, D. Riedel, and M. Baldus. Molecular-level secondary structure, polymorphism, and dynamics of full-length α-synuclein fibrils studied by solid-state NMR. *Proc Natl Acad Sci USA*, 102:15871–15876, **2005**.

[100] P. Schmidt, T. Gensch, A. Remberg, W. Gärtner, S.E. Braslavsky, and K. Schaffner. The complexity of the Pr to Pfr phototransformation kinetics is an intrinsic property of native phytochrome. *Photochem Photobiol*, 68:754–761, **1998**.

[101] V.A. Sineshchekov. Extreme dehydration of plant tissues irreversibly converts the major and variable phyA' into the minor and conserved phyA". *J Photochem Photobiol*, 85:85–91, **2006**.

[102] J. Hahn, R. Kuhne, and P. Schmieder. Solution-state ^{15}N NMR spectroscopic study of α-C-phycocyanin: Implications for the structure of the chromophore-binding pocket of the cyanobacterial phytochrome Cph1. *ChemBioChem*, 8:2249–2255, **2007**.

[103] M. Stanek and K. Grubmayr. Protonated 2,3-dihydrobilindiones: Models for the chromophores of phycocyanin and the red absorbing form of phytochrome. *Chem Eur J*, 4:1653–1659, **1998**.

[104] T. Rohmer, H. Strauss, J. Hughes, H. de Groot, W. Gärtner, P. Schmieder, and J. Matysik. ^{15}N MAS NMR studies of Cph1 phytochrome: Chromophore dynamics and intramolecular signal transduction. *J Phys Chem B*, 110:20580–20585, **2006**.

[105] G. Filippini and A. Gavezzotti. The crystal-structure of 1,3,5-triamino-2,4,6-trinitrobenzene - centrosymmetric or noncentrosymmetric. *Chem Phys Lett*, 231:86–92, **1994**.

[106] H. Foerstendorf, T. Lamparter, J. Hughes, W. Gärtner, and F. Siebert. The photoreactions of recombinant phytochrome from the cyanobacterium *Synechocystis*: A low-temperature UV-Vis and FTIR spectroscopic study. *Photochem Photobiol*, 71:655–661, **2000**.

[107] W.L. DeLano. The PyMOL molecular graphics system. www.pymol.org, **2002**.

[108] L. Yu. *Solitons and polarons in conduction polymers*. World Scientific, Singapore, **1988**.

[109] J.H. Koek. *Synthesis and spectroscopy of tetrapyrrol systems related to biliprotein chromophores*. PhD thesis, Leiden University, 1987.

[110] D. Mozley, A. Remberg, and W. Gärtner. Large-scale generation of affinity purified recombinant phytochrome chromopeptide. *Photochem Photobiol*, 66:710–715, **1997**.

[111] H.M. Strauss, P. Schmieder, and J. Hughes. Light-dependent dimerisation in the N-terminal sensory module of cyanobacterial phytochrome 1. *FEBS Lett*, 579:3970–3974, **2005**.

[112] P. Eilfeld, P. Eilfeld, J. Vogel, and R. Maurer. Evidence for a sequential pathway from Pr to Pfr of the phototransformation of 124-kDa oat phytochrome. *Photochem Photobiol*, 45:825–830, **1987**.

[113] P. Eilfeld and W. Rüdiger. Absorption spectra of phytochrome intermediates. *Z Naturforsch*, 40:109–114, **1985**.

[114] R.D. Scurlock, C.H. Evans, S.E. Braslavsky, and K. Schaffner. A phytochrome phototransformation study using two-laser/two-color flash-photolysis: Analysis of the decay mechanism of I(700). *Photochem Photobiol*, 58:106–115, **1993**.

[115] W. Gärtner and S.E. Braslavsky. *Photoreceptors and light signalling,*, volume 3, chapter The Phytochromes: Spectroscopy and Function, pages 136–180. Royal Society Chemistry, Cambridge, United Kingdom, D.P. Häder and G. Jori edition, **2003**.

[116] P. Schwinté, W. Gärtner, S. Sharda, M.A. Mroginski, P. Hildebrandt, and F. Siebert. The photoreactions of recombinant phytochrome CphA from the cyanobacterium *Calothrix* PCC7601: A low-temperature UV-Vis and FTIR study. *Photochem Photobiol*, 85:239–249, **2009**.

[117] M. Concistrè, A. Gansmüller, N. McLean, O.G. Johannessen, I.M. Montesinos, P.H.M. Bovee-Geurts, P. Verdegem, J. Lugtenburg, R.C.D. Brown, W.J. de Grip, and M.H. Levitt. Double-quantum ^{13}C nuclear magnetic resonance of bathorhodopsin, the first photointermediate in mammalian vision. *J Am Chem Soc*, 130:10490–10491, **2008**.

[118] M.L. Mak-Jurkauskas, V.S. Bajaj, M.K. Hornstein, M. Belenky, R.G. Griffin, and J. Herzfeld. Energy transformations early in the bacteriorhodopsin photocycle revealed by DNP-enhanced solid-state NMR. *Proc Natl Acad Sci USA*, 105:883–888, **2008**.

[119] A.V. Cherepanov, E.V. Doroshenko, J. Matysik, S. de Vries, and H.J.M. de Groot. The associative nature of adenylyl transfer catalyzed by T4 DNA ligase. *Proc Natl Acad Sci USA*, 105:8563–8568, **2008**.

[120] T. Rohmer, C. Lang, J. Hughes, L.O. Essen, W. Gärtner, and J. Matysik. Light-induced chromophore activity and signal transduction in phytochromes observed by ^{13}C and ^{15}N magic-angle spinning NMR. *Proc Natl Acad Sci USA*, 105:15229–15234, **2008**.

[121] U. Robben, I. Lindner, and W. Gärtner. New open-chain tetrapyrroles as chromophores in the plant photoreceptor phytochrome. *J Am Chem Soc*, 130:11303–11311, **2008**.

[122] J. Dasgupta, R.R. Frontiera, K.C. Taylor, J.C. Lagarias, and R.A. Mathies. Ultrafast excited-state isomerization in phytochrome revealed by femtosecond stimulated Raman spectroscopy. *Proc Natl Acad Sci USA*, 106:1784–1789, **2009**.

[123] W.M. Gong, B. Hao, and M.K. Chan. New mechanistic insights from structural studies of the oxygen-sensing domain of *Bradyrhizobium japonicum* FixL. *Biochemistry*, 39:3955–3962, **2000**.

[124] E. Daviso, G. Jeschke, and J. Matysik. *Biophysical Techniques in Photosynthesis*, volume 26 of *Advances in Photosynthesis and Respiration*, chapter Photo-CIDNP Magic Angle Spinning NMR, page 385–399. Springer Publishers, Dordrecht, **2008**.

[125] A.F.L. Creemers, S. Kiihne, P.H.M. Bovee-Geurts, W.J. de Grip, J. Lugtenburg, and H.J.M. de Groot. H-1 and C-13 MAS NMR evidence for pronounced ligand-protein interactions involving the ionone ring of the retinylidene chromophore in rhodopsin. *Proc Natl Acad Sci USA*, 99:9101–9106, **2002**.

[126] S.R. Kiihne, A.F.L. Creemers, W.J. de Grip, P.H.M. Bovee-Geurts, J. Lugtenburg, and H.J.M. de Groot. Selective interface detection: Mapping binding site contacts in membrane proteins by NMR spectroscopy. *J Am Chem Soc*, 127:5734–5735, **2005**.

[127] M.A. Verhoeven, P.H.M. Bovee-Geurts, H.J.M. de Groot, J. Lugtenburg, and W.J. de Grip. Methyl substituents at the 11 or 12 position of retinal profoundly and differentially affect photochemistry and signalling activity of rhodopsin. *J Mol Biol*, 363:98–113, **2006**.

[128] A. Bifone, H.J.M. de Groot, and F. Buda. Ab initio molecular dynamics of rhodopsin. *Pure Appl Chem*, 69:2105–2110, **1997**.

[129] A. Cembran, F. Bernardi, M. Olivucci, and M. Garavelli. Excited-state singlet manifold and oscillatory features of a nonatetraeniminium retinal chromophore model. *J Am Chem Soc*, 125:12509–12519, **2003**.

[130] P.J.E. Verdegem, M. Helmle, J. Lugtenburg, and H.J.M. de Groot. Internuclear distance measurements up to 0.44 nm for retinals in the solid state with 1-D rotational resonance C-13 MAS NMR spectroscopy. *J Am Chem Soc*, 119:169–174, **1997**.

[131] H. Görner and H.J. Kuhn. *Advances in Photochemistry*, volume 19, chapter *Cis-trans* photoisomerization of stilbenes and stilbene-like molecules. Wiley InterScience, **1995**.

[132] H. Falk, K. Grubmayr, E. Haslinger, T. Schlederer, and K. Thirring. Chemistry of pyrrole pigments: Diastereomeric (geometrically isomeric) biliverdindimethylesters-structure, configuration and conformation. *Monatsh Chem*, 109:1451–1473, **1978**.

[133] K. Smit, J. Matysik, P. Hildebrandt, and F. Mark. Vibrational analysis of biliverdin dimethyl ester. *J Phys Chem*, 97:11887–11900, **1993**.

[134] J. Matysik, P. Hildebrandt, K. Smit, F. Mark, W. Gärtner, S.E. Braslavsky, K. Schaffner, and B. Schrader. Raman spectroscopic analysis of isomers of biliverdin dimethyl ester. *J Pharm Biomed Anal*, 15:1319–1324, **1997**.

[135] B. Durbeej. On the primary event of phytochrome: quantum chemical comparison of photoreactions at C-4, C-10 and C-15. *Phys Chem Chem Phys*, 11:1354–1361, **2009**.

[136] X.L. Yao, K. Schmidt-Rohr, and M. Hong. Medium- and long-distance H-1-C-13 heteronuclear correlation NMR in solids. *J Magn Reson*, 149:139–143, **2001**.

[137] N. Khaneja and N.C. Nielsen. Triple oscillating field technique for accurate distance measurements by solid-state NMR. *J Chem Phys*, 128, **2008**.

[138] S.R. Kiihne, A.F.L. Creemers, J. Lugtenburg, and H.J.M. de Groot. Accurate CSA measurements from uniformly isotopically labeled biomolecules at high magnetic field. *J Magn Reson*, 172:1–8, **2005**.

[139] T. Kakiuchi, H. Kato, K.P. Jayasundera, T. Higashi, K. Watabe, D. Sawamoto, H. Kinoshita, and K. Inomata. Total syntheses of ±-phycocyanobilin and its derivatives bearing a photoreactive group at D ring. *Chem Lett*, pages 1001–1002, **1998**.

[140] A. Gossauer and W. Hirsch. Syntheses of bile-pigments: Total synthesis of racemic phycocyanobilin (phycobiliverdin) and of a homophycobiliverdin. *Liebigs Ann Chem*, pages 1496–1513, **1974**.

[141] Y. Makhynya, Z. Hussain, T. Bauschlicher, P. Schwinté, F. Siebert, and W. Gärtner. Synthesis of selectively ^{13}C-labelled bilin compounds. *Eur J Org Chem*, pages 1287–1293, **2007**.